Stress and strain rate estimates associated with penetrative deformation of the Harkless quartzite aureole rocks, Papoose Flat Pluton, eastern California/Using structure contour maps to analyze subsurface 3D fault geometry along segments of the Moine thrust, NW Scotland

Nicholas Dean Heaverlo

Thesis submitted to the faculty of the Virginia Polytechnic Institute and State University in partial fulfillment of the requirements for the degree of

Master of Science
In
Geosciences

Committee:
Richard D. Law (*Chair*)
Mark J. Caddick
James A. Spotila

May 7th, 2014

Blacksburg, VA

Keywords: Papoose Flat pluton, piezometers, strain rate, Moine thrust zone, structure contour maps, Glencoul thrust

Stress and strain rate estimates associated with penetrative deformation of the Harkless quartzite aureole rocks, Papoose Flat Pluton, eastern California/Using structure contour maps to analyze subsurface 3D fault geometry along segments of the Moine thrust, NW Scotland

Nicholas Dean Heaverlo

ABSTRACT

Dynamically recrystallized quartz microstructures preserved in contact aureoles allow for stress and strain rate estimates associated with penetrative deformation of rocks surrounding pluton margins. Microstructural analysis of the Harkless quartzites surrounding the western margin of Papoose Flat pluton indicates that recrystallization occurred by grain boundary migration with mean recrystallized grain size ranging from 86-225 μm. The application of three calibrated piezometers results in differential stress estimates between ~11 and ~29 MPa. Published wet-quartzite dislocation creep flow laws combined with deformation temperature, water fugacity, and differential stress estimates infer strain rates that range from 1.2×10^{-14} s^{-1} to 2.3×10^{-12} s^{-1}.

In order to analyze 3D subsurface fault geometry along map-pattern curves (salients and recesses), a structure contour map of the Moine thrust, extending from the North Coast southwards to the Dundonnel area, was constructed from 1:50,000 scale British Geological Survey (BGS) maps by correlating between elevation control points constrained by the intersection of the fault trace with topographic contours. The structure contour map indicates significant lateral variation in fault geometry along the Moine thrust, with recesses associated with antiformal corrugations in the subsurface and salients characterized by planar geometries or broad synformal corrugations. Additionally, structure contour maps constructed on the Glencoul thrust, as depicted by original BGS maps confirms that the thrust segments to the NE and SW of Loch Glencoul are part of the same structure, rather than different structures separated by a lateral ramp as shown on more recent BGS maps.

This thesis is dedicated to my parents,

Ron and Kim Heaverlo

ACKNOWLEDGMENTS

First and foremost, I would like to express my gratitude to my advisor Rick Law, who has been beyond helpful throughout my entire graduate school experience. His patience, enthusiasm, and immeasurable knowledge helped me throughout the research and writing process. In addition to his academic support, Rick's kindness and sense of humor made me feel immediately welcome at Virginia Tech, and the past two years I have spent as part of his research group will always be thought of fondly.

Additionally, I must thank the other two members of my research committee, Mark Caddick and Jim Spotila, for their insight and interest in my projects during my time at Virginia Tech.

I must also thank two professors from my undergraduate work at The University of Iowa; Jane Gilotti and Bill Mclelland, who continued to push me to become a better geologist and student. They opened up many opportunities to me within the field of geosciences, including an opportunity to work as a geologist in Alaska following my undergraduate work, and I can never thank these two enough.

More thanks go out to our research group consisting of Sarah Mazza, Kyle Overby, and Kyle Ashley, for their willingness to talk about my research and to grab a beer when it was needed.

My family cannot be thanked enough for supporting me over the years. I could never put how much they mean into words.

And last, but not least, I thank my incredible girlfriend, Katherine Marek, who continued to encourage me throughout the process. I couldn't have done it without her and I look forward to many more adventures with her in the future!

CHAPTER 3

LIST OF FIGURES

CHAPTER 2

CHAPTER 3

LIST OF TABLES

CHAPTER 2

LIST OF EQUATIONS

CHAPTER 1

Introduction

This thesis is separated into two distinct structural- and petrology- based chapters which detail the application of two different techniques, at the microstructural (Chapter 2) and regional (Chapter 3) scales.

In Chapter 2, "*Stress and strain rate estimates associated with penetrative deformation of the Harkless quartzite aureole rocks, Papoose Flat Pluton, eastern California"*, we used published piezometers and wet-quartzite flow laws to estimate differential stress and strain rates associated with penetrative deformation of aureole rocks around the western margin of the Papoose Flat pluton, in eastern California. Along the plutons western margin, stratigraphic units were thinned to nearly 10% of their regional thickness as a result of forcible pluton emplacement. In order to estimate the rate at which the aureole rocks were strained, thin sections were analyzed from six locations along the pluton's western margin to determine the size of the recrystallized grains and the mechanism by which quartz was dynamically recrystallized. These grain sizes were employed to estimate differential stress using three calibrated piezometers. The differential stress estimates were in turn used in conjunction with deformation temperatures to estimate strain rates for deformation of quartzite aureole rocks using wet-quartzite flow laws.

In Chapter 3, *"Using structure contour maps to analyze subsurface 3D fault geometry along segments of the Moine thrust zone, NW Scotland"*, we constructed structure contour maps along the mapped trace of the Moine thrust from the North Coast to the Dundonnel area to analyze the three-dimensional subsurface fault geometry in the region. Additionally, we applied this technique to investigate the Glencoul thrust 'controversy' in the northern part of the Assynt culmination, where the structural positions of the Glencoul thrust and Ben More thrust have been the subject of recent debate. Structure contours on the Glencoul thrust surface were constructed in this region to evaluate the lateral continuity of the Glencoul thrust surface.

CHAPTER 2

Stress and strain rate estimates associated with penetrative deformation of the Harkless quartzite aureole rocks, Papoose Flat Pluton, eastern California

N.D. HEAVERLO[1], R.D. LAW[1]

[1]*Department of Geosciences, Virginia Polytechnic Institute and State University, Blacksburg, Virginia, 24061, USA*

Abstract

Past attempts to quantify stress and strain rates associated with pluton emplacement have concentrated on measuring strains in aureole rocks and attempting to quantify duration of deformation via numerical models of pluton/wall rock cooling. Cambrian age Harkless quartzites located along the western margin of Papoose Flat pluton, White-Inyo Mountains, California, were thinned and dynamically recrystallized to as little as 10% of their regional stratigraphic thickness during pluton emplacement.

Previous experimental and theoretical studies have quantified relationships between dynamically recrystallized grain size, recrystallization regime, and corresponding differential flow stresses and strain rates. Dynamically recrystallized quartz grain sizes and microstructures preserved in naturally deformed rocks can therefore be used to estimate differential flow stress and, in combination with appropriate flow laws, strain rates in the rock.

Microstructure analysis indicates that recrystallization of Harkless quartzite occurred by grain boundary migration with mean recrystallized grain size ranging from 86-225 μm. Only grain sizes up to ~120 μm were considered in differential stress and strain rate estimations. Application of three calibrated piezometers results in differential stress estimates between ~11 and ~29 MPa. Published wet-quartzite dislocation creep flow laws combined with deformation temperature, water fugacity, and differential stress estimates, provide strain rates that range from 1.2×10^{-14} s^{-1} to 2.3×10^{-12} s^{-1}. The faster strain rate estimates are in agreement with strain rates indicated by numerical cooling models within the pluton's contact aureole.

2.1 Introduction

Only a few studies of mid-crustal plutons have attempted to quantify the stress and strain rates of deformation related to forcible pluton emplacement. Past research has suggested that strain rates associated with aureole rock deformation vary between 10^{-8} and 10^{-12} s^{-1} (Karlstrom et al., 1993; Miller and Paterson, 1994; Nyman et al., 1995; Fernandez and Castro, 1999; McCaffrey et al., 1999; Albertz et al., 2006). These rates are several orders of

magnitude faster than typical geologic strain rates of 10^{-13} to 10^{-15} s^{-1} (Pfiffner and Ramsey, 1982). No study, to our knowledge, has used published grain size piezometers or wet-quartzite flow laws to estimate strain rates associated with pluton emplacement. This is likely because high strains associated with forcible emplacement typically are not preserved in aureole rock microstructures at relatively close structural distances to the pluton margin. These preservation issues typically occur as a result of either mechanical processes, such as assimilation and stoping of aureole rocks (Paterson and Vernon, 1995) or grain boundary area reduction processes that may occur during dynamic recrystallization or after deformation has ceased (static annealing), resulting in the removal or complete recrystallization of microstructures.

Aureole rocks along the western margin of the Papoose Flat pluton, eastern California, have been plastically deformed and thinned to only 10% of their regional stratigraphic thickness, with no field evidence for stoping or assimilation processes (Sylvester et al., 1978). Nyman et al. (1995) incorporated the amount of stratigraphic thinning into simple 1D thermal cooling models to estimate strain rates on the order of 10^{-12} s^{-1} associated with the emplacement and deformation of aureole rocks surrounding the western margin of the pluton. This study will use the grain sizes of dynamically recrystallized microstructures preserved in the relatively pure (with minor accessory phases) Harkless quartzites to estimate differential stress and strain rates associated with emplacement of Papoose Flat pluton and compare these strain rate estimates with strain rates indicated by thermal modeling (Nyman et al., 1995). The simple PT history of quartzites in the contact aureole of the Papoose Flat pluton, compared to multiply deformed terranes with complex P-T-D histories, make them ideal candidates for quartz piezometry and strain rate estimates.

Optically measured grain sizes were employed to determine differential stresses associated with forcible emplacement and syn-magmatic deformation of the aureole rocks using three calibrated piezometers. We use these differential stress estimates, along with published deformation temperatures obtained from calcite-dolomite thermometry (Nyman et al., 1995) and quartz c-axis fabric opening angles (Law et al., 1992), to estimate strain rates using wet-quartzite flow laws.

In most studies, these differential stress and strain rate estimates are calculated with a single piezometer-flow law relationship, without discussion of alternative estimates obtained by using other published calibrations. Given the relatively simple deformation history under which the quartzites surrounding the western margin of Papoose Flat pluton were dynamically recrystallized, these rocks provides an ideal case study site to investigate discrepancies in differential stress and strain rate estimates obtained when different combinations of piezometer-flow laws are applied.

2.2 Geologic Background

The Papoose Flat pluton is a Late Cretaceous quartz monzonite with K-feldspar megacrysts (Ross, 1965; Sylvester et al., 1978) located in the White-Inyo Mountains of eastern California. It is part of a Mesozoic suite of granitic plutons considered to be tectonically linked to the Sierra Nevada Batholith (Bateman et al., 1963; Ross, 1965; 1969), located ~20 km to the west (Figure 2.1). The Papoose Flat pluton is one of the youngest plutons in the range, with a U-Pb monazite age of 83.1 ± 0.4 Ma (Miller, 1996). This age is coincident with a period of Late Cretaceous magmatism and regional dextral strike-slip movement along NW-trending shear zones in the Sierra Nevada magmatic arc (Tobisch et al., 1995; Greene and Schweikert, 1995; Tikoff and Saint-Blanquat, 1997; Saint-Blanquant et al., 1998; Glazner et al., 2004; Bartley et al., 2007) and along the western flank of the White-Inyo Range (Vines, 1999, Sullivan and Law, 2007).

The White-Inyo Range is a NW-trending horst block that is bounded to the west by high-angle Cenozoic normal faults in Owens Valley and to the east by normal faults and dextral oblique slip faults in Eureka Valley, Fish Lake, and Saline Valley (Nelson, 1992) (Figure 2.2). The Inyo Range is composed of essentially unmetamorphosed Cambrian and pre-Cambrian sedimentary rocks (Figure 2.3) that are folded around the S-plunging Inyo Anticline and locally metamorphosed around pluton margins (Nelson, 1962; Ernst et al., 1993). The Papoose Flat pluton was forcibly emplaced as a dike-fed laccolith (Morgan et al., 1998) into the southwest

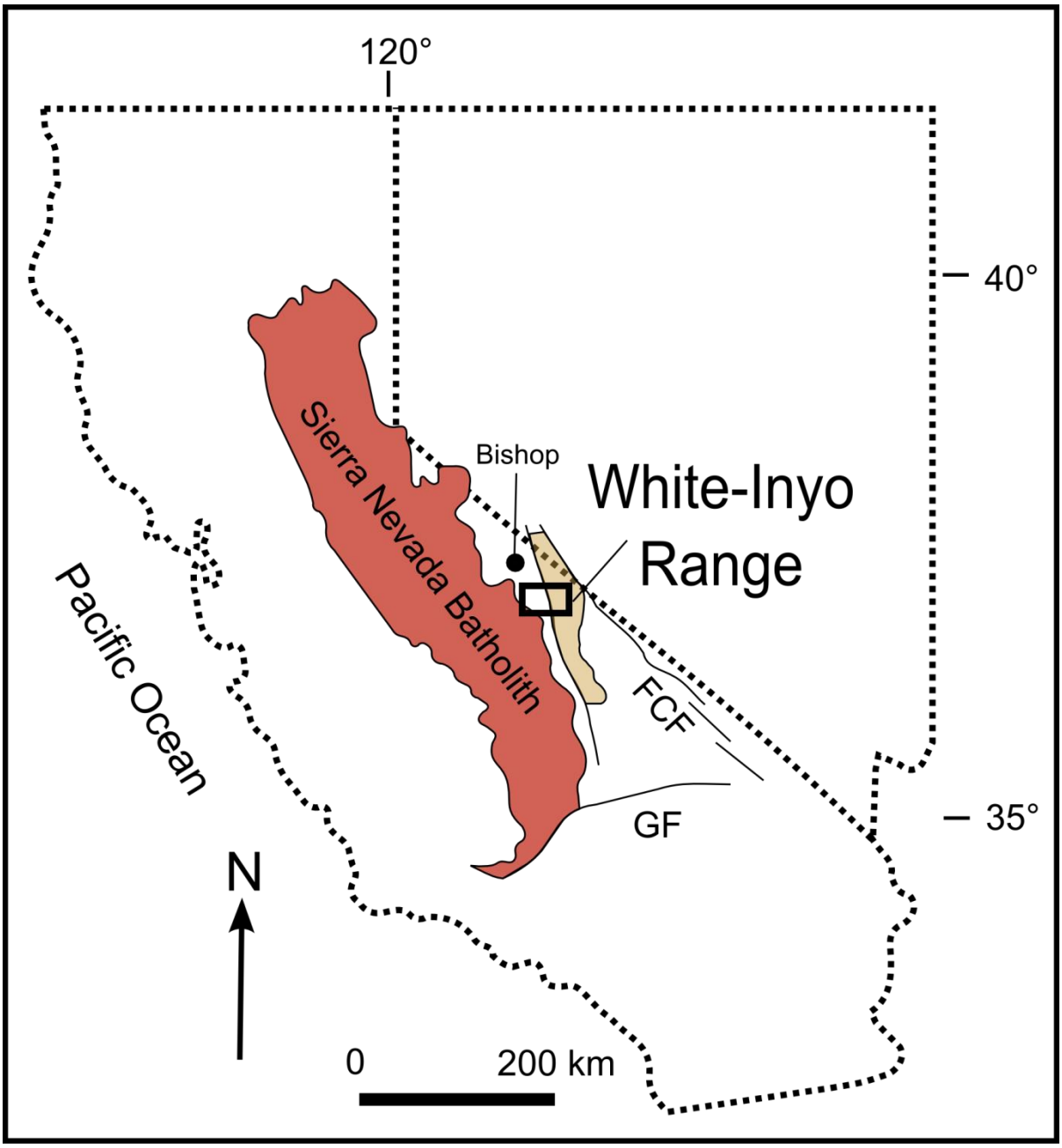

Fig. 2.1. Simplified regional geologic map of eastern California showing location of the White-Inyo Range in relation to the Sierra Nevada Batholith located ~20 km west. Black box designates location of the study area. FCF-Furnace Creek fault, GF-Garlock fault. Figure modified from Saint-Blanquat et al. (2011).

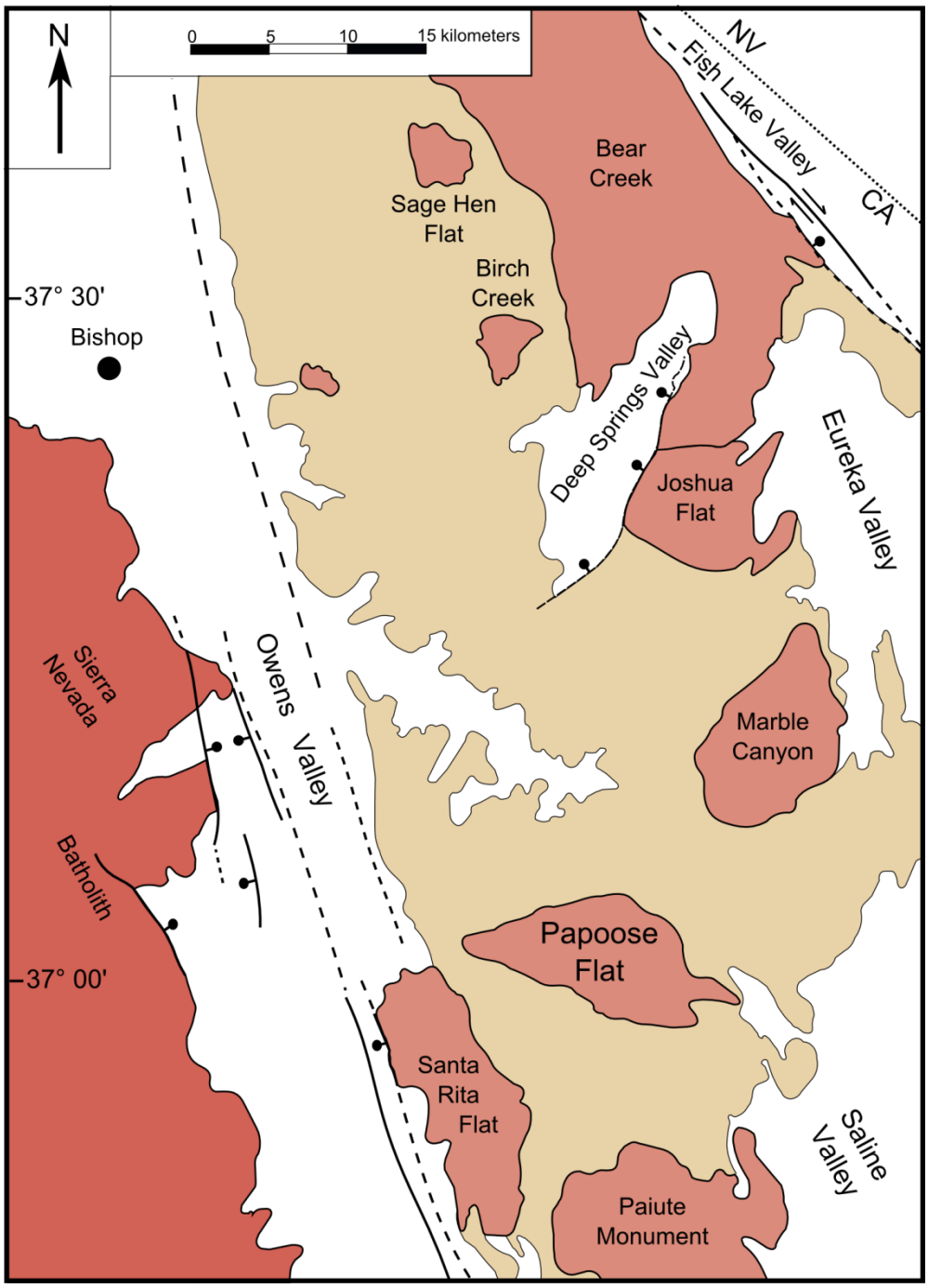

Fig 2.2. Simplified geologic map showing Mesozoic intrusions of the White-Inyo Range and location of Papoose Flat pluton. The White-Inyo range is bound to the west by Cenozoic normal faults in Owens Valley and to the east by normal and dextral slip faults in Fish Lake, Eureka, and Saline Valley. Figure modified from Law et al. (1992).

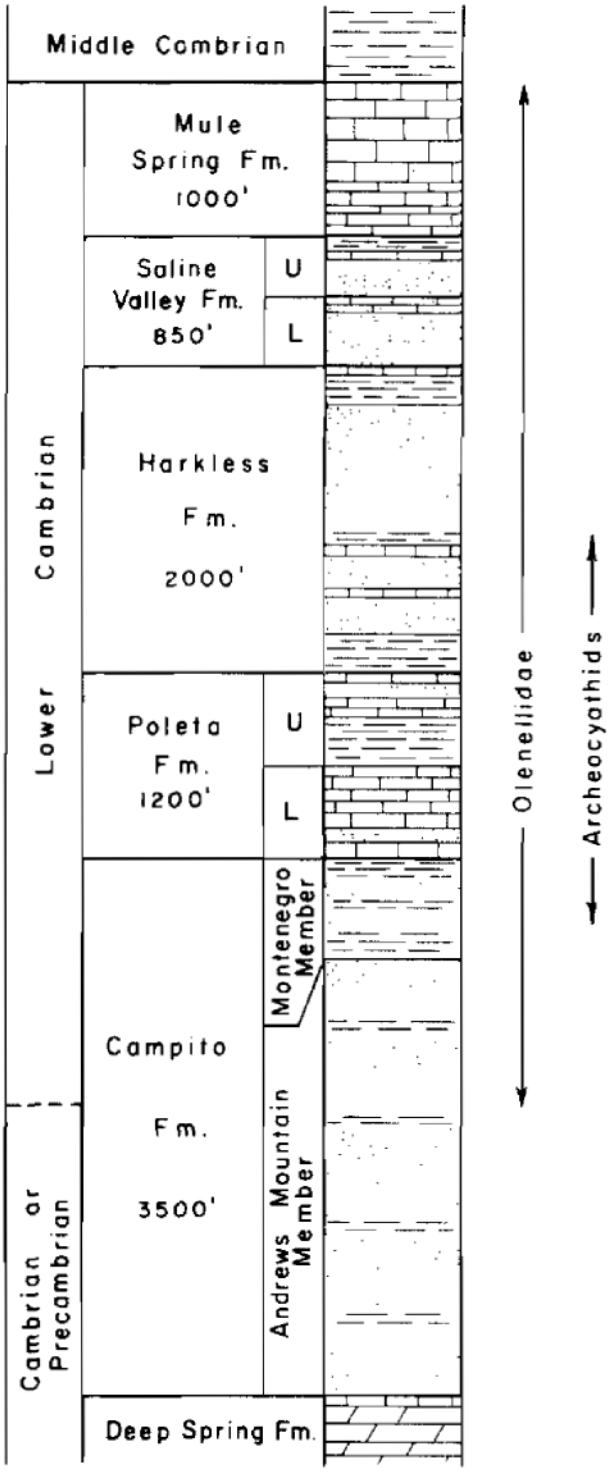

Fig. 2.3. Generalized stratigraphic column of the Cambrian and Pre-Cambrian sedimentary rocks exposed in the White-Inyo Range. Figure from Nelson (1962)**.**

limb of the Inyo-Anticline at a crustal depth of ~12-15 km (Saint-Blanquat et al., 2001), locally deforming and deflecting the pre-Cambrian and Cambrian sediments to the west (Figures 2.4, 2.5) (Nelson et al., 1978; Sylvester et al., 1978). Pressure estimates for emplacement vary between ~3.5 and 4.0 kbar (Nyman et al., 1995).

The pluton-aureole rock contacts along the western and eastern margins of the pluton exhibit strikingly different field relationships. Along the western margin, an outer carapace of the pluton known as the gneissic border facies is concordant with the aureole rocks for ~20 km (Nelson et al., 1972, 1978; Sylvester et al., 1978; Morgan et al., 1998). These aureole rocks have been metamorphosed (marble, quartzite, schist) and plastically deformed and thinned by up to 90%, now measuring only 10% of their regional stratigraphic thickness (Figure 2.4) (Nelson et al., 1972; Sylvester et al., 1978). Palinspastic restoration of the aureole rocks shows that during emplacement the pluton inflated vertically by ~ 2 km, while deflecting and thinning the aureole rocks along its western margin (Morgan et al., 1998). Contrastingly, the eastern margin pluton-aureole rock contact is discordant with virtually no strain accumulated along the pluton margin or in the aureole rocks surrounding the pluton (Figures 2.5, 2.6).

Foliation and lineation in the aureole rocks along the western pluton margin are parallel to foliation and lineation observed in the pluton's gneissic border facies (Law et al., 1992). Lineation data within both the aureole rocks and gneissic border facies along the western margin indicate that plastic deformation occurred synchronous with pluton inflation (Saint-Blanquat et al., 2001). Quartz fabric analysis of the Lower Cambrian Harkless Formation quartzites around the western part of the pluton indicate that the stretching lineation is associated with km-scale domains of top to the SE and top to the NE shear senses, although top to the SE shear senses are dominant (Morgan, 1992; Law et al., 1992; 1993).In contrast, the eastern margin of the pluton displays a vertical linear fabric and the aureole rocks lack any major fabric development (Sylvester et al., 1978).

Morgan et al. (1998) proposed a two-stage model for pluton emplacement based on the relationship between andalusite porphyroblast growth and development of macroscopic

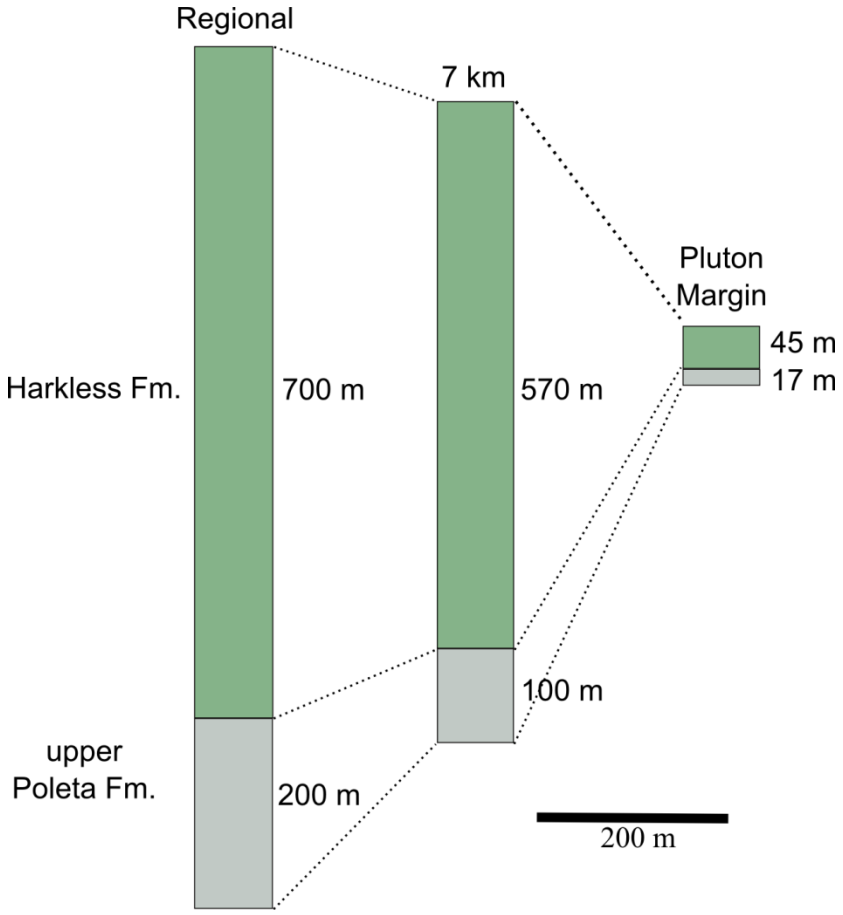

Figure 2.4. Schematic stratigraphic columns showing average regional geologic thicknesses of the Harkless and upper Poleta Formations, compared to the average stratigraphic thicknesses at 7 km from the Papoose Flat pluton, and attenuated stratigraphic thicknesses on the western margin of the pluton. The Harkless Formation is composed of quartzite and schists. The upper Poleta Formation is composed of marble. Figure modified from Sylvester et al. (1978).

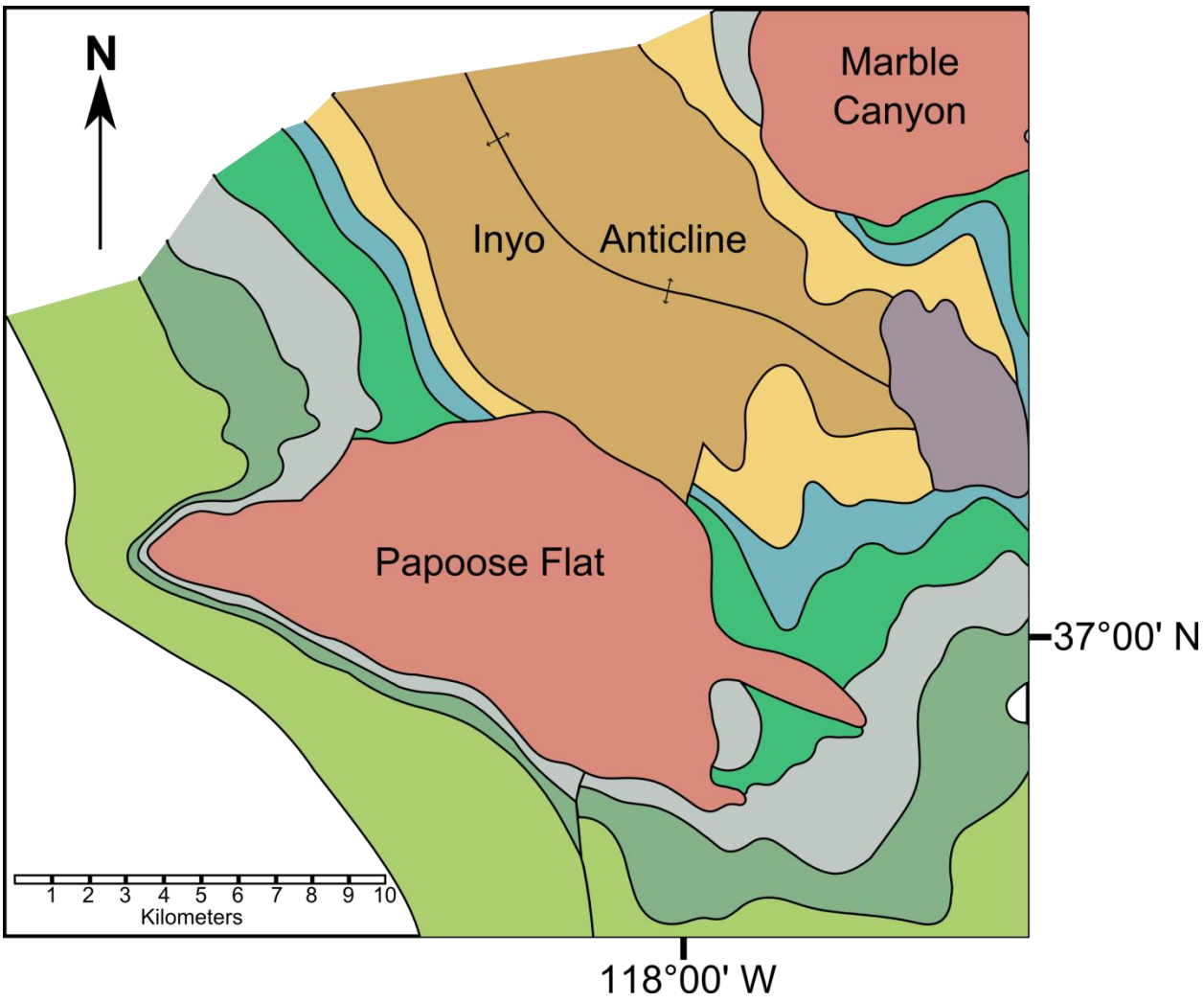

Fig 2.5. Simplified geologic map showing position of Papoose Flat pluton in the SW limb of the Inyo Anticline. Aureole rocks on the western pluton margin have been plastically deformed and strained to 10% of their regional stratigraphic thickness. Figure modified from A.G. Sylvester website at http://www.geol.ucsb.edu/faculty/sylvester/PAPOOSE/PFpages/PFgeolmap1.html

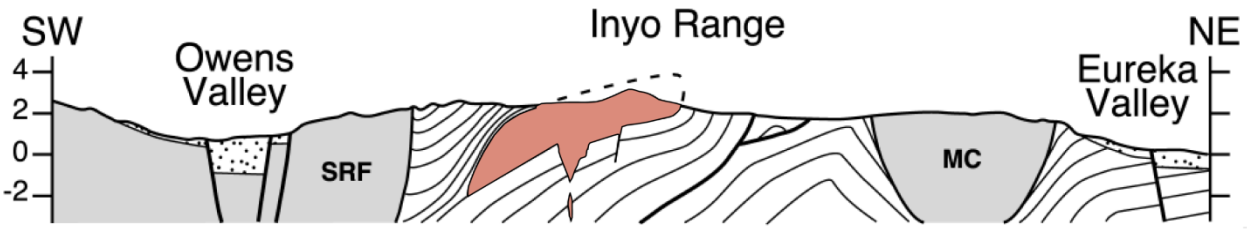

Fig 2.6. SW-NE Cross-section through the White-Inyo Range from SW to NE showing the concordant margin of Papoose Flat pluton (pink) with thinned strata deflected to the west, along the western margin of the pluton. The eastern margin of the plutonshows a cross-cutting relationship with stratigraphy and a lack of strain developed in the aureole rocks. Figure adapted from Saint-Blanquat et al. (2001).

structures within the Harkless Formation schist. Additionally, compositional zoning of silicate and magnetic minerals within the granitic pluton body suggests that the pluton evolved through injection of multiple magma pulses (Saint-Blanquat et al., 2001).

Thermal modeling of the pluton's cooling history indicates that a time-averaged strain rate of ~$10^{-12}s^{-1}$ likely occurred in at least the inner margin of the aureole (Nyman et al., 1995). Strain rates were modeled using the heat flow equation for a rectangular-shaped pluton from Buntebarth (1984). An assumed magma temperature of 850˚ C, with a solidus of 650˚ C was used. The initial wall rock temperature was assumed to be at 250˚ C, based on an emplacement depth of ~10 km and a geothermal gradient of 25˚ C km^{-1}. This modeling assumes that the pluton was formed from a single magma pulse that stretched the surrounding country rocks in the pluton's aureole. Additional modeling by Nyman et al. (1995; their fig. 8a) indicates that if elevated temperatures are maintained by the input of successive magma pulses, the observed 90% thinning of stratigraphic units along the pluton's western margin could have been achieved at slower strain rates. . Further modeling by Saint Blanquat et al. (2001) estimated total duration for pluton development, from initial sill emplacement to final crystallization to be ~30,000 years.

2.3 Microstructures

Dynamically recrystallized quartz microstructures produced under known experimental conditions (Hirth and Tullis, 1992) have also been recognized in naturally deformed rocks (Dunlap et al., 1997; Stoeckhert et al., 1999; Stipp et al., 2002a, b, 2010). Three different recrystallization microstructures can form as a result of changes in strain rate and/or deformation temperature. These microstructures in naturally deformed quartzites are: grain boundary bulging (BLG), formed at relatively high strain rates and/or low temperatures; subgrain rotation (SGR), formed under medium strain rate and/or temperature conditions; and grain boundary migration (GBM), formed at relatively low strain rates and/or high temperatures (Stipp et al., 2002b). These microstructures broadly correlate to the three dislocation creep regimes for quartz, identified by Hirth & Tullis (1992) - but cf. Stipp et al.

(2002b) and review by Law (in press). In naturally deformed rocks, transitional recrystallization regimes are often observed, with the presence of at least two recrystallization microstructures, one dominant over the other (Stipp et al., 2002a; this study).

In their study of natural quartzites along the Tonale Fault Zone (Italian Alps), Stipp et al. (2002b) recognized two separate classes of GBM based on the relationship between accessory phase phyllosilicates and dynamically recrystallized quartz grains. The relatively low temperature, GBM I, is identified by quartz microstructures that are pinned by phyllosilicates, with spacing between phyllosilicates controlling quartz grain growth during dynamic recrystallization. The relatively high temperature, GBM II, is distinguished by quartz grains growing without impedance from second phase minerals (phyllosilicates) on grain boundary growth.

Previous microstructural work completed on the plastically deformed aureole rocks along the western margin of Papoose Flat pluton has focused on quartz fabrics (Law et al., 1992) and deformation temperatures associated with pluton emplacement and deformation (Nyman et al., 1995). Law et al. (1992) documented preferred alignment (S_B) of dynamically recrystallized grains oblique to the macroscopic mylonitic foliation (S_A) defined by phyllosilicates in some Harkless quartzite samples that indicated a dominant top-to-the SE shear sense. In all samples shear sense inferred from oblique grain shape alignments was confirmed by asymmetry of single and cross-girdle (transitional between Type 1 and 2, *sensu* Lister, 1977) c-axis fabrics.

Samples analyzed in this study were collected by R.D. Law and S.S. Morgan during field seasons in 1990-1991. Our analyses were completed on Harkless quartzites, collected from the western aureole of Papoose Flat pluton, along traverses oriented perpendicular to the pluton margin (Figure 2.7). Thin sections were cut perpendicular to macroscopic foliation and parallel to stretching lineation (XZ plane). In most cases, sample traverse names correspond to the Law et al. (1992) traverse descriptions (their Traverse B, C, D, and E). Traverses not described by Law et al. (1992) are named according to sample location numbers (Location 26, 46), recorded on the field topographic map by R.D. Law and S.S. Morgan.

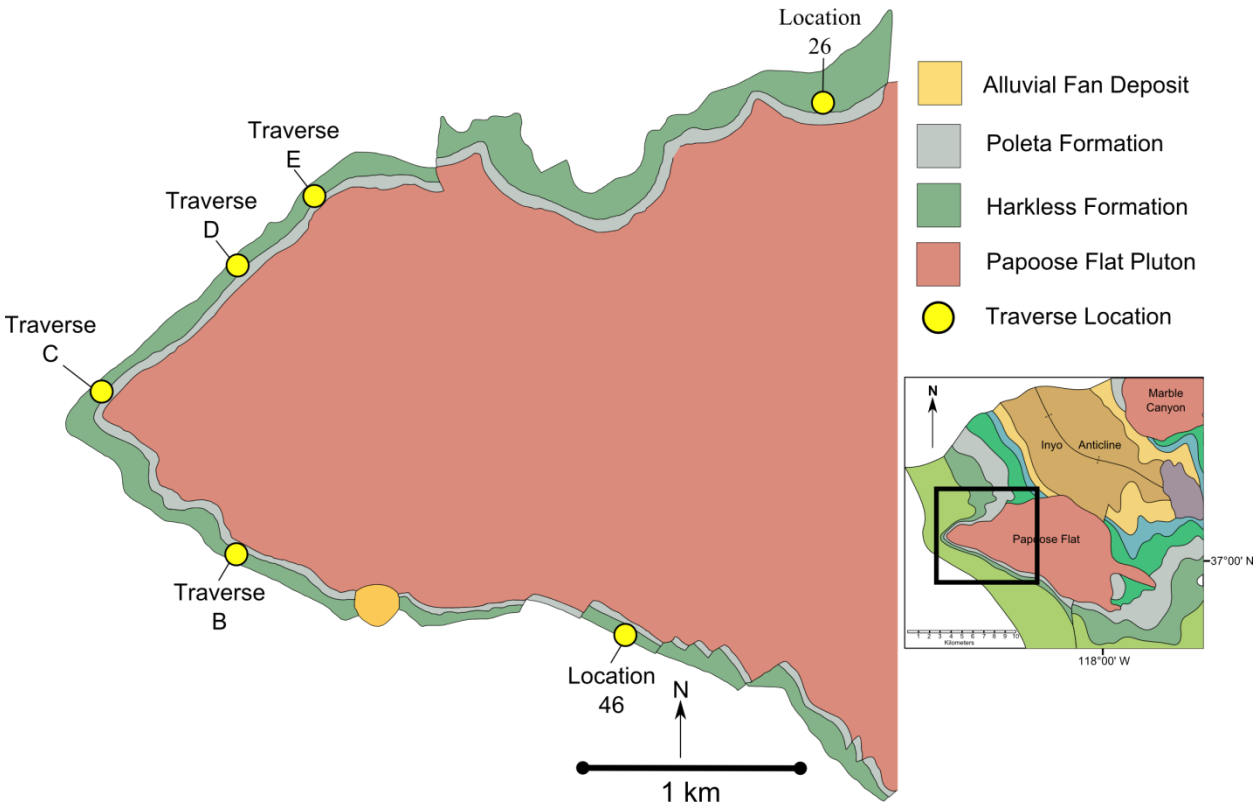

Fig. 2.7. Simplified geologic map showing location of samples collected from the Harkless Formation quartzites along western margin of the Papoose Flat pluton. Figure adapted from Law et al. (1992).

All quartz grains in the samples from the Harkless Formation quartzites have been dynamically recrystallized by GBM I/II with minor amounts of transitional SGR/GBM microstructures, whose significance we will discuss later. Large lobate and sutured grain boundaries are typical microstructures in these dynamically recrystallized quartzites. In areas of relatively high mica concentration, pinning of quartz grain boundaries, parallel to the main quartzite foliation is common throughout the samples. Even in cases where GBM I dominates in the Harkless quartzite samples, there are GBM II microstructures with phyllosilicate trails included within large quartz grains, indicative of a transitional regime within GBM.

In samples collected near the pluton margin, possible dissection microstructures or island grains (sensu Urai et. al., 1986) are present, and in some cases the samples exhibit a foam texture with polygonal grain boundaries that intersect at 120˚ triple junctions. This microstructure is characteristic of grain boundary area reduction (GBAR) processes that may occur as a result of: dynamic recrystallization (syn-deformation), static annealing (post-deformation), or by a combination of the two processes (Heilbronner and Tullis, 2002; Passchier and Trouw, 2005). While it is important to draw a distinction between these processes, both result in an increase in grain size and polygonal grain 'foam' textures, making it difficult - if not impossible - to differentiate between these mechanisms based on microstructures. In consideration of this problem, samples displaying this grain fabric will be referred to as either displaying a 'foam' texture after Passchier and Trouw (2005) or as a grain boundary area reduction (GBAR) microstructure, for the remainder of this chapter.

2.3.1 Traverse B

Traverse B (Figure 2.8) is located along the SW margin of the pluton. GBM microstructures indicated by large lobate grain boundaries are present in all samples. PF-135, located 10.9 m from the pluton margin, exhibits GBM II microstructures with an abundant number of grains with a foam texture. PF-136, located 15.8 m from the margin, exhibits GBM II microstructures,

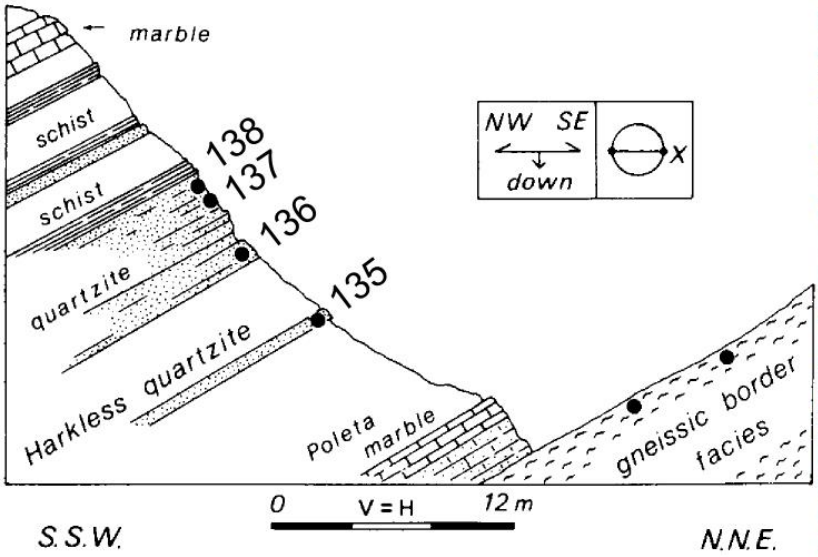

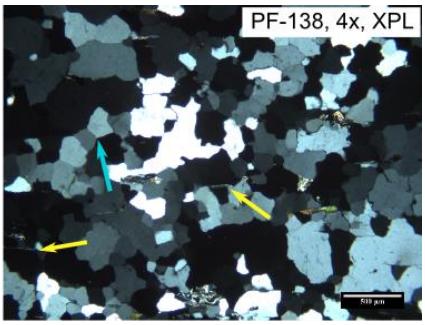

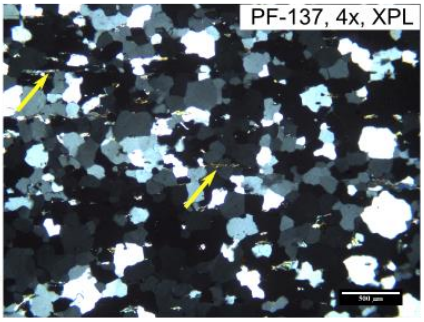

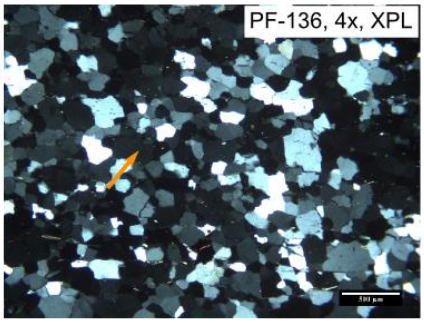

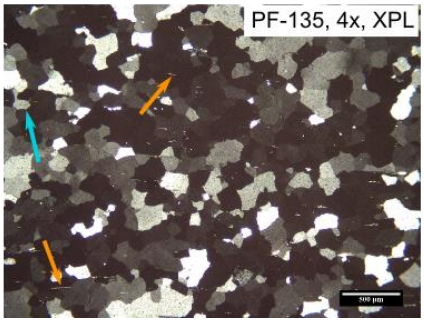

Fig 2.8. Cross-section along Traverse B. Photomicrographs on the right are arranged in order of proximity to the pluton margin (bottom image is closest to the margin). Orange arrows indicate phyllosilicates included within quartz grains, indicative of GBM II microstructures. Light blue arrows indicate GBAR microstructures (?), and yellow arrows indicate phyllosilicates controlling grain boundary migration; indicative of GBM I. This microstructural relationship indicates a decrease in temperature or strain rate as we move away from the pluton margin. Mean grain sizes and structural distance of each sample from the pluton margin can be found in Table 2.1. All photomicrograph scale bars at 500 µm. Figure adapted from Law et al. (1992).

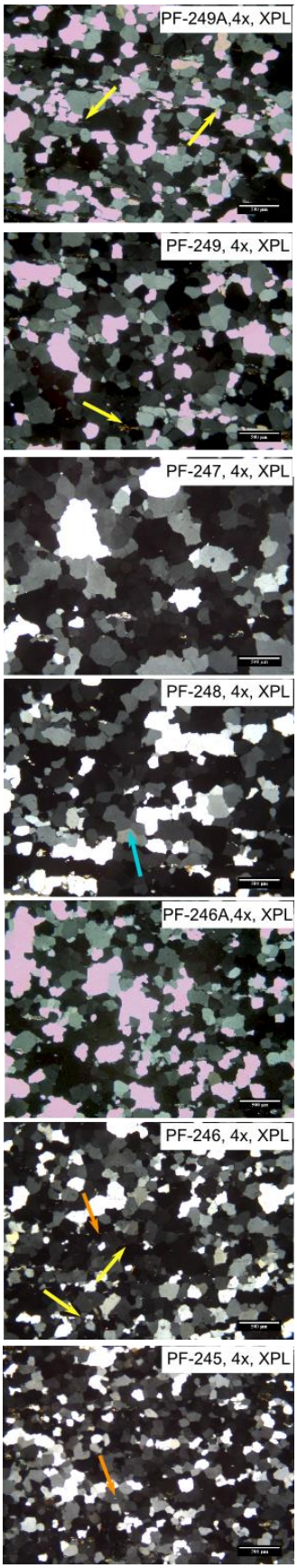

Fig 2.8 (continued). Cross-section along Traverse B (extension). Photomicrographs on the left are arranged in order of proximity to the pluton margin (bottom image is closest to the margin). Yellow arrows indicate phyllosilicates controlling grain boundary migration; indicative of GBM I, orange arrows indicate phyllosilicates included within quartz grains; indicative of GBM II microstructures, and light blue arrows indicate GBAR microstructures. Mean grain sizes and structural distance of each sample to the pluton margin can be found in Table 2.1. All photomicrograph scale bars at 500 µm.

with relatively fewer annealed grains than the previously described sample. The locally observed decrease in GBAR microstructures is likely due to the increased structural distance from the pluton margin. In sample PF-137, located 18.9 m from the pluton margin, a transition to GBM I microstructures is observed. Grain boundaries are pinned by phyllosilicates, which define foliation in the sample. PF-138, located 19.9 m from the pluton margin displays GBM I microstructures with minor amounts of GBAR grains. The transition from GBM II (PF-136) to GBM I (PF-137,138) microstructures are interpreted to be thermally controlled, based on the distances between the samples and the pluton margin.

2.3.2 Traverse C

Traverse C (Figure 2.9) is located at the western-most map position of the pluton margin. All samples exhibit GBM II microstructures. PF-90, 504, and 505 are all located in essentially the same structural position in the aureole at 23.2 m from the pluton-wall rock contact, and yet display different recrystallization microstructures. A comparison between PF-505 and PF-90, 504 shows that PF-505 grains are much more lobate and amoeboid in shape. PF-505 exhibits GBM II microstructures with island grains, but lacks GBAR microstructures. PF-90 also displays GBM II microstructures with possible island grains, and grain boundary area reduction is much more common than in the other two samples from the same structural position. PF-90 exhibits GBM II microstructures and island grains, but lacks GBAR grains. PF-89, located 25.3 m from the pluton margin displays GBM II microstructures with island grains and PF-88, located 39.6 m from the pluton margin displays GBM II microstructure with relatively larger grain sizes than the structurally lower PF-88. All samples located along this traverse display GBM II microstructures. This traverse displays the clearest evidence for grain boundary area reduction processes compared to any of the other traverses analyzed around the pluton margin.

2.3.3 Traverse D

Traverse D is located along the NW margin of the pluton (Figure 2.10). PF-73, the sample collected closest to the pluton margin (22.7 m), exhibits GBM II microstructures with foam

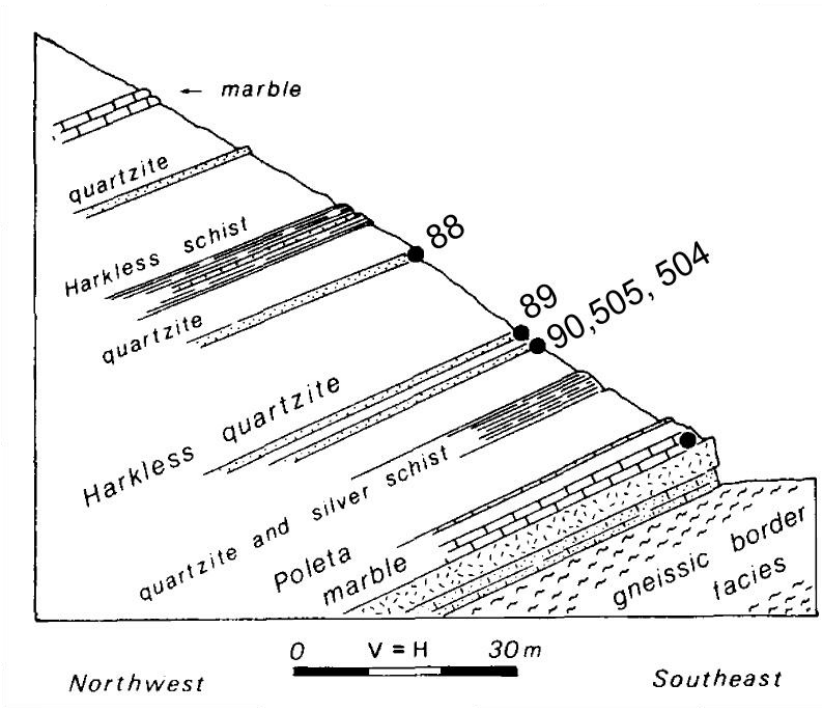

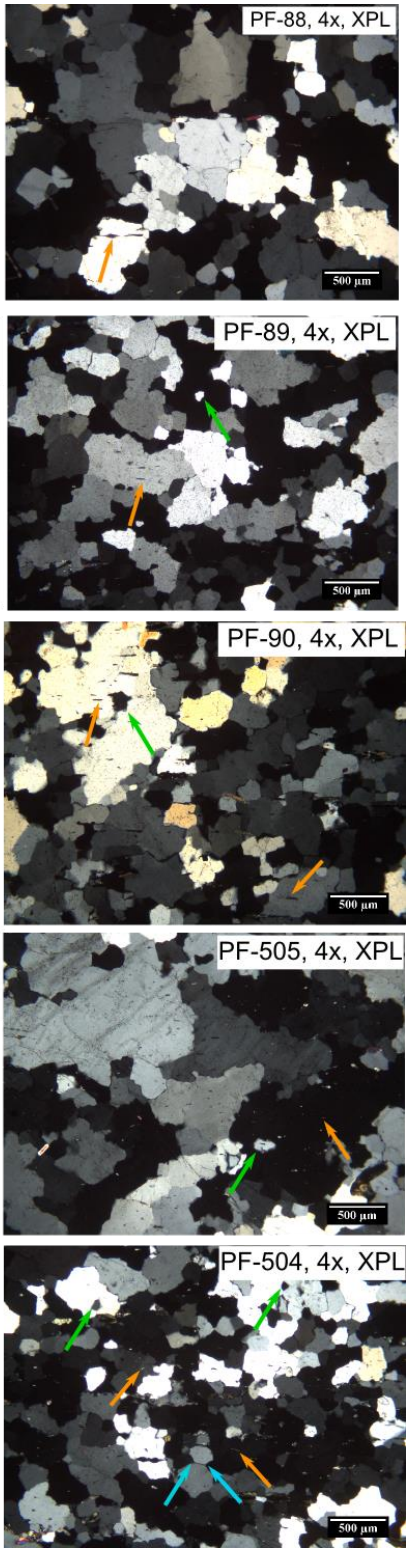

Fig 2.9. Cross-section along Traverse C. Photomicrographs on the right are arranged in order of proximity to the pluton margin (bottom image is closest to the margin). Green arrows indicate possible island grain microstructures, orange arrows indicate phyllosilicates included within quartz grain grains; indicative of GBM II microstructures, and light blue arrows indicate GBAR microstructures. Mean grain sizes and structural distance of each sample to the pluton margin can be found in Table 2.1. All photomicrograph scale bars at 500 µm. Figure adapted from Law et al. (1992).

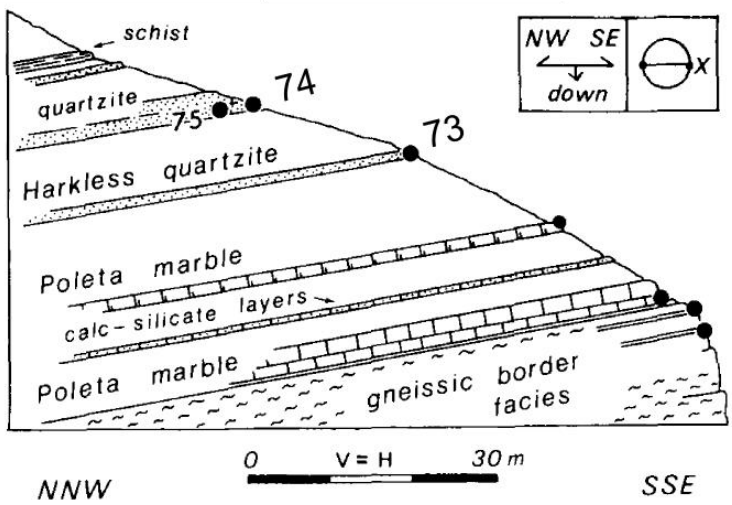

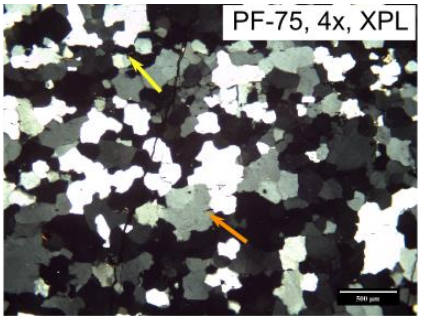

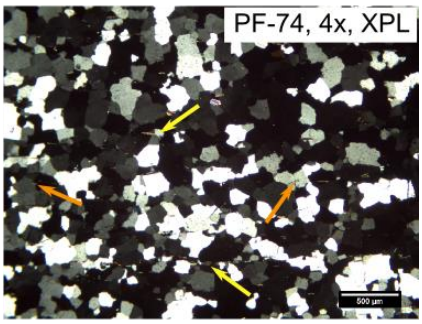

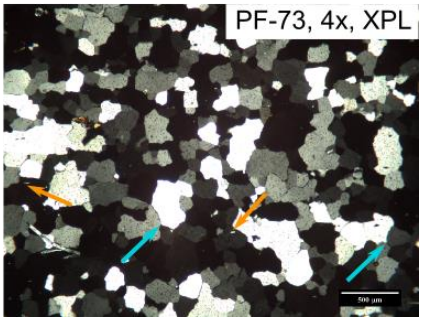

Fig 2.10. Cross-section along Traverse D. Photomicrographs on the right are arranged in order of proximity to the pluton margin (bottom image closest to the margin). Yellow arrows indicate phyllosilicates controlling grain boundary migration; indicative of GBM I, orange arrows indicate phyllosilicates included within quartz grain grains; indicative of GBM II microstructures, and light blue arrows indicate potential GBAR microstructures. Mean grain sizes and structural distance of each sample to the pluton margin can be found in Table 2.1. All photomicrograph scale bars at 500 µm. Figure adapted from Law et al (1992).

texture and 120˚ triple junctions. Moving to a structurally higher position within the pluton aureole (PF-74,75), GBM I/II transitional microstructures are observed, along with a decrease in presence of GBAR microstructures. This transition to GBM I at the higher structural position likely indicates a decrease in temperature.

2.3.4 Traverse E

Traverse E is located along the NW margin of the pluton (Figure 2.11). PF-77, located 34.0 m from the pluton margin, was the only quartzite sample collected along this traverse. It displays GBM II microstructures with phyllosilicates included within grains. Possible island grain structures are present. These could also be interpreted as SGR microstructures, but given the lobate nature of the surrounding grains with the inclusion of phyllosilicates, it is not likely that SGR microstructures were produced.

2.3.5 Location 26

Location 26 (Figure 2.12) is situated on the northern margin of the pluton. Two samples were analyzed from this location. No data were available for correlating samples to structural distance from the pluton margin. PF-105 displays transitional SGR/GBM recrystallization microstructures. This is the only sample where SGR microstructures are so abundant. Microstructures are pinned by phyllosilicates, indicating GBM I recrystallization. Because this is the only known quartzite sample that displays these microstructures, the SGR microstructures in this sample are interpreted to be overprinting microstructures that have developed after deformation under relatively low temperature conditions. However, they may have also formed due to an increase in strain rate and overprint of syn-deformational GBM microstructures. PF-109 displays GBM I microstructures with few microstructures indicative of GBAR.

2.3.6 Location 46

Location 46 (Figure 2.13) is situated on the southern margin of the pluton. Structural distance data were not available for this traverse. Recrystallization is dominated by GBM I and II microstructures. PF-171 exhibits possible SGR microstructures. Because of the GBM II

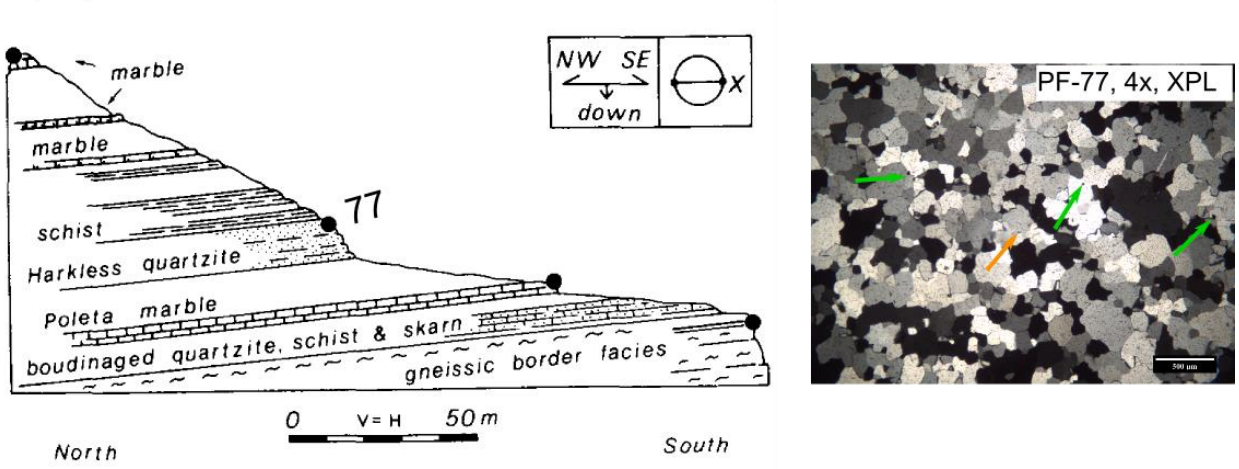

Fig. 2.11. Cross-section along Traverse E. Green arrows indicate possible island grain microstructures (?) and orange arrows indicate phyllosilicates included within quartz grains; indicative of GBM II microstructures. Mean grain size can be found in Table 2.1. Photomicrograph scale bar at 500 µm. Figure adapted from Law et al. (1992).

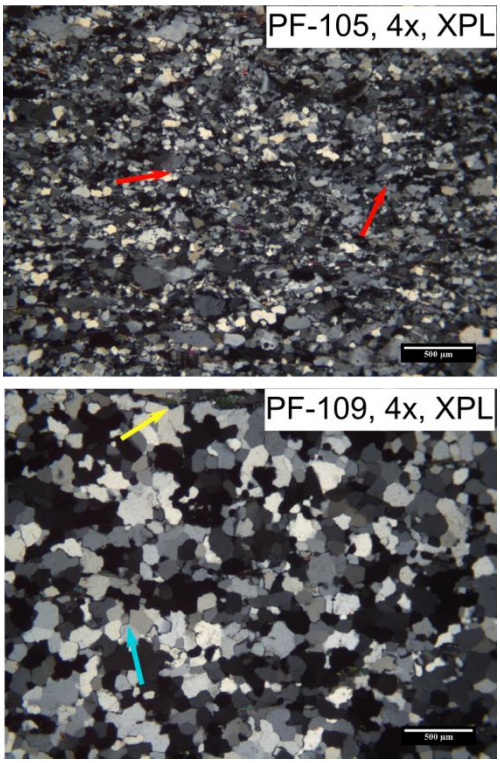

Fig 2.12. Location 26 microstructures. Structural distance data was not available for this traverse. Red arrows indicate possible SGR microstructures. Yellow arrows indicate phyllosilicates controlling grain boundary migration; indicative of GBM I, and light blue arrows indicate potential GBAR microstructures Mean grain sizes and structural distance of each sample from the pluton margin can be found in Table 2.1. All photomicrograph scale bars at 500 µm.

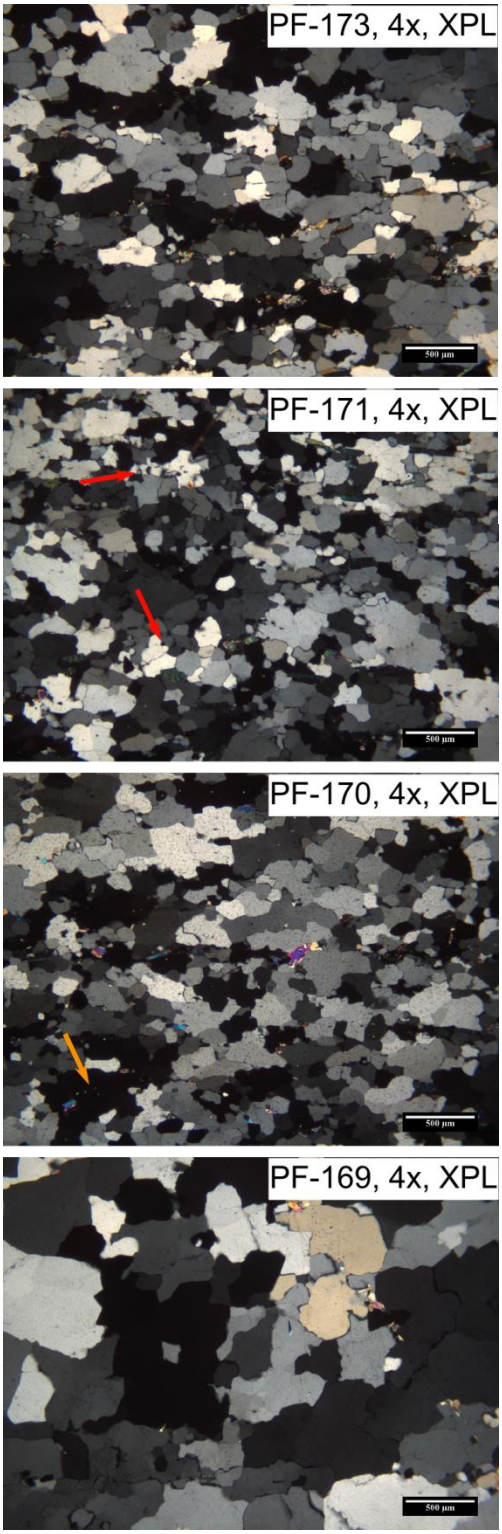

Fig 2.13. Location 46 microstructures. Structural distance data not available for this traverse. Orange arrows indicate phyllosilicates included within quartz grains; indicative of GBM II microstructures, and red arrows indicate possible SGR microstructures. Mean grain sizes and structural distance of each sample from the pluton margin can be found in Table 2.1. All photomicrograph scales at 500 µm.

microstructures present in other samples from this location, these microstructures are interpreted as being formed as a result of a pulse of high strain rate or due to increased structural position from the pluton margin; i.e. SGR microstructures overprinting syn-deformational GBM microstructures.

Samples PF-170, 171, and 173 all display more tabular grain shapes than all other traverse samples with grain long axes oriented perpendicular to foliation. PF-170 and 173 appear to be recrystallized by GBM I, but these are very pure quartzites that lack phyllosilicate grains so it is difficult to constrain the GBM sub-regime.

2.4 Quartz recrystallized grain size measurements

Quartz grain size measurements were completed on standard 30 µm thin sections cut perpendicular to macroscopic foliation and parallel to stretching lineation (XZ plane) following the analytical procedures of Stipp and Tullis (2003). Grain size measurements were completed using the grain boundary-linear intercept method of Smith and Guttman (1953), complying with grain size measurement techniques of Stipp et al. (2010) for quartz grains exhibiting SGR and GBM microstructures. The grain boundary-linear intercept method is our chosen method over other techniques (see Stipp et al., 2010) because it not only prevents bias by not allowing for "cherry picking" of easy to measure grains, but it is also the most time-efficient technique, when compared to other methods.

The linear intercept method involves placing a line of known length across a series of grains and dividing by the number of grain boundary intercepts along the line (Figure 2.14). Grain boundary measurements were completed using a linear intercept grid that was constructed with fixed transects oriented parallel, perpendicular, and oblique to the macroscopic foliation of the sample (Figure 2.15). Past studies (Stipp et al., 2002a,b; 2010) have only measured grains sizes along transects oriented parallel and perpendicular to the foliation. Due to the lobate, non-equant nature of the grains that characterize GBM microstructures, and the preferred shape (S_B) of dynamic recrystallized grains that are oblique to the main foliation (Law et al., 1992), measurements made oblique to the macroscopic foliation were implemented

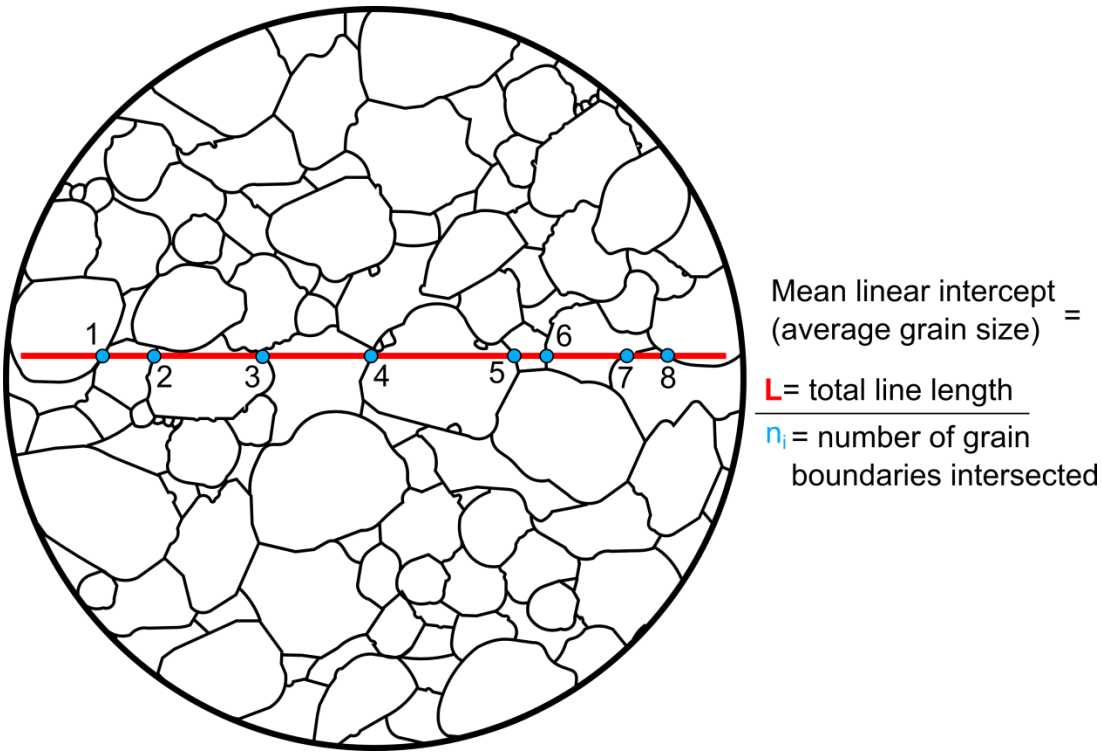

Fig 2.14. Diagram illustrating the grain boundary-linear intercept method of Smith & Guttman (1953) used to determine mean grain size. The drawing represents a schematic photomicrograph captured from the optical microscope. The equation used to calculate the average grain size along the transect line is shown to the right of the figure.

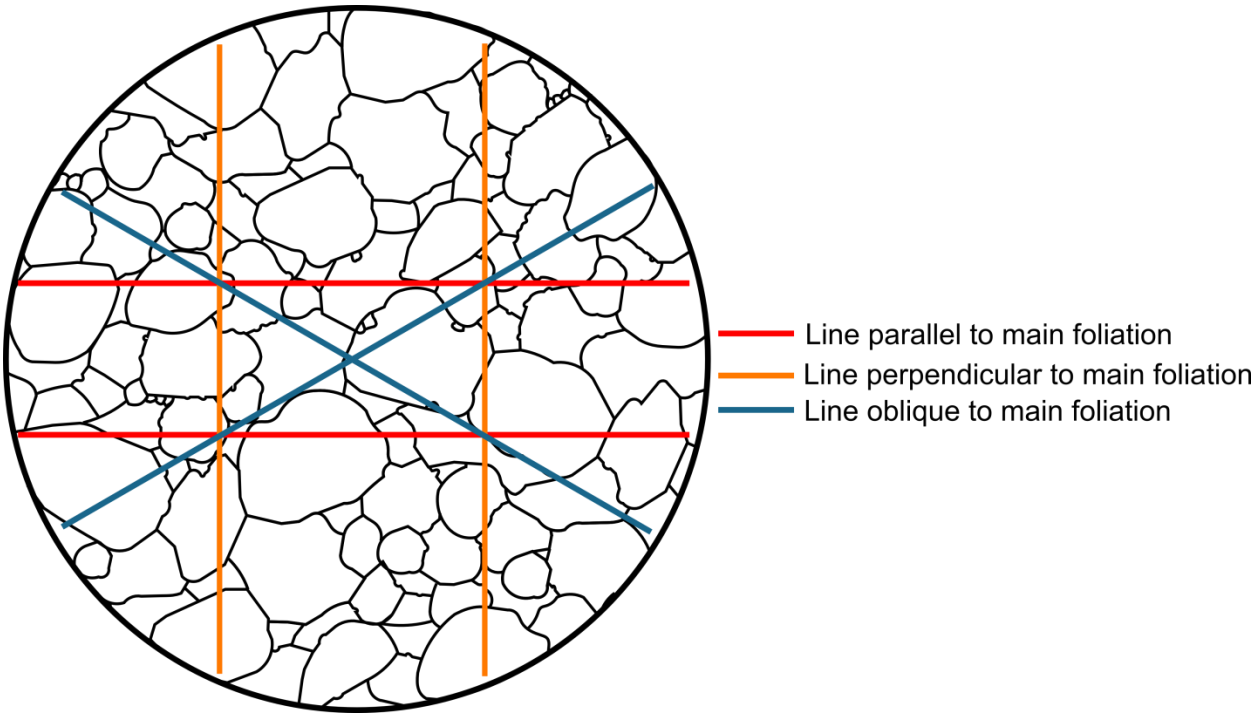

Fig. 2.15. Linear intercept transect grid with transect lines oriented parallel, perpendicular, and oblique to the macroscopic foliation. This grid was placed over three spatially different locations on the photomicrograph in order to more meaningfully estimate the representative grain size of the sample.

to more meaningfully constrain mean grain size. Grain sizes were measured using an optical microscope combined with photomicrographs. The linear transect grid was overlain on the photomicrograph using *ImageJ* software (Rasband, 1997-2014) Micrographs of quartz-rich rocks taken in cross-polarized light often convey a false impression of grain boundaries due to adjacent grains having similar extinction positions for particular orientations on the microscope stage. In order to more meaningfully determine the presence of grain boundaries that may not be obvious on the micrographs, refinements to the microstructures shown on the micrographs were made using different extinction positions on the rotating stage of the optical microscope. This allowed grain boundary relationships to be mapped on the photomicrographs at a finer scale. Three linear intercept grid measurements were completed on each sample, resulting in a minimum of 250 grains measured per sample. Following the analytical methods of Stipp and Tullis (2003), no stereological corrections were made to the measured grain sizes.

Quartz grain growth may be inhibited by secondary phase minerals such as mica and magnetite (Jessell, 1987) during both dynamic recrystallization and annealing processes (Tullis and Yund, 1982; Song and Ree, 2007), therefore grain size measurements were carried out in thin section areas that lacked abundant secondary phase mineral grains. Thin section analysis indicated that GBM II microstructures whose grain boundaries cut across pre-existing domains of phyllosilicates are not impacted by the secondary phase minerals, so measurements were still completed in these areas.

Following the analytical method of Stipp et al., 2002a, mean grain size diameter was calculated using the geometric mean for grain sizes measured perpendicular, parallel, and oblique to the macroscopic foliation. A summary of grain size measurements can be found in Table 2.1. There is no apparent relationship between dynamically recrystallized grain size and proximity to the pluton margin.

2.5 Deformation Temperatures

Peak temperatures of contact metamorphism were estimated using both calcite-dolomite thermometry (Nyman et al., 1995) and quartz c-axis fabric opening angle data

(reported by Law et al., 1992) combined with the Kruhl opening-angle thermometer (Kruhl, 1998). Peak temperatures of contact metamorphism acquired from Poleta Formation samples, using calcite-dolomite thermometry, range between between *c.* 460˚and 550 ˚C, depending on sample location along the western margin of the pluton. Deformation temperatures inferred from fabric opening angles are typically ~50 ˚C higher than temperatures in adjacent marble layers obtained by calcite-dolomite thermometry. The thermal aureole reaches a maximum width of ~600 m along the southern margin and narrows to ~ 60 m on the westernmost margin of the pluton (Nyman et al., 1995). In areas, where the outer extent of the thermal aureole could not be constrained by calcite-dolomite or quartz opening angle thermometry, it was determined by lack of silicate mineral phases in carbonate rocks sampled furthest from the contact, and by the first appearance of unstrained sedimentary structures traced outwards from the pluton margin (Nyman et al., 1995).

Dynamic recrystallization microstructures in the Harkless quartzites allow us to at least qualitatively evaluate deformation temperatures associated with pluton emplacement. In the Tonale Fault Zone study area described by Stipp et al. (2002a, b) the presence of SGR and GBM microstructures correlate with temperatures of contact metamorphism (associated with the Adamello pluton) in the ~400-500 ˚C (SGR) and >~500 ˚C (GBM) ranges. For the aureole of the Papoose Flat pluton, SGR and dominant GBM microstructures in the Harkless quartzites correlate with roughly similar temperatures indicated by calcite-dolomite thermometry and quartz c-axis fabric opening angles.

2.6 Differential stress estimates

Experimentally- (De Bresser et al., 1998; Stipp and Tullis, 2003) and theoretically- (Twiss, 1977; Shimizu, 2008) derived piezometers predict an inverse relationship between dynamically recrystallized grain size (D) and differential stress (σ). These piezometers provide a way to estimate differential stresses operating in plastically deformed and dynamically recrystallized rocks. BLG, SGR and GBM microstructures recognized in the experimental studies of Hirth and Tullis (1992) have also been identified in natural settings (Dunlap et al., 1997; Stipp et al.,

2002a; 2010a). Extrapolation of the experimentally derived differential stress, temperature, and strain rate conditions under which these microstructures formed to natural settings allows for the use of dynamically recrystallized grain size (D) to estimate the differential stress (σ). Stipp et al. (2006) argued that quartz recrystallization microstructures will only change regimes with changes in flow stress and that there is no independent effect of hydrolytic weakening, temperature, strain rate, and quartz alpha-beta transition on grain size and hence the experimentally calibrated Stipp and Tullis (2003) piezometer.

The relationship between dynamically recrystallized grain size (D) and differential stress (σ) is shown by the equation:

$$\sigma = \mathrm{B}D^{-x} \tag{2.1}$$

where (σ) is the differential stress, (*D*) is the grain size diameter, and *B* and *x* are empirically-derived constants whose values vary between different experimental and theoretical studies. In this study we will estimate and compare differential stresses associated with deformation of Harkless quartzite samples in the contact aureole of the Papoose Flat pluton using the following three piezometers: Stipp and Tullis (2003), Twiss (1977) and Shimizu (2008).

The experimentally derived piezometer of Stipp and Tullis (2003) was calibrated using a molten salt cell Griggs apparatus to deform Black Hills quartzite under varying temperature and strain rate conditions. Holyoke and Kronenberg (2010) published an improved calibration for the Stipp and Tullis (2003) piezometer by incorporating corrections made from their experimental gas apparatus, into the differential stress equation. The piezometer is calibrated for grain sizes between ~3 and 46 μm (Stipp and Tullis, 2003). However, Stipp et al., (2010) suggest that the piezometer can be applied to grain sizes <120 μm based on correlations between microstructures recognized in experimental and natural settings. The empirical constants *B* and *x* used for calculating the differential stress with this piezometer are 480 and 0.79, respectively.

The theory-based piezometer of Twiss (1977) piezometer is temperature independent and therefore, recrystallized grain size is dependent only on differential stress. This piezometer was used by Stipp et al. (2010) to determine differential stresses for naturally deformed quartzites based on recrystallized grain sizes compiled from a number of natural case studies. They argued that given the geologic parameters for their compiled data, the Twiss (1977) piezometer is the most suitable of the currently available grain size/stress calibrations and is best-suited for GBM microstructures (Stipp et al., 2010). Gleason and Tullis (1995) and Hirth et al. (2001) also found the Twiss (1977) piezometer to be the most accurate piezometer for quartz grains recrystallized by GBM. This theoretical piezometer follows the form of Eq. 2.1. with; *B* equal to 603 and *x* equal to 0.68.

In the theoretical piezometer of Shimizu (2008) it is assumed that grain size is dependent on both stress and temperature, and that if temperature is neglected as a contributing factor, estimated stresses will be too low. This piezometer was used Boutonnet (2013) because it is best suited for SGR-GBM recrystallization microstructures, and they argued that the Twiss (1977) piezometer is applicable to subgrain size, but not to grains recrystallized by GBM. For alpha-quartz (stable at <~570 °C), the following equation (with temperature incorporated) is used for paleostress estimates on dynamically recrystallized SGR-GBM microstructures:

$$\sigma = B \times D^{-x} \times e^{\left(\frac{1190}{T}\right)} \tag{2.2}$$

where (σ) is differential stress, (*D*) is grain size diameter, *T* is temperature in K˚, *B* is an empirical constant equal to 217, and *x* is an empirical constant equal to 0.8.

Differential stress estimates for wall rocks strains associated with emplacement of the Papoose Flat pluton range from ~ 10 to 42 MPa using the Stipp and Tullis (2003) piezometer, ~ 21 to 73 MPa using the Twiss (1977) piezometer and ~ 17 to 77 MPa using the Shimizu (2008) piezometer. Only grains less than ~120 µm were considered in these differential stress estimates (based on recommendations of Stipp et al., 2010). Table 2.1 and Figure 2.16 summarize the variation in estimated stresses between the piezometers.

Table 2.1. ***Recrystallized grain size and differential stress estimates***

Sample #	Deformation Temperature (˚C)	Distance from pluton (m)	Recrystallized Grain Size Diameter (μm)	Std Dev (+/-)	Stipp, 2003 Min. (MPa)	Stipp, 2003 Avg. (MPa)	Stipp, 2003 Max. (MPa)	Twiss, 1977 Min. (MPa)	Twiss, 1977 Avg. (MPa)	Twiss, 1977 Max (MPa)	Shimizu, 2008 Min. (MPa)	Shimizu, 2008 Avg. (MPa)	Shimizu, 2008 Max. (MPa)
Traverse C													
PF-504	500	58.4	122.6	11.1	10.1	10.8	11.6	21.6	22.9	24.4	20.1	21.6	23.3
PF-505	500	67.3	225.1	15.3	6.3	6.7	7.0	14.5	15.2	15.9	12.6	13.3	14.1
PF-90	500	76.1	194.5	59.9	6.0	7.5	10.0	13.9	16.7	21.5	12.1	14.9	20.1
PF-89	500	83.0	184.9	30.8	6.9	7.8	9.0	15.6	17.3	19.6	13.7	15.5	17.9
PF-88	500	129.9	190.2	32.4	6.7	7.6	8.8	15.3	17.0	19.3	13.4	15.2	17.6
Location 26													
PF-109	550	-	103.7	16.2	11.0	12.3	14.1	23.3	25.7	28.8	20.0	22.5	25.7
PF-105	550	-	23.8	1.5	37.7	39.6	41.7	66.9	69.9	73.1	69.4	72.9	76.9
Traverse D													
PF-73	570	22.7	124.9	13.7	9.8	10.6	11.6	21.1	22.6	24.5	17.2	18.7	20.5
PF-74	570	32.7	102.4	9.7	11.6	12.4	13.5	24.4	25.9	27.7	20.4	21.9	23.8
PF-75	530	32.7	143.6	23.2	8.4	9.5	10.9	18.6	20.6	23.2	15.9	17.9	20.7
Traverse E													
PF-77	512	34.0	128.1	13.6	9.6	10.4	11.4	20.8	22.2	24.0	18.8	20.4	22.3
Traverse B													
PF-135	550	10.9	113.6	16.2	10.3	11.4	12.9	22.0	24.1	26.8	18.8	20.9	23.6
PF-136	550	15.8	117.2	16.6	10.1	11.2	12.6	21.6	23.6	26.2	18.3	20.4	23.1
PF-137	550	18.9	112.8	14.3	10.5	11.5	12.8	22.4	24.3	26.6	19.1	21.0	23.4
PF-138	544	19.9	151.3	25.1	8.1	9.1	10.5	17.9	19.9	22.5	14.9	16.8	19.4
PF-245	550	29.2	97.8	12.8	11.7	12.9	14.4	24.6	26.7	29.4	21.3	23.6	26.3
PF-246	550	39.6	103.2	11.9	11.3	12.4	13.6	23.9	25.8	28.0	20.7	22.6	24.9
PF-246A	550	41.5	112.4	11.1	10.7	11.5	12.5	22.8	24.3	26.1	19.5	21.1	22.9
PF-248	550	51.8	126.3	12.3	9.8	10.5	11.4	21.1	22.5	24.1	17.8	19.2	20.8
PF-247	550	56.1	140.6	17.3	8.8	9.7	10.7	19.3	20.9	22.8	16.1	17.6	19.6
PF-249	550	61.6	108.6	14.4	10.7	11.9	13.3	22.9	24.9	27.4	19.6	21.7	24.3
PF-249A	550	65.2	104.5	13.8	11.1	12.2	13.7	23.5	25.5	28.1	20.2	22.3	25.1
Location 46													
PF-170	550	-	88.9	25.5	11.4	13.9	18.2	24.0	28.5	35.9	20.8	25.4	33.3
PF-171	550	-	85.9	17.2	12.4	14.3	17.1	25.8	29.2	34.0	22.6	26.1	31.3
PF-173	550	-	117.7	17.6	10.0	11.1	12.7	21.4	23.6	26.3	18.2	20.3	23.1
PF-169	550	-	225.8	17.5	6.3	6.6	7.1	14.4	15.1	16.0	11.4	12.1	12.9

Recrystallized grain sizes and differential stress estimates for samples collected from the Harkless quartzites along the western margin of the Papoose Flat pluton. Structural distances from pluton margin are given if data were available. Deformation temperatures estimated from quartz c-axis fabrics (Law et al., 1992) and calc-dolomite thermometry (Nyman et al., 1995). For analytical method used for grain size measurements see text

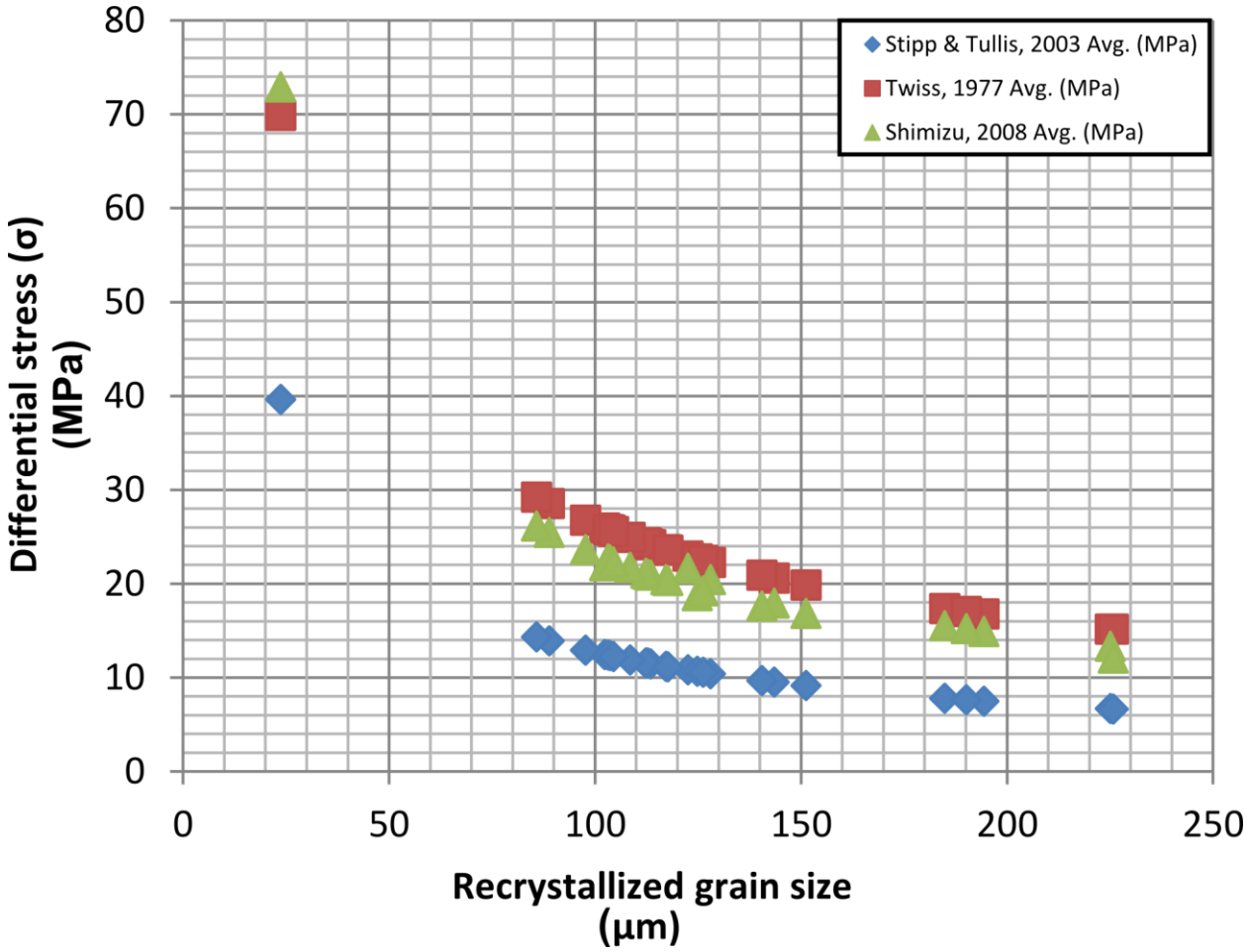

Fig. 2.16. Diagram comparing differential stress estimates for Harkless quartzites using different recrystallized grain size piezometers. All plotted values are average estimates from Table 2.1. The Stipp and Tullis (2003) piezometer gives the lowest differential stress estimates in all samples analyzed. The Twiss (1977) piezometer gives the highest differential stress estimates for all samples, except for the fine grain size sample (PF-105) that was dynamically recrystallized by SGR. For this sample, the Shimizu (2008) piezometer indicates the highest differential stress.

In this study, when comparing average differential stress estimates, the Twiss (1977) piezometer yields the highest differential stresses for all grain sizes except for sample PF-105 which has SGR microstructures and an average grain size of ~24 μm. In this case the Shimizu (2008) piezometer yields the highest differential stress estimate. When considering maximum differential stresses associated with the deformation of the Harkless quartzites, the estimate for sample PF-105 was not considered because the microstructures are interpreted to have formed post-deformation (see Section *2.3.5*). The Stipp and Tullis (2003) piezometer estimates the lowest differential stresses in all samples that were analyzed (Figure 2.16). Given the narrow extent of the aureole, estimated differential stresses do not significantly decrease traced away from the pluton margin.

2.7 Strain rate estimates

Strain rates associated with emplacement of plutons and the associated displacement of aureole rocks may occur at notably higher rates (e.g. Karlstrom et al., 1993; John and Blundy, 1993; Miller and Paterson, 1994; Nyman et al., 1995; McCaffrey et al., 1999; Fernandez and Castro, 1999; Johnson et al., 2001) than 'average' geologic strain rates of 10^{-13} to 10^{-15} s^{-1} (Pfiffner and Ramsay, 1982). As noted above, thermal modeling by Nyman et al. (1995) estimated strain rates of 10^{-12} s^{-1} for the aureole of the Papoose Flat pluton that are 1-3 orders of magnitude faster than these 'average' geologic rates. Strain rates of this magnitude are too rapid to be calculated from isotope-based geochronological techniques, but aureole rock microstructures may record these high strain rates (Gerbi et al., 2004). If steady state dislocation creep is reached in the aureole rocks, the resultant microstructure can be coupled with published wet quartzite flow laws to estimate strain rates associated with pluton emplacement and deformation of aureole rocks. The GBM quartz microstructures observed around the western margin of the pluton indicate that steady-state dislocation creep was reached in the aureole rocks.

Published wet quartzite flow laws can be used to estimate strain rate if differential stress, temperature, and water fugacity can be constrained (Hirth et al., 2001; Rutter and Brodie, 2004). The wet quartzite power law equation for strain rate follows the form:

$$\dot{e} = A f_{H_2O}^{m} \sigma^{n} \exp(-Q/RT) \quad (2.3)$$

where ė is the strain rate, *A* is a material constant, (f_{H_2O}) is the water fugacity exponent, (σ) is the differential stress, *n* is the differential stress exponent, *Q* is the activation energy, *R* is the ideal gas constant, and *T* is the absolute temperature.

The wet quartzite flow law of Hirth et al. (2001) uses comparisons between experimentally and naturally deformed rocks to constrain individual flow law parameters. The parameter values for the Hirth et al. (2001) power flow law are as follows: $A=10^{-11.2}$ MPa^{-n}/s, *m*=1, *n*=4, *Q*= 135 kJ/mol, and *R* . Water fugacity was calculated following the methodology of Hirth et al. (2001) and estimated to be ~196 MPa. This value was calculated by assuming an average deformation temperature of 550˚ C (Law et al., 1992; Nyman et al., 1995) and a maximum lithostatic pressure of 4.2 kbar (based on the presence of andalusite).

The quartzite power flow law of Rutter and Brodie (2004) was calibrated experimentally in the beta-quartz field using an argon gas medium apparatus. The parameter values for the Rutter and Brodie (2004) equation are as follows: $A=10^{-4.93}$ MPa^{-n}/s, *m*=1, *n*=2.97, and *Q*= -242000. A water fugacity of ~196 MPa was estimated in the same manner as previously noted.

These two published quartzite flow laws indicate strain rates that vary by orders of magnitude when the input parameters , temperature (*T*), and stress (σ) are kept constant. Strain rates based on the Hirth et al. (2001) flow law are typically 2-3 orders of magnitude faster than strain rates based on the Rutter and Brodie (2004) flow law (Law et al., 2011; Francsis, 2012; Law et al., 2013). For this study, the wet quartzite flow law of Hirth et al. (2001) is preferred because the parameters were determined from a well-constrained, natural tectonic setting, while the Rutter and Brodie (2004) calibration tends to indicate strain rates lower than the time-averaged strain rate (~ 10^{-12} sec^{-1}) indicated for the aureole of the Papoose Flat pluton

aureole by thermal modeling (Nyman et al., 1995). Summaries of variations in strain rate estimates for the Harkless quartzites indicated by the Hirth and Tullis (2001) and Rutter and Brodie (2004) flow laws, and using stress data from the Stipp and Tullis (2003), Twiss (1977) and Shimizu (2008) piezometers, are shown in Tables 2.2, 2.3 and 2.4, respectively All parameters except stress (σ), which varies with the piezometer chosen, are kept constant in these strain rate calculations for each sample.

Using the Hirth et al. (2001) flow law combined with the Stipp et al. (2003) piezometer results in estimated strain rates that vary between 9.7×10^{-12} and 2.9×10^{-14} s^{-1}. The Rutter and Brodie (2004) piezometer results in strain rates of 6.2×10^{-14} to 9.2×10^{-17} s^{-1} using the same input parameters (Figure 2.17).

Using the Hirth et al. (2001) flow law combined with the Twiss (1977) piezometer results in estimated strain rates that vary between 9.1×10^{-11} and 1.9×10^{-13} s^{-1}. The Rutter and Brodie (2004) piezometer results in strain rates of 3.3×10^{-13} to 9.0×10^{-16} s^{-1} using the same input parameters (Figure 2.18).

Using the Hirth et al. (2001) flow law combined with the Shimizu (2008) piezometer results in estimated strain rates that vary between 1.1×10^{-10} and 1.5×10^{-13} s^{-1}. The Rutter and Brodie (2004) piezometer results in strain rates of 3.8×10^{-14} to 7.2×10^{-17} s^{-1} using the same input parameters (Figure 2.19).

The ‘L’ shaped pattern of data points observed in Figures 2.17, 2.18, and 2.19 may be caused by the influence of deformation temperature on the strain rate equation. We would expect a decrease in differential stress to result in a decrease in strain rate. However, if estimated deformation temperatures are higher in samples with lower estimated differential stresses, this might result in an increase in estimated strain rate. When deformation temperatures are consistent between the samples, a linear relationship between differential stress and strain rate is indicated by the upper segment of the ‘L’ pattern, where an increase in differential stress results in faster strain rate estimates.

Table 2.2. *Strain rate estimates for the Stipp and Tullis (2003) piezometer*

	Stress (σ)					Strain Rate (*é*)					
Sample	Deformation Temperature (˚C)	Water Fugacity (MPa)	Stipp, 2003 Min. (MPa)	Stipp, 2003 Avg. (MPa)	Stipp, 2003 Max. (MPa)	*é* Min. (Hirth, 2001)	*é* Average (Hirth, 2001)	*é* Max (Hirth, 2001)	*é* Min (Rutter, 2004)	*é* Avg (Rutter, 2004)	*é* Max (Rutter, 2004)
Traverse C											
PF-504	500	187	10.1	10.8	11.6	9.1E-15	1.2E-14	1.6E-14	9.2E-17	1.1E-16	1.4E-16
PF-505	500	187	6.3	6.7	7.0	1.4E-15	1.7E-15	2.2E-15	2.3E-17	2.7E-17	3.2E-17
PF-90	500	187	6.0	7.5	10.0	1.2E-15	2.8E-15	8.9E-15	2.0E-17	3.8E-17	9.1E-17
PF-89	500	187	6.9	7.8	9.0	2.0E-15	3.3E-15	5.8E-15	3.0E-17	4.3E-17	6.6E-17
PF-88	500	187	6.7	7.6	8.8	1.8E-15	3.0E-15	5.4E-15	2.8E-17	4.0E-17	6.3E-17
Location 26											
PF-109	550	187	11.0	12.3	14.1	4.6E-14	7.3E-14	1.3E-13	1.2E-15	1.7E-15	2.5E-15
PF-105	550	187	37.7	39.6	41.7	6.4E-12	7.8E-12	9.7E-12	4.6E-14	5.3E-14	6.2E-14
Traverse D											
PF-73	570	187	9.8	10.6	11.6	4.6E-14	6.5E-14	9.3E-14	1.9E-15	2.5E-15	3.3E-15
PF-74	570	187	11.6	12.4	13.5	9.1E-14	1.2E-13	1.7E-13	3.2E-15	4.0E-15	5.0E-15
PF-75	530	187	8.4	9.5	10.9	9.9E-15	1.6E-14	2.8E-14	2.2E-16	3.2E-16	4.8E-16
Traverse E											
PF-77	512	187	9.6	10.4	11.4	1.0E-14	1.4E-14	2.1E-14	1.4E-16	1.8E-16	2.4E-16
Traverse B											
PF-135	550	187	10.3	11.4	12.9	3.6E-14	5.5E-14	8.9E-14	9.8E-16	1.3E-15	1.9E-15
PF-136	550	187	10.1	11.2	12.6	3.3E-14	5.0E-14	8.0E-14	9.1E-16	1.2E-15	1.8E-15
PF-137	550	187	10.5	11.5	12.8	3.8E-14	5.6E-14	8.6E-14	1.0E-15	1.4E-15	1.9E-15
PF-138	544	187	8.1	9.1	10.5	1.2E-14	1.9E-14	3.4E-14	3.7E-16	5.2E-16	8.0E-16
PF-245	550	187	11.7	12.9	14.4	6.0E-14	8.8E-14	1.4E-13	1.4E-15	1.9E-15	2.6E-15
PF-246	550	187	11.3	12.4	13.6	5.2E-14	7.4E-14	1.1E-13	1.3E-15	1.7E-15	2.2E-15
PF-246A	550	187	10.7	11.5	12.5	4.2E-14	5.7E-14	7.9E-14	1.1E-15	1.4E-15	1.8E-15
PF-248	550	187	9.8	10.5	11.4	2.9E-14	3.9E-14	5.4E-14	8.4E-16	1.0E-15	1.3E-15
PF-247	550	187	8.8	9.7	10.7	1.9E-14	2.8E-14	4.2E-14	6.2E-16	8.1E-16	1.1E-15
PF-249	550	187	10.7	11.9	13.3	4.3E-14	6.3E-14	9.9E-14	1.1E-15	1.5E-15	2.1E-15
PF-249A	550	187	11.1	12.2	13.7	4.8E-14	7.1E-14	1.1E-13	1.2E-15	1.6E-15	2.3E-15
Location 46											
PF-170	550	187	11.4	13.9	18.2	5.4E-14	1.2E-13	3.5E-13	1.3E-15	2.4E-15	5.3E-15
PF-171	550	187	12.4	14.3	17.1	7.4E-14	1.3E-13	2.7E-13	1.7E-15	2.6E-15	4.4E-15
PF-173	550	187	10.0	11.1	12.7	3.1E-14	4.9E-14	8.2E-14	8.9E-16	1.2E-15	1.8E-15
PF-169	550	187	6.3	6.6	7.1	4.9E-15	6.2E-15	8.0E-15	2.2E-16	2.6E-16	3.2E-16

Estimated strain rates for the Harkless quartzites using the Hirth et al. (2001) and Rutter and Brodie (2004) quartzite flow laws, inputting differential stress estimates from the Stipp and Tullis (2003) piezometer with corrections published by Holyoke and Kronenberg (2010).

Table 2.3. *Strain rate estimates for the Twiss (1977) piezometer*

		Stress (σ)				Strain Rate (*ė*)					
Sample	Deformation Temperature (˚C)	Water Fugacity (MPa)	Twiss, 1977 Min. (MPa)	Twiss, 1977 Avg. (MPa)	Twiss, 1977 Max. (MPa)	*ė* Min. (Hirth, 2001)	*ė* Average (Hirth, 2001)	*ė* Max (Hirth, 2001)	*ė* Min (Rutter, 2004)	*ė* Avg (Rutter, 2004)	*ė* Max (Rutter, 2004)
Traverse C											
PF-504	500	187	21.6	22.9	24.4	1.9E-13	2.5E-13	3.2E-13	9.0E-16	1.1E-15	1.3E-15
PF-505	500	187	14.5	15.2	15.9	3.9E-14	4.7E-14	5.7E-14	2.7E-16	3.1E-16	3.6E-16
PF-90	500	187	13.9	16.7	21.5	3.4E-14	7.0E-14	1.9E-13	2.4E-16	4.2E-16	8.8E-16
PF-89	500	187	15.6	17.3	19.6	5.3E-14	8.0E-14	1.3E-13	3.4E-16	4.7E-16	6.7E-16
PF-88	500	187	15.3	17.0	19.3	4.8E-14	7.4E-14	1.2E-13	3.2E-16	4.4E-16	6.4E-16
Location 26											
PF-109	550	187	23.3	25.7	28.8	9.3E-13	1.4E-12	2.2E-12	1.1E-14	1.5E-14	2.1E-14
PF-105	550	187	66.9	69.9	73.1	6.4E-11	7.6E-11	9.1E-11	2.5E-13	2.9E-13	3.3E-13
Traverse D											
PF-73	570	187	21.1	22.6	24.5	1.0E-12	1.3E-12	1.8E-12	1.9E-14	2.3E-14	3.0E-14
PF-74	570	187	24.4	25.9	27.7	1.8E-12	2.3E-12	3.0E-12	2.9E-14	3.5E-14	4.3E-14
PF-75	530	187	18.6	20.6	23.2	2.3E-13	3.5E-13	5.6E-13	2.3E-15	3.2E-15	4.5E-15
Traverse E											
PF-77	512	187	20.8	22.2	24.0	2.3E-13	3.0E-13	4.1E-13	1.4E-15	1.7E-15	2.2E-15
Traverse B											
PF-135	550	187	22.0	24.1	26.8	7.5E-13	1.1E-12	1.6E-12	9.4E-15	1.2E-14	1.7E-14
PF-136	550	187	21.6	23.6	26.2	6.9E-13	9.9E-13	1.5E-12	8.8E-15	1.2E-14	1.6E-14
PF-137	550	187	22.4	24.3	26.6	8.0E-13	1.1E-12	1.6E-12	9.8E-15	1.2E-14	1.6E-14
PF-138	544	187	17.9	19.9	22.5	2.8E-13	4.3E-13	7.0E-13	3.9E-15	5.3E-15	7.6E-15
PF-245	550	187	24.6	26.7	29.4	1.2E-12	1.6E-12	2.4E-12	1.3E-14	1.7E-14	2.2E-14
PF-246	550	187	23.9	25.8	28.0	1.0E-12	1.4E-12	2.0E-12	1.2E-14	1.5E-14	1.9E-14
PF-246A	550	187	22.8	24.3	26.1	8.6E-13	1.1E-12	1.5E-12	1.0E-14	1.3E-14	1.5E-14
PF-248	550	187	21.1	22.5	24.1	6.3E-13	8.1E-13	1.1E-12	8.2E-15	9.9E-15	1.2E-14
PF-247	550	187	19.3	20.9	22.8	4.4E-13	6.1E-13	8.7E-13	6.3E-15	8.0E-15	1.0E-14
PF-249	550	187	22.9	24.9	27.4	8.7E-13	1.2E-12	1.8E-12	1.0E-14	1.3E-14	1.8E-14
PF-249A	550	187	23.5	25.5	28.1	9.7E-13	1.4E-12	2.0E-12	1.1E-14	1.5E-14	1.9E-14
Location 46											
PF-170	550	187	24.0	28.5	35.9	1.1E-12	2.1E-12	5.3E-12	1.2E-14	2.0E-14	4.0E-14
PF-171	550	187	25.8	29.2	34.0	1.4E-12	2.3E-12	4.3E-12	1.5E-14	2.2E-14	3.4E-14
PF-173	550	187	21.4	23.6	26.3	6.7E-13	9.8E-13	1.5E-12	8.6E-15	1.1E-14	1.6E-14
PF-169	550	187	14.4	15.1	16.0	1.4E-13	1.7E-13	2.1E-13	2.6E-15	3.1E-15	3.6E-15

Estimated strain rates for the Harkless quartzites using the Hirth et al. (2001) and Rutter and Brodie (2004) quartzite flow laws, inputting differential stress estimates from the Twiss (1977) piezometer.

Table 2.4. *Strain rate estimates for the Shimizu (2008) piezometer*

		Stress (σ)				Strain Rate (*ė*)					
Sample	Deformation Temperature (˚C)	Water Fugacity MPa	Shimizu, 2008 Min. (MPa)	Shimizu, 2008 Avg. (MPa)	Shimizu, 2008 Max. (MPa)	*ė* Min. (Hirth, 2001)	*ė* Average (Hirth, 2001)	*ė* Max (Hirth, 2001)	*ė* Min (Rutter, 2004)	*ė* Avg (Rutter, 2004)	*ė* Max (Rutter, 2004)
Traverse C											
PF-504	500	187	20.1	21.6	23.3	1.5E-13	1.9E-13	2.6E-13	7.2E-16	8.9E-16	1.1E-15
PF-505	500	187	12.6	13.3	14.1	2.2E-14	2.8E-14	3.5E-14	1.8E-16	2.1E-16	2.5E-16
PF-90	500	187	12.1	14.9	20.1	1.9E-14	4.4E-14	1.5E-13	1.6E-16	3.0E-16	7.2E-16
PF-89	500	187	13.7	15.5	17.9	3.1E-14	5.1E-14	9.1E-14	2.3E-16	3.3E-16	5.1E-16
PF-88	500	187	13.4	15.2	17.6	2.9E-14	4.7E-14	8.5E-14	2.2E-16	3.2E-16	4.9E-16
Location 26											
PF-109	550	187	20.0	22.5	25.7	5.1E-13	8.2E-13	1.4E-12	7.0E-15	1.0E-14	1.5E-14
PF-105	550	187	69.4	72.9	76.9	7.4E-11	9.0E-11	1.1E-10	2.8E-13	3.3E-13	3.8E-13
Traverse D											
PF-73	570	187	17.2	18.7	20.5	4.5E-13	6.2E-13	9.0E-13	1.0E-14	1.3E-14	1.7E-14
PF-74	570	187	20.4	21.9	23.8	8.8E-13	1.2E-12	1.6E-12	1.7E-14	2.1E-14	2.7E-14
PF-75	530	187	15.9	17.9	20.7	1.2E-13	2.0E-13	3.6E-13	1.5E-15	2.1E-15	3.2E-15
Traverse E											
PF-77	512	187	18.8	20.4	22.3	1.5E-13	2.1E-13	3.0E-13	1.1E-15	1.3E-15	1.7E-15
Traverse B											
PF-135	550	187	18.8	20.9	23.6	4.0E-13	6.1E-13	9.9E-13	5.8E-15	8.0E-15	1.1E-14
PF-136	550	187	18.3	20.4	23.1	3.6E-13	5.5E-13	9.1E-13	5.4E-15	7.4E-15	1.1E-14
PF-137	550	187	19.1	21.0	23.4	4.2E-13	6.2E-13	9.6E-13	6.1E-15	8.1E-15	1.1E-14
PF-138	544	187	14.9	16.8	19.4	1.4E-13	2.2E-13	3.9E-13	2.3E-15	3.2E-15	4.9E-15
PF-245	550	187	21.3	23.6	26.3	6.6E-13	9.9E-13	1.5E-12	8.5E-15	1.1E-14	1.6E-14
PF-246	550	187	20.7	22.6	24.9	5.8E-13	8.3E-13	1.2E-12	7.8E-15	1.0E-14	1.3E-14
PF-246A	550	187	19.5	21.1	22.9	4.6E-13	6.3E-13	8.8E-13	6.5E-15	8.2E-15	1.0E-14
PF-248	550	187	17.8	19.2	20.8	3.2E-13	4.3E-13	6.0E-13	5.0E-15	6.2E-15	7.9E-15
PF-247	550	187	16.1	17.6	19.6	2.1E-13	3.1E-13	4.7E-13	3.7E-15	4.8E-15	6.6E-15
PF-249	550	187	19.6	21.7	24.3	4.7E-13	7.1E-13	1.1E-12	6.6E-15	8.9E-15	1.3E-14
PF-249A	550	187	20.2	22.3	25.1	5.3E-13	7.9E-13	1.3E-12	7.2E-15	9.7E-15	1.4E-14
Location 46											
PF-170	550	187	20.8	25.4	33.3	5.9E-13	1.3E-12	3.9E-12	7.9E-15	1.4E-14	3.2E-14
PF-171	550	187	22.6	26.1	31.3	8.3E-13	1.5E-12	3.0E-12	1.0E-14	1.6E-14	2.6E-14
PF-173	550	187	18.2	20.3	23.1	3.5E-13	5.4E-13	9.1E-13	5.3E-15	7.3E-15	1.1E-14
PF-169	550	187	11.4	12.1	12.9	5.3E-14	6.7E-14	8.7E-14	1.3E-15	1.6E-15	1.9E-15

Estimated strain rates for the Harkless quartzites using the Hirth et al. (2001) and Rutter and Brodie (2004) quartzite flow laws, inputting differential stress estimates from the Shimizu (2008) piezometer.

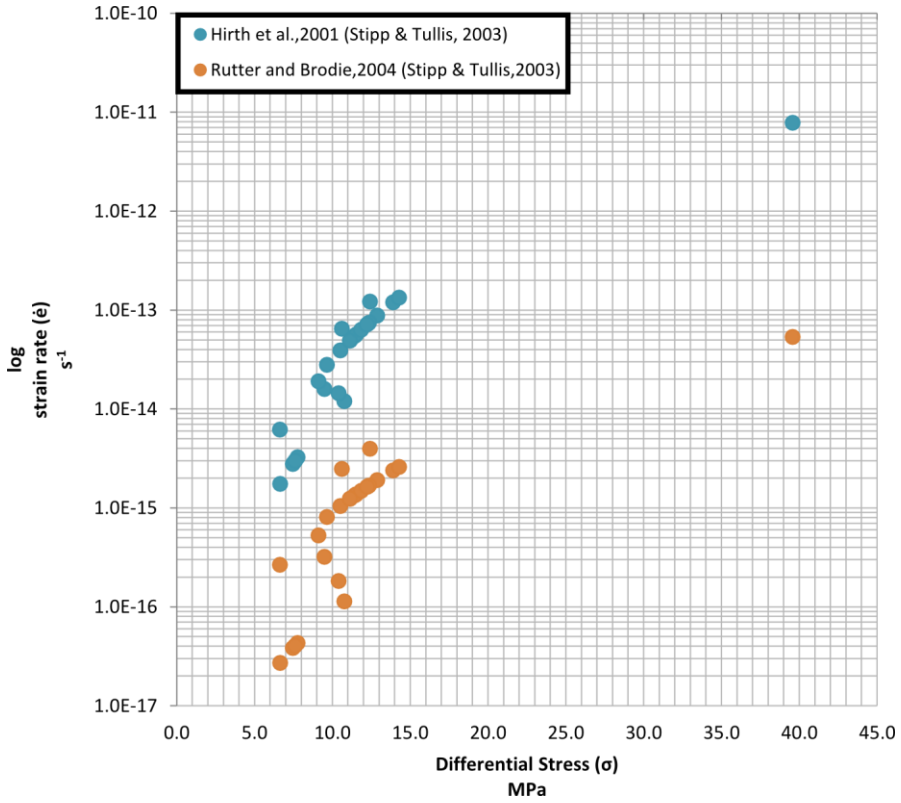

Fig. 2.17. Diagram comparing strain rate estimates from the Hirth et al. (2001) and Rutter and Brodie (2004) flow laws with differential stress estimates from the Stipp and Tullis (2003) piezometer. Temperature and differential stress are kept constant when comparing the two quartzite flow laws. Strain rate estimates vary by 2-3 orders of magnitude between the two flow laws. All plotted values are average stress and strain rate estimates from Table 2.2.

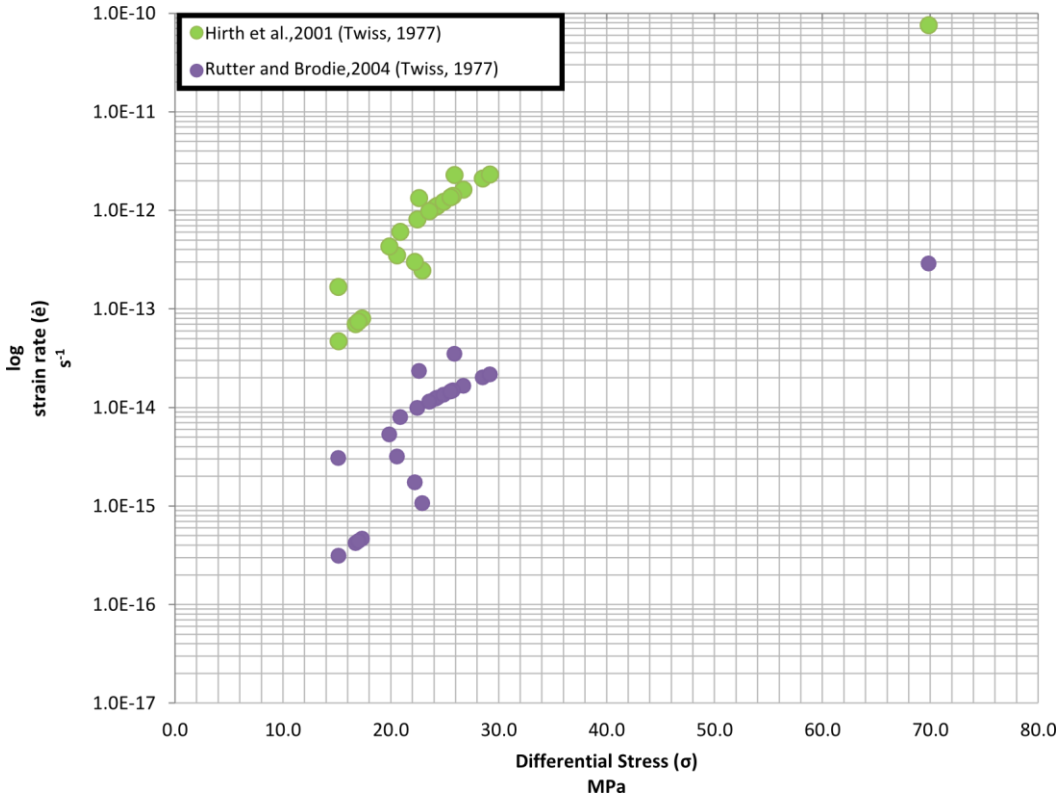

Fig. 2.18 Diagram comparing strain rate estimates from the Hirth et al. (2001) and Rutter and Brodie (2004) flow laws with differential stress estimates from the Twiss (1977) piezometer. Temperature and differential stress are kept constant when comparing the two quartzite flow laws. Strain rate estimates vary by 2-3 orders of magnitude between the two flow laws. All plotted values are average stress and strain rate estimates from Table 2.3.

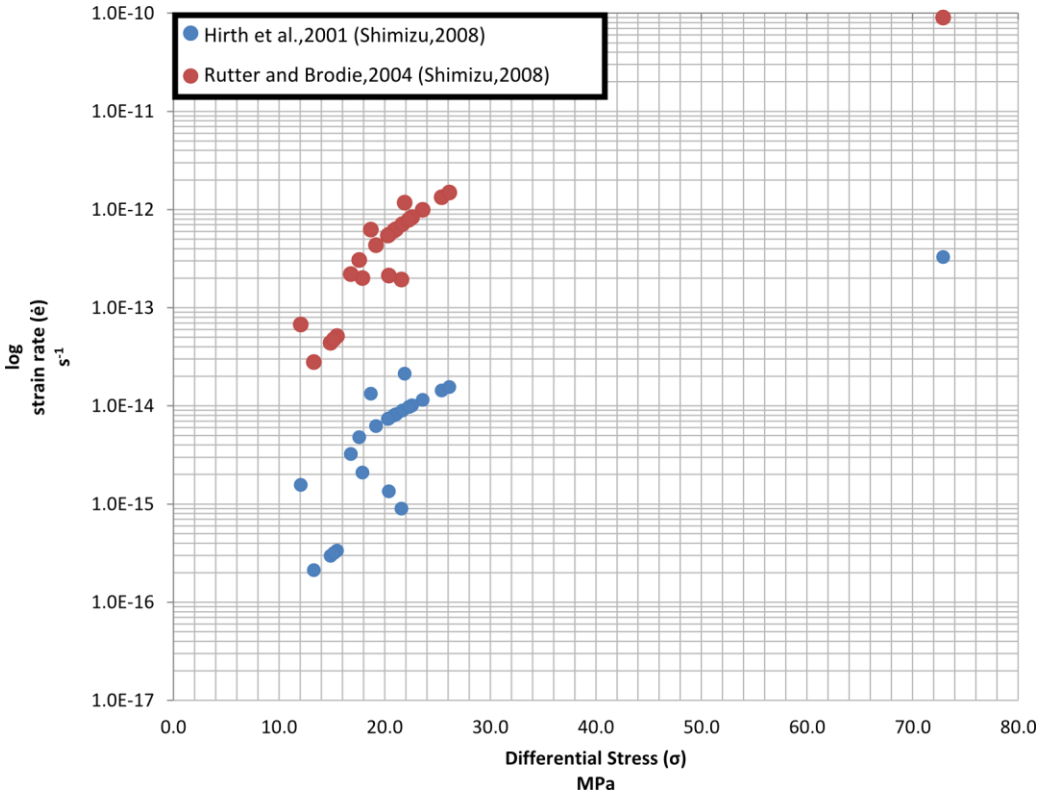

Fig. 2.19. Diagram comparing strain rate estimates from the Hirth et al. (2001) and Rutter and Brodie (2004) flow laws with differential stress estimates from the Shimizu (2008) piezometer. Temperature and differential stress are kept constant when comparing the two quartzite flow laws. Strain rate estimates vary by 2-3 orders of magnitude between the two flow laws. All plotted values are average stress and strain rate estimates from Table 2.4.

2.8 Discussion

2.8.1 Grain Boundary Area Reduction

As shown in the photomicrographs and described in Section 2.3, GBAR microstructures are most prevalent in samples close to the pluton-aureole contact, but are also noted in samples at further structural distance from the pluton margin. Grain boundary area reduction can occur during deformation and may become dominant after deformation has ended (Bons and Urai, 1992). If the GBAR microstructures in the Harkless quartzites have been formed due to post-deformation static annealing, they are interpreted to have formed as the result of elevated thermal conditions that outlasted pluton emplacement and associated wall rock deformation. In a general sense, the influence of post-deformation annealing on grain size is poorly understood and, to our knowledge, only one experimental study has addressed this issue (Helibronner and Tullis, 2002). The Heilbronner and Tullis (2002) experimental study showed that regardless of the finite dynamic recrystallization microstructure (BLG, SGR, GBM), post-deformational annealing always led to an increase in grain size. BLG showed the greatest increase in grain size with post-deformational annealing, while GBM showed the least amount of grain growth. The same increase in grain size is seen, however, in GBAR microstructures produced syn-deformation. Therefore, the ability to differentiate between recrystallized grains formed by grain boundary area reduction processes operating during (dynamic) and after (annealing) deformation is critical if we are going to apply a grain size piezometer to rocks that contain these microstructures. Inputting GBAR microstructure grain sizes into a piezometer, regardless of the process that formed them, will result in underestimates of differential flow stresses because of the relatively large grain sizes produced during these processes.

The basis for identifying GBAR microstructures in the Harkless quartzite was guided by the experimental results of Heilbronner and Tullis (2002) and the review by Passchier and Trouw (2005). Based on these criteria, grains that were clearly formed as a result of grain boundary area reduction processes were avoided when measuring grain sizes. However, it is often difficult to recognize and explicitly identify these grains as such. Lobate and inter-

fingering GBM microstructures often form at or near these triple junction boundaries, so the extent of grain boundary area reduction near these boundaries is difficult to determine. Heilbronner and Tullis (2002) proposed that for analytical purposes annealed grain sizes could be scaled down, depending on the dynamic recrystallization microstructure that was formed, prior to annealing. Based on their study, grain sizes can be scaled down by a factor of 4 to 5 for regime I/II and by a factor of 2 to 3 for regime III microstructures. While this is an appealing and apparently easy solution to the problem of grain annealing, more experimental studies will need to be conducted to test the validity of this scaling. Additionally, analytical methods for determining the grain boundary area reduction process that formed the end member microstructure must be developed.

2.8.2 Grain size piezometers

As summarized in Table 2.1 and Figure 2.16, for a given recrystallized grain size the experimental (Stipp and Tullis, 2003) and theoretical (Twiss, 1977; Shimizu, 2008) piezometers vary by a factor of two in their estimates of differential stress. This difference, especially when comparing stress estimates from the experimental and theoretical piezometers, suggests that different piezometers may be better suited for specific dynamic recrystallization mechanisms and perhaps, geologic settings. Stipp et al. (2010) proposed that the experimentally-calibrated piezometer of Stipp and Tullis (2003), which is based on BLG microstructures that vary in size between ~3 to 50 µm, may be best suited for naturally deformed samples that exhibit low temperature (and/or high strain rate) BLG to SGR microstructures. Their study shows that when applying this piezometer to grains recrystallized by GBM, it will likely underestimate the differential flow stress.

Our analysis of quartz microstructures and grain sizes in the Harkless quartzites supports this conclusion. For example, when inputting differential stress estimates obtained from the Stipp and Tullis (2003) piezometer into the Hirth et al. (2001) flow law, strain rates between 10^{-14} and 10^{-15} s^{-1} were estimated. These estimated strain rates are low, even when compared to typical geologic strain rates. As noted previously, time-averaged strain rates on the order of 10^{-}

^{12} s^{-1} are estimated for the Papoose Flat pluton aureole rocks, based on numerical cooling models (Nyman et al., 1995). This two to three order of magnitude difference in strain rate most likely results from inputting differential stress estimates that are too low for this geologic setting and GBM microstructure. This serves to demonstrate that the Stipp and Tullis (2003) quartz piezometer is not an appropriate piezometer for estimating differential stresses in high temperature naturally deformed rocks recrystallized by GBM.

Application of the Twiss (1977) theory-based piezometer to the Harkless quartzites results in higher differential stress estimates than the Stipp and Tullis (2003) piezometer. Inputting stress estimates based on the Twiss (1977) piezometer into the wet-quartzite flow law of Hirth et al. (2001) results in strain rates that are similar to those estimated by Nyman et al. (1995). Other experimental studies (Gleason and Tullis, 1993, 1995; Hirth et al., 2001) have also found that the Twiss (1977) piezometer provides differential stress estimates that are in relatively close agreement with their predetermined experimentally applied flow stresses for transitional SGR/GBM dynamically recrystallized quartz, and for quartz grains completely recrystallized by GBM. Because of these experimental findings, we favor the Twiss (1977) piezometer over the Stipp and Tullis (2003) piezometer for our study of the Harkless quartzites.

The Shimizu (2008) theory-based piezometer incorporates additional temperature condition dependencies into the analytical protocol attributing changes in grain size to both differential stress and temperature. Differential stress estimates obtained from the Harkless quartzites using this piezometer roughly correlate to stress values obtained using the Twiss (1977) piezometer. The Shimizu (2008) piezometer also appears to provide relatively robust differential stress estimates for rocks that have recrystallized by GBM; therefore we also favor this piezometer over the Stipp and Tullis (2003) piezometer.

The two-fold differences in differential stress estimates obtained using the experimentally-calibrated (Stipp and Tullis 2003) and theory-based (Twiss, 1977; Shimizu, 2008) quartz grain size piezometers (Figure 2.16) demonstrates the critical importance of applying a piezometer based on observed microstructures, especially when grains have recrystallized by

GBM. From our study of the Harkless quartzites, the Twiss (1977) and Shimizu (2008) piezometers provide differential stress estimates that are likely closest to paleo-stress conditions associated with deformation of the aureole rocks around the margin of Papoose Flat pluton based on comparisons of our values to the strain rate estimated by Nyman et al. (1995). While this is arguably the best solution currently available for choosing appropriate piezometers, more experimental work - as well as continued compilation of natural data sets - is needed in order to develop improved quartz piezometers that are calibrated for a specific dynamic recrystallization microstructure.

2.8.3 Strain Rate

As previously mentioned, contact aureole strain rates associated with pluton emplacement are typically much higher than typical 'average' geologic strain rates. Nyman et al. (1995) estimated strain rates on the order of 10^{-12} s^{-1} associated with emplacement of the Papoose Flat pluton and deformation of the surrounding aureole rocks. Strain rate modeling of aureole deformation associated with forcible pluton emplacement indicates that evidence for high strain rates is only likely to be preserved in microstructures close to the pluton-aureole rock contact (Gerbi et al., 2004; Albertz et al., 2006). As previously mentioned in Section 2.8.1, preservation of dynamic recrystallization microstructures associated with emplacement-driven deformation may be modified and/or overprinted by grain boundary area reduction microstructures during or after penetrative deformation ceases, but while the pluton and its aureole rocks are still at elevated temperatures. Other potential magma emplacement mechanisms such as stoping or assimilation can lead to loss of highly strained rocks in the inner part of the contact aureole (Paterson and Vernon, 1995). If one of these mechanisms operated during straining of the aureole rocks, the rocks preserved around a pluton margin will not necessarily record the highest strains associated with pluton emplacement. In the case of the Papoose Flat pluton, evidence for stoping or assimilation has not been found along the exposed portion of the pluton's western margin. In a more general sense, however, stoping and assimilation cannot be ruled out as possible mechanisms for removing highly strained aureole rocks.

When applying either the theoretical piezometer of Twiss (1977) or Shimizu (2008) and the quartzite flow law of Hirth et al. (2001), our strain rate estimates for the Harkless quartzites in the aureole of the Papoose Flat pluton are in general agreement (see Table 2.2,2.3,2.4 and Figure 2.17,2.18,2.19) with the time average strain rate of 10^{-12} s^{-1} estimated from thermal modeling (Nyman et al., 1995). In some samples, a strain rate up to one order of magnitude slower than this time-averaged rate is calculated. These slower strain rates may be the result of increased grain size due to GBAR processes in the quartzites. While these strain rate estimates based on grain size may be slower than the time-averaged strain rate indicated by thermal cooling models, Nyman et al., (1995) acknowledge that if multiple magma pulses were injected during evolution of Papoose Flat pluton, then strain rates in the aureole rocks will be likely be slower. Based on more recent studies of the pluton and its contact aureole by Morgan et al. (1998) and Saint Blanquat et al. (2001), it is now believed that "several" magma pulses resulted in formation of the pluton, so these slower strain rates are still likely to be in reasonable agreement with the time-averaged strain rate predictions of Nyman et al. (1995).

The Rutter and Brodie (2004) wet-quartzite flow law equation consistently estimated strain rates that are much too low when compared to typical strain rates for pluton emplacement and to the thermal cooling models of Nyman et al. (1995). Therefore, we conclude that this is not an appropriate flow law for estimating strain rates in the aureole rocks around the western margin of Papoose Flat pluton.

The problem with using quartz flow law equations to estimate strain rates is that there is not an independent way to assess strain rates in naturally deformed rocks, and thereby test the flow law-based estimates. The use of flow laws in attempting to estimate strain rates is heavily dependent on estimates of input parameters such as differential stress and deformation temperature, together with the possible impact of hydrolytic weakening on both deformation temperature thermometers and differential stress estimates. If these differential stress values are not correctly determined, then resulting strain rate estimates will also be incorrect. Therefore, when using these equations to estimate strain rate, especially in settings where quartz grains have been dynamically recrystallized by GBM, it is useful to have strain rate

models or other reference frames (e.g. Boutonnet, 2013) specific to the geologic environment, in order to determine the validity of strain rate estimates obtained from dislocation creep flow law equations. As with grain size piezometers, this is the best solution currently available and more experimental and natural datasets are required to determine a way to independently estimate strain rates.

2.8.4 Grain Size Measurements

As grain sizes increase with increasing deformation temperature and grains become more lobate and amoeboid in shape, it is often difficult to meaningfully measure grain size, given the degree of irregularity in grain shape that persists at these large sizes. The oblique transect along our linear intercept grid was implemented to take these grain boundary irregularities into account, in an attempt to mitigate errors involved with measuring these grains.

Dissection microstructures (*sensu* Urai, 1986) and island grains pose another problem when trying to estimate mean grain size. If dissection microstructures are present, the linear intercept method counts different segment of the same grain as individual dynamically recrystallized grains. This results in an average grain size that is smaller than the 'true' grain size, resulting in higher differential stress estimates when input into a grain size piezometer. The only possible way to avoid this issue is to increase the size of the data set in the hope that a close approximation to the 'true' sample average grain size, discounting island grains, is determined. Avoiding these problem island grains completely is, however, often difficult.

2.9 Conclusions

Harkless quartzites in the aureole of the Papoose Flat pluton have been dynamically recrystallized by grain boundary migration. Quartz grains from sample locations along the plastically deformed western margin of the pluton, range in size from ~ 86 to 226 µm. For paleostress analyses, samples that exhibited SGR microstructures and smaller grain sizes were excluded from the data sets used because we interpret these SGR microstructures to be related to post-deformational overprinting of the syn-deformational GBM microstructures.

Recrystallized grain size in the aureole quartzites showed no direct relationship with distance from pluton margin. This is thought to be due to rapid emplacement of the pluton resulting in a relatively narrow thermal aureole, in which all of the aureole rocks were subjected to similar deformation temperatures.

When combined with the Hirth et al. (2001) wet-quartz flow law, the theoretical piezometers of Twiss (1977) and Shimizu (2008) estimate strain rates between 10^{-12} and 10^{-13} s^{-1}. These strain rate estimates are in agreement with the thermal cooling model of Nyman et al. (1995) for deformation of the aureole rocks surrounding the western margin of the Papoose Flat pluton.

A comparison with strain rate estimates obtained by using the Stipp and Tullis (2003) piezometer and the Rutter and Brodie (2004) flow law demonstrates the need to develop a piezometer/flow combination that is specific to the dynamic recrystallization microstructure and geologic setting in which the rock was deformed. This may be accomplished through continued experimental work and by increasing the GBM data from natural settings.

References

Albertz, M., and Johnson, S. E., 2006, Modeling dislocation creep as a near-field material transfer process during spherical pluton expansion; implications for strain rates and their preservation in pluton aureoles: Journal of Structural Geology, v. 28, p. 253-267.

Bartley, J. M., Glazner, A. F., Coleman, D. S., Kylander-Clark, A., Mapes, R. W., and Friedrich, A. M., 2007, Large Laramide dextral offset across Owens Valley, California, and its possible relation to tectonic unroofing of the southern Sierra Nevada: Special Paper - Geological Society of America, v. 434, p. 129-148.

Bateman, R. 1984, On the role of diapirism in the segregation, ascent and final emplacement of granitoids: Tectonophysics, v. 110, p. 211-31

Bons, P. D., and Urai, J. L., 1992, Syndeformational grain growth; microstructures and kinetics: Journal of Structural Geology, v. 14, p. 1101-1109.

Boutonnet, E., Leloup, P. H., Sassier, C., Gardien, V., and Ricard, Y., 2013, Ductile strain rate measurements document long-term strain localization in the continental crust: Geology, v. 41, p. 819-822.

Buntebarth, G., 1984, Geothermics; An Introduction, Springer-Verlag, Berlin, 144 p.

De Bresser, J. H. P., Peach, C. J., Reijs, J. P. J., and Spiers, C. J., 1998, On dynamic recrystallization during solid state flow; effects of stress and temperature: Geophysical Research Letters, v. 25, p. 3457-3460.

Dunlap, W. J., Hirth, G., and Teyssier, C., 1997, Thermomechanical evolution of a ductile duplex: Tectonics, v. 16, p. 983-1000.

Ernst, W.G., Nelson, C.A., and Hall, C.A., 1993, Geology and metamorphic mineral assemblages of Precambrian and Cambrian rocks of the central White-Inyo Range, eastern California: California Department of Conservation, Division of Mines and Geology, Map Sheet 46, scale 1:62 500, 26 p.

Fernandez, C., and Castro, A., 1999, Pluton accommodation at high strain rates in the upper continental crust; the example of the Central Extremadura Batholith, Spain: Journal of Structural Geology, v. 21, p. 1143-1149.

Francsis, M.K., 2012, Piezometry and strain rate estimates along mid-crustal shear zones [M.S. Thesis]: Blacksburg, Virginia Polytechnic Institute and State University, 110 p.

Gerbi, C., Johnson, S. E., and Paterson, S. R., 2004, Implications of rapid, dike-fed pluton growth for host-rock strain rates and emplacement mechanisms: Journal of Structural Geology, v. 26, p. 583-594.

Glazner, A. F., and Coleman, D. S., 1994, Cretaceous crustal construction around the Owens Valley between Bishop and Independence, California: Eos, Transactions, American Geophysical Union, v. 75, Suppl., p. 583.

Gleason, G. C., and Tullis, J., 1993, Improving flow laws and piezometers for quartz and feldspar aggregates: Geophysical Research Letters, v. 20, p. 2111-2114.

Gleason, G. C., and Tullis, J., 1995, A flow law for dislocation creep of quartz aggregates determined with the molten salt cell: Tectonophysics, v. 247, p. 1-23.

Greene, D. C., and Schweickert, R. A., 1995, The Gem Lake shear zone; Cretaceous dextral transpression in the northern Ritter Range pendant, eastern Sierra Nevada, California: Tectonics, v. 14, p. 945-961.

Heilbronner, R., and Tullis, J., 2002, The effect of static annealing on microstructures and crystallographic preferred orientations of quartzites experimentally deformed in axial compression and shear. In: De Meer, S., Drury, M. R., De Bresser, J. H. P., and Pennock, G. M. (Eds.), Deformation Mechanisms, Rheology and Tectonics: Current Status and Future Perspectives. Geological Society of London, Special Publications, v. 200, p. 191-218.

Hirth, G., Teyssier, C., and Dunlap, W. J., 2001, An evaluation of quartzite flow laws based on comparisons between experimentally and naturally deformed rocks: International Journal of Earth Sciences (1999), v. 90, p. 77-87.

Hirth, G., and Tullis, J., 1992. Dislocation creep regimes in quartz aggregates. Journal of Structural Geology, v. 14, 149-159.

Holyoke, C. W., and Kronenberg, A. K., 2010, Accurate differential stress measurement using the molten salt cell and solid salt assemblies in the Griggs apparatus with applications to strength, piezometers and rheology: Tectonophysics, v. 494, p. 17-31.

Jessell, M. W., 1987, Grain-boundary migration microstructures in a naturally deformed quartzite: Journal of Structural Geology, v. 9, p. 1007-1014.

John, B.E. and Blundy, J.D., 1993, Emplacement-related deformation of granitoid magmas, southern Adamello massif, Italy: Geological Society of America Bulletin, v. 105, p. 1517-1541.

Johnson, S.E., Albertz, M., and Paterson, S.R., 2001, Growth rates of dike-fed plutons: are they compatible with observations in the middle and upper crust? Geology, v. 29, p. 727-730.

Karlstrom, K. E., Miller, C. F., Kingsbury, J. A., and Wooden, J. L., 1993, Pluton emplacement along an active ductile thrust zone, Piute Mountains, southeastern California; interaction between deformational and solidification processes: Geological Society of America Bulletin, v. 105, p. 213-230.

Kruhl, J.H. 1998, Reply: Prism- and basal-plane parallel subgrain boundaries in quartz: a microstructural geothermobarometer: Journal of Metamorphic Petrology, v. 16, p. 142–146.

Law, R.D., (in press), Deformation thermometry based on quartz c-axis fabrics and recrystallization microstructures: a review: Journal of Structural Geology.

Law, R.D., Morgan, S.S., Casey, M., Sylvester, A.G., and Nyman, M., 1992, The Papoose Flat pluton of eastern California: a re-assessment of its emplacement history in the light of new microstructural and crystallographic fabric observations: Transactions Royal Society Edinburgh: Earth Sciences, v. 83, p. 361-375.

Law, R.D., Sylvester, A.G., Nelson, C.A., Morgan, S.S., and Nyman, M., 1993, Deformation associated with emplacement of the Papoose Flat pluton, Inyo Mountains, eastern California: Geologic Overview and Fieldguide. In: Lahren, M.M., Trexler, J.H. Jr. and Spinosa, C. (eds.) *Crustal Evolution of the Great Basin and Sierra Nevada: Cordilleran - Rocky Mountain Sections, Geological Society of America Guidebook*, Department of Geological Sciences, University of Nevada, Reno, p. 231-262.

Law, R.D., Jessup, M.J., Searle, M.P., Francsis, M.K., Waters, D.J., Cottle, J.M., 2011, Telescoping of isotherms beneath the South Tibetan Detachment System, Mount Everest Massif: Journal of Structural Geology 33, 1569-1594. doi:10.1016/j.jsg.2011.09.004

Law, R.D., Stahr, D.W., Francsis, M.K., Ashley, K.T., Grasemann, B., Ahmad, T., 2013, Deformation temperatures and flow vorticities near the base of the Greater Himalayan Series, Sutlej Valley and Shimla Klippe, NW India: Journal of Structural Geology 54, 21-53. doi: 10.1016/j.jsg.2013.05.009.

Lister, G., Nicolas, A., and Poirier, J. P., 1977, Crystalline plasticity and solid state flow in metamorphic rocks [book review]: Tectonophysics, v. 43, p. 308-310.

McCaffrey, K. J. W., Miller, C. F., Karlstrom, K. E., and Simpson, C., 1999, Synmagmatic deformation patterns in the Old Woman Mountains, SE California: Journal of Structural Geology, v. 21, p. 335-349.

Miller, J. S., 1996, Pb/U crystallization age of the Papoose Flat Pluton, White-Inyo Mountains, California: Geological Society of America, Abstracts with Programs, v. 28, p. 91.

Miller, R. B., and Paterson, S. R., 1994, The transition from magmatic to high-temperature solid-state deformation; implications from the Mount Stuart Batholith, Washington: Journal of Structural Geology, v. 16, p. 853-865.

Morgan, S.S., 1992, Strain path partitioning during forceful emplacement of Papoose Flat pluton, Inyo Mountains, California [M.S. Thesis]: Blacksburg, Virginia Polytechnic Institute and State University, 126 p.

Morgan, S. S., Law, R. D., and Nyman, M. W., 1998, Laccolith-like emplacement model for the Papoose Flat Pluton based on porphyroblast-matrix analysis: Geological Society of America Bulletin, v. 110, p. 96-110.

Nelson, C. A., 1962, Lower Cambrian-Precambrian succession, White-Inyo Mountains, California: Geological Society of America Bulletin, v. 73, p. 139-144.

Nelson, C. A., Oertel, G., Christie, J. M., and Sylvester, A. G., 1978, Geologic map of Papoose Flat Pluton, Inyo Mountains, California with palinspastic map and cross sections, Geological Society of America, [Boulder, CO].

Nelson, C. A., Oertel, G., Christie, J. M., and Sylvester, A. G., 1972, Structure and emplacement history of Papoose Flat pluton, Inyo Mountains, California: Geological Society of America, Abstracts with Programs, v. 4, p. 208-209.

Nyman, M.W., Law, R.D., and Morgan, S.S., 1995, Conditions of contact metamorphism, Papoose Flat Pluton, eastern California, USA: implications for cooling and strain histories.

Journal of Metamorphic Geology, v. 13, p. 627-643.

Passchier, C. W., and Trouw, R. A. J., 2005, Microtectonics, Springer, Berlin, 366 pp.

Paterson, S. R., and Vernon, R. H., 1995, Bursting the bubble of ballooning plutons; a return to nested diapirs emplaced by multiple processes: Geological Society of America Bulletin, v. 107, p. 1356-1380.

Pfiffner, O. A., and Ramsay, J. G., 1982, Constraints on geological strain rates; arguments from finite strain states of naturally deformed rocks: Journal of Geophysical Research, v. 87, p. 311-321.

Rasband, W.S., ImageJ, U. S. National Institutes of Health, Bethesda, Maryland, USA, http://imagej.nih.gov/ij/, 1997-2014.

Ross, D.C., 1965, Geology of the Independence quadrangle, Inyo County, California: Bulletin of the United States Geological Survey, 1181-0, 64.

Ross, D.C., 1969, Descriptive petrography of three large granitic bodies in the Inyo Mountains, California. U.S. Geological Survey, Professional Paper 601, 47 p.

Rutter, E. H., and Brodie, K. H., 2004, Experimental intracrystalline plastic flow in hot-pressed synthetic quartzite prepared from Brazilian quartz crystals: Journal of Structural Geology, v. 26, p. 259-270.

Saint Blanquat, M., Tikoff, B., Teyssier, C., and Vigneresse, J.-L., 1998, Transpressional kinematics and magmatic arcs. In: Holdsworth, R.E., Strachan, R.A., Dewey, J.F., Continental transpressional and transtensional tectonics. Geological Society of London Special Publications, v. 135, p. 327-340.

Saint-Blanquat, M., Law, R. D., Bouchez, J.-L., and Morgan, S. S., 2001, Internal structure and emplacement of the Papoose Flat Pluton; an integrated structural, petrographic, and magnetic susceptibility study: Geological Society of America Bulletin, v. 113, p. 976-995.

Shimizu, I., 2008, Theories and applicability of grain size piezometers; the role of dynamic recrystallization mechanisms: Journal of Structural Geology, v. 30, p. 899-917.

Smith C.S., and Guttman L., 1953, Measurement of internal boundaries in three dimensional structures by random sectioning. Trans AIME 197: 81.

Song, W. J., and Ree, J.-H., 2007, Effect of mica on the grain size of dynamically recrystallized quartz in a quartz-muscovite mylonite: Journal of Structural Geology, v. 29, p. 1872-1881.

Stipp, M., Stünitz, H., Heilbronner, R., and Schmid, S., 2002a, Dynamic recrystallization of quartz: correlation between natural and experimental conditions. In: De Meer, S., Drury, M. R., De Bresser, J. H. P., and Pennock, G. M. (Eds.), Deformation Mechanisms, Rheology and Tectonics: Current Status and Future Perspectives. Geological Society of London, Special Publications, v. 200, p. 171–190.

Stipp, M., Stünitz, H., Heilbronner, R., and Schmid, S. M., 2002b, The eastern Tonale fault zone; a “natural laboratory” for crystal plastic deformation of quartz over a temperature range from 250 to 700 degrees C: Journal of Structural Geology, v. 24, p. 1861-1884.

Stipp, M., and Tullis, J., 2003, The recrystallized grain size piezometer for quartz. Geophysical Research Letters 2088, doi:10.1029/2003GL018444.

Stipp, M., Tullis, J., and Behrens, H., 2006, Effect of water on the dislocation creep microstructure and flow stress of quartz and implications for the recrystallized grain size piezometer: Journal of Geophysical Research, v. 111, p. 19, doi:10.1029/2005JB003852.

Stipp, M., Tullis, J., Scherwath, M., and Behrmann, J.H., 2010, A new perspective on paleopiezometry: Dynamically recrystallized grain size distributions indicate mechanism changes: Geology, v. 38, p. 759-762, doi: 10.1130/G31162.

Stoeckhert, B., and Duyster, J., 1999, Discontinuous grain growth in recrystallised vein quartz; implications for grain boundary structure, grain boundary mobility, crystallographic preferred orientation, and stress history: Journal of Structural Geology, v. 21, p. 1477-1490.

Sullivan, W. A., and Law, R. D., 2007, Deformation path partitioning within the transpressional White Mountain shear zone, California and Nevada: Journal of Structural Geology, v. 29, p. 583-599.

Sylvester, A.G., Oertel, G., Nelson, C.A., and Christie, J.M., 1978. Papoose Flat pluton: A granitic blister in the Inyo Mountains, California: Geological Society of America Bulletin, v. 89, p. 1205–1219.

Tikoff, B., and de Saint Blanquat, M., 1997, Transpressional shearing and strike-slip partitioning in the Late Cretaceous Sierra Nevada magmatic arc, California: Tectonics, v. 16, p. 442-459.

Tobisch, O. T., Saleeby, J. B., Renne, P. R., McNulty, B. A., and Tong, W., 1995, Variations in deformation fields during development of a large-volume magmatic arc, central Sierra Nevada, California: Geological Society of America Bulletin, v. 107, p. 148-166

Tullis, J., and Yund, R. A., 1982, Grain growth kinetics of quartz and calcite aggregates: Journal of Geology, v. 90, p. 301-318.

Twiss, R.J., 1977, Theory and applicability of a recrystallized grain size paleopiezometer. Pure and Applied Geophysics, v. 115, 227-244.

Urai, J.L., Means, W.D., and Lister, G.S., 1986, Dynamic recrystallization of minerals. In: Hobbs, B.E., Heard, H.C. (Eds.), Mineral and Rock Deformation: Laboratory Studies. Geophysical Monograph, v. 36, p. 161-199. American Geophysical Union, Washington DC.

Vines, J. A., 1999, Emplacement of the Santa Rita Flat Pluton and kinematic analysis of cross cutting shear zones, eastern California [M.S. Thesis]: Blacksburg, Virginia Polytechnic Institute and State University, 89 p.

CHAPTER 3

Using structure contour maps to analyze subsurface 3D fault geometry along segments of the Moine thrust zone, NW Scotland

N.D. HEAVERLO[1], R.D. LAW[1]

[1]*Department of Geosciences, Virginia Polytechnic Institute and State University, Blacksburg, Virginia, 24061, USA*

Abstract

Beginning in the late 19th century, extensive research throughout the Moine thrust zone (MTZ) in the Highlands of NW Scotland has resulted in the production of detailed geologic maps with excellent control on the location of the Moine thrust (MT). Much like other thrust belts, the MTZ displays map pattern curves (salients and recesses) that vary in amplitude and sinuosity when traced along orogenic strike. Structure contour maps constructed along these salients and recesses allow us to interpret subsurface variations in 3D geometry and lateral continuity of the thrust planes.

A structure contour map of the MT, extending from the North Coast southwards for ~100 km to the Dundonnel area, was constructed from 1:50,000 scale British Geological Survey (BGS) maps by correlating map positions of the MT between elevation control points, constrained by the intersection of the fault trace with topographic contours. The structure contour map indicates significant lateral variation in subsurface 3D geometry of the fault surface. Salients along the MT are characterized by either relatively planar geometries or broad synformal corrugations on the fault surface, recesses are associated with antiformal corrugations, and relatively linear segments of the fault are characterized by planar geometries.

A structure contour map constructed on the Glencoul thrust as depicted on original BGS maps for the Assynt region, confirms that the mapped thrust segments to the NE and SW of Loch Glencoul are part of the same structure, rather than different structures separated by a lateral ramp as the result of lateral ramp truncation as shown on more recent BGS maps.

3.1 Introduction

A structure contour map is a powerful visual tool that can be used to analyze the three dimensional geometry and lateral continuity of thrust planes (Sebring, 1958; Elliot and Johnson, 1980; Bird, 1988; Groshong, 2006). Structure contour maps constructed on regional scale faults facilitate insight into lateral and down-dip changes in 3D geometry of the fault surface and linkages with structures in the adjacent hanging wall and footwall. Lateral variations in 3D fault geometry are common in most thrust terranes and may be either original features of the fault

surface (frontal, oblique and lateral ramps etc.) or due to later deformation of the fault surface (e.g. subsequent folding over underlying imbricates associated with foreland propagating thrusts). Lateral and down-dip irregularities in the 3D shape of the fault are often linked to changes in footwall rock type, and/or basement control, including the influence of pre-existing basement faults, and syn-thrusting footwall deformation. The most pronounced variations in geometry are often associated with curves in the map traces of thrusts and associated folds, referred to as salients and recesses (Elliot and Johnson, 1980; Marshak, 2004).

Salients and recesses are map-view curves observed in thrust terranes/orogenic belts (see Thomas, 1977; Elliot and Johnson, 1980; Thomas, 1983, Marshak, 2004). A recess is a map pattern curve of an orogenic belt that is convex toward the hinterland, while a salient is concave toward the hinterland (Figure 3.1) (Billings, 1954). These map patterns are indicative of non-planar geometries, formed as the result of a number of variables, which include pre-existing basin geometry, basement obstacles, rheologic changes in footwall lithology, and continental margin irregularities that were present, prior to orogenesis (Thomas, 1983; Marshak, 2004).

A structure contour map was constructed along the Moine thrust from topographic contour control points identified on 1:50,000 scale British Geological Survey sheets, in order to characterize subsurface lateral variation in the three dimensional geometry of the Moine thrust. This structure contour map extends from the North Coast southwards for ~100 km to the Dundonnel area (Figure 3.2).The structure contour map was then used to determine structural geometries associated with map-pattern recesses, salients, and linear segments of the Moine thrust. Dip variation was calculated from structure contour spacing and compared to structural data recorded on British Geological Survey maps. The structure contour map was also used to constrain three-dimensional hanging wall geometries adjacent to the salients and recesses on the underlying Moine thrust. Previously published structure contour maps constructed by Elliott and Johnson (1980) around these mapped curves for a ~50 km long section of the Moine thrust (Assynt region), demonstrate the non-planar nature of the thrust surface. Structure contour maps created for the Assynt and Dundonnel Culminations

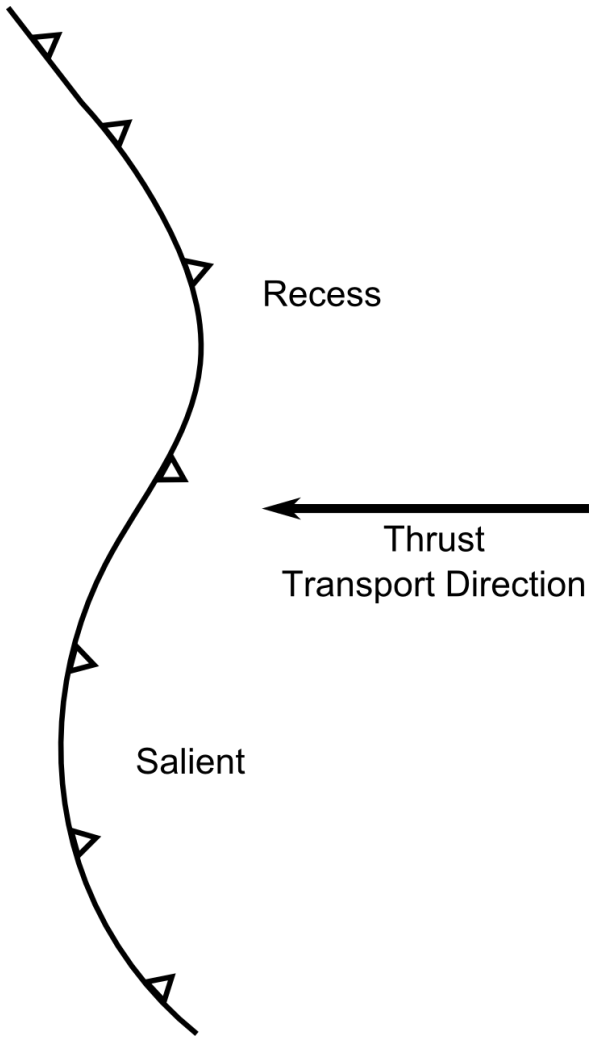

Fig 3.1. Schematic representation of salient and recess on map trace of a thrust fault. A recess is convex toward the hinterland (right hand side of diagram) while a salient is concave toward the hinterland.

(i.e. recesses) during their analysis of the structural evolution of the Moine thrust zone indicated the presence of hanging wall antiforms associated with these recesses.

A structure contour map was also constructed on the Glencoul thrust as depicted on the original Geological Survey maps for the northern part of the Assynt Culmination (Peach et al., 1907; British Geological Survey, 1923) in order to test later reinterpretation of this structure proposed by the Geological Survey (Krabbendam and Leslie, 2004; British Geological Survey, 2007).

3.2 Geologic Setting

The Highlands of NW Scotland are considered one of the type localities that guide our understanding of middle and upper crustal tectonic processes operating in orogenic belts. Extensive mapping and research in this region began in the late 19th century (see reviews by Butler, 2010a, b; Law and Johnson, 2010) with geologic maps (1:63,360) from the region first published in the late 19th century (Peach et al., 1888). Arguably, the most important work that emerged from this early research was the 1907 Geological Survey Memoir entitled; *The Geological Structure of the North-West Highlands of Scotland* (Peach et. al., 1907). This work established the structural framework for the Moine Thrust zone, outlining concepts related to the structural evolution of the NW Highlands which continue to guide research today. More recent mapping in the Moine thrust zone has been completed by the British Geological Survey and associated university-based researchers from the mid-1950s to mid-2000s was released in a series of 1:50,000 scale sheets. (British Geological Survey, 1997, 2002, 2007, 2008, 2009, 2011, 2012).

The Moine thrust zone is composed of a WNW-directed series of thrust sheets, which form the NW margin of the Caledonian orogenic belt in Scotland (Figure 3.2) (see review by Strachan, 2002). Debate has continued for over a hundred years on the relative timing of motion on the individual thrust surfaces in the thrust belt. Adoption of 'Rocky Mountains / Appalachian thrust rules' in the early 1980s led to a broad consensus that the thrust belt developed as a foreland propagating piggy-back sequence (e.g. Elliot and Johnson, 1980; Coward, 1985), but this view has more recently been questioned by Butler (2004b, 2010b).

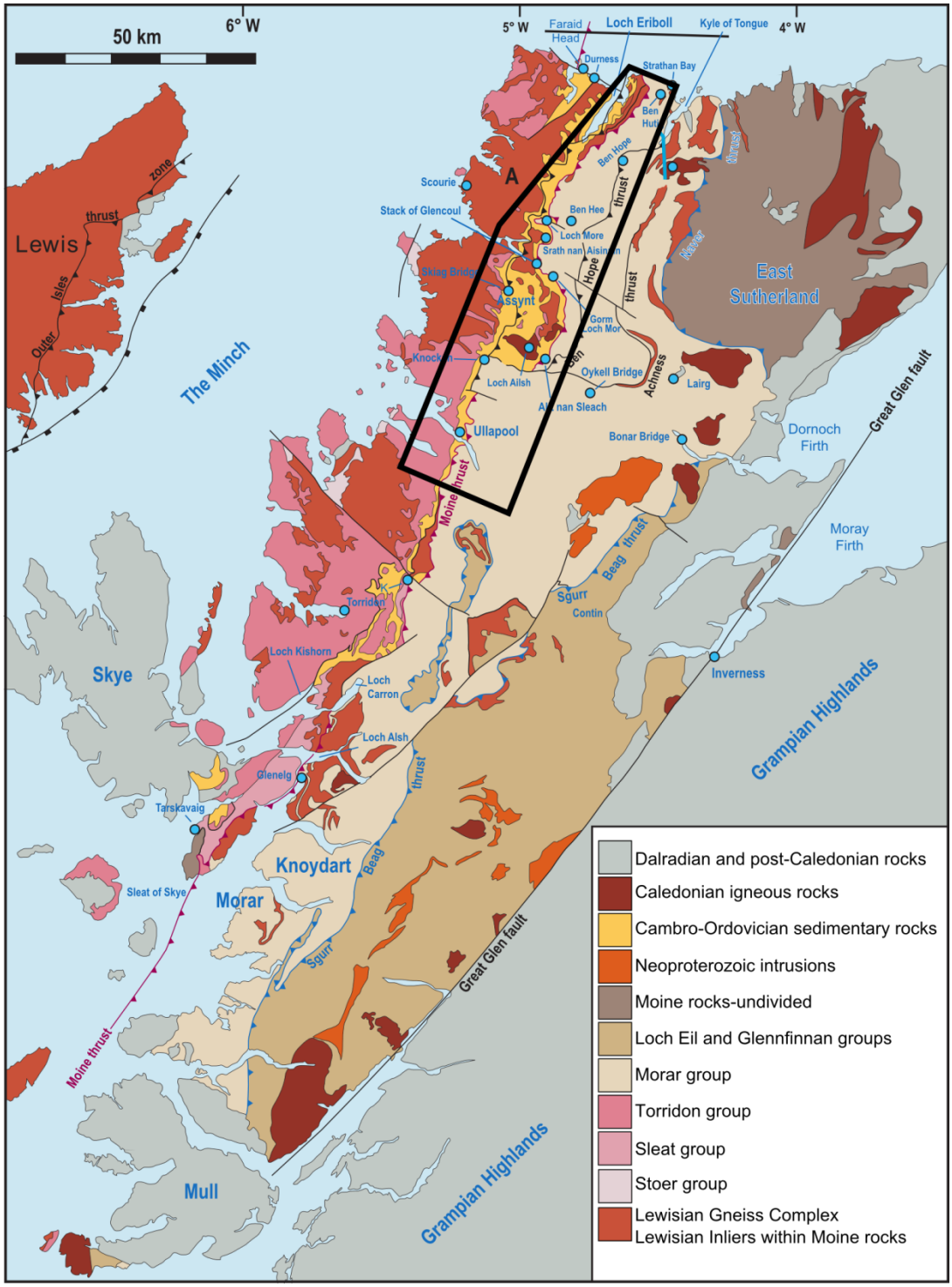

Fig. 3.2. Generalized geologic map of NW Scotland. The Moine thrust (purple) is the structurally highest fault in the Moine thrust zone and is positioned at the eastern-most margin of the thrust zone. Black box indicates study area. Figure from Thigpen et al. (2010b).

The Moine thrust zone developed during the Scandian phase (~430 Ma) of the Caledonian Orogeny, as a result of the collision of Laurentia and Baltica during closure of the Iapetus Ocean (see review by Strachan, 2002) Timing of motion on the Moine thrust zone is constrained by syntectonic magmatism and is estimated at *c.* 430-415 Ma (Kinny et al., 2003; Alsop, 2010; Goodenough et al., 2011). The Moine thrust is the eastern-most, and structurally highest thrust, while the Glencoul thrust is a structurally lower thrust exposed further to the west within the Moine thrust zone.

The Moine thrust has a mapped length of ~ 200 km, with various salients and recesses in its map-view pattern. The thrust juxtaposes Proterozoic Moine Supergroup metasedimentary rocks and their sheared Lewisian basement over Cambrian or Torridonian sedimentary rocks and their basement (Figure 3.3). First described in detail by Peach et al. (1888, 1907), foliation in the Moine thrust sheet has a gentle sheet dip to the SE, with down dip mineral stretching lineation trending perpendicular to the map trace of the underlying Moine thrust. The structural placement of the Moine thrust in relation to the various lithotectonic units recognized in the NW Highlands has at times been controversial (see review by Law and Johnson, 2010, pp. 474-475). In producing our structure contour map we have followed the general practice adopted by the Geological Survey in placing the Moine thrust at the base of the Moine Supergroup metasedimentary rocks and – where present – their underlying mylonitic Lewisian basement rocks.

In the Assynt region, stacking of thrust sheets has bulged up the overlying Moine thrust, producing the Assynt Culmination (British Geological Survey, 1923). Despite the extensive and detailed mapping of faults within the culmination, interpretation of some structures remains controversial, especially the relationships between lateral ramps and the termination of thrust sheets.

In the northern part of the Assynt Culmination, two large thrusts are present; the Glencoul thrust, located in a more foreland position, and the Ben More thrust, located in a more hinterland position to the east. Both sheets carry Lewisian gneiss, Cambrian basal quartzite and Pipe Rock (Krabbendam and Leslie, 2004). To the north of Loch Glencoul only one of these

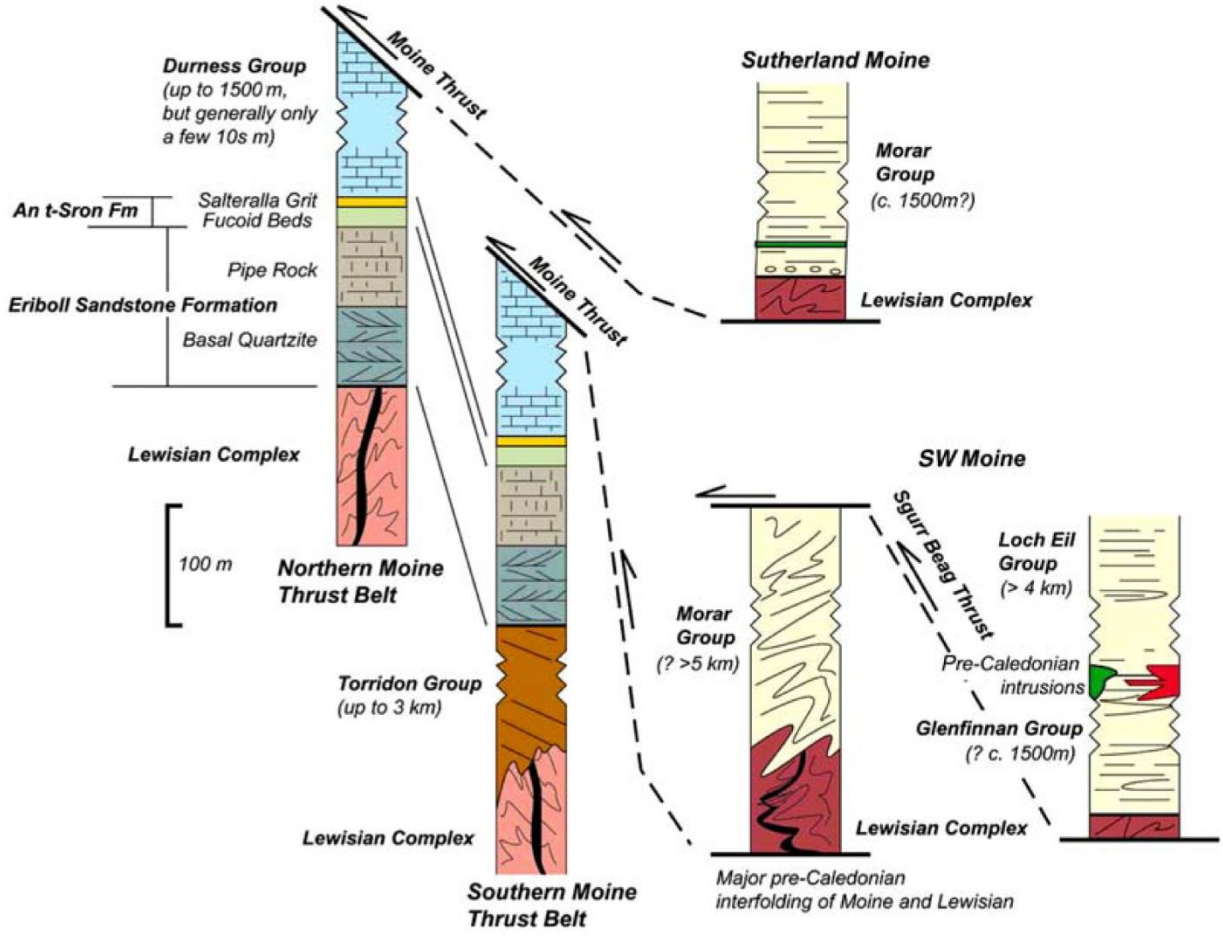

Fig. 3.3 Simplified tectonostratigraphic columns for the Moine thrust zone of NW Scotland. The Moine thrust juxtaposes Proterozoic age Moine Supergroup metasedimentary rocks and their Lewisian (Archean) basement over Cambrian or Torridonian sedimentary rocks and their basement. Figure from Butler (2010).

thrust sheets is present (Figure 3.4); therefore one thrust must terminate at or to the south of Loch Glencoul.

Since its initial recognition by Callaway (1883) , the Glencoul thrust has been mapped as continuing along strike from the SW side of Loch Glencoul to the NE across Loch Glencoul and the eastern end of Loch Glendhu, while the Ben More thrust terminates somewhere to the south. North of Na Tuadhan, the precise location for termination of the Ben More thrust has been debated (see Figure 3.4; Clough in Peach et al., 1907; Bailey, 1935; Elliot and Johnson, 1980). More recent mapping by Krabbendam and Leslie (2004) led to the conclusion that the Glencoul thrust terminates to the NE against a lateral branch line at Loch Glencoul and that the Ben More thrust continues to the north across Loch Glencoul, changing the over 100 year old structural interpretation for this part of the Assynt Culmination (Figure 3.5). This interpretation greatly reduces the size of the Glencoul thrust sheet, increases the size of the Ben More thrust sheet, and has implications for the structural propagation style in the region.

The last piece of field evidence for the Ben More thrust is located at Glen Beag, approximately 4 km to the SE of the proposed lateral truncation (Figure 3.5). The newly proposed map trace of the Ben More thrust strikes to the WNW across Glen Beag, cutting across topographic contours in this area, and implying a nearly vertical thrust fault. The Krabbendam and Leslie (2004) interpretation for the lateral truncation of the Glencoul thrust also implies that within the Assynt Culmination, the structural style is that of a hinterland propagating sequence, as opposed to the foreland propagating style for the region proposed by Elliot and Johnson (1980) (Figure 3.6). If the Glencoul thrust is in fact laterally truncated by the Ben More thrust, this implies that the Ben More thrust is a younger structure within the Assynt culmination.

3.3 Analytical Methods

Structure contours on the Moine thrust were constructed using 1:50,000 scale British Geological Survey (BGS) sheets (Figure 3.7). (British Geological Survey, 1997, 2002, 2007, 2008, 2009, 2011, 2012) Structural control points were constrained by locating intersection points between the map trace of the Moine thrust and topographic contours shown on the BGS maps.

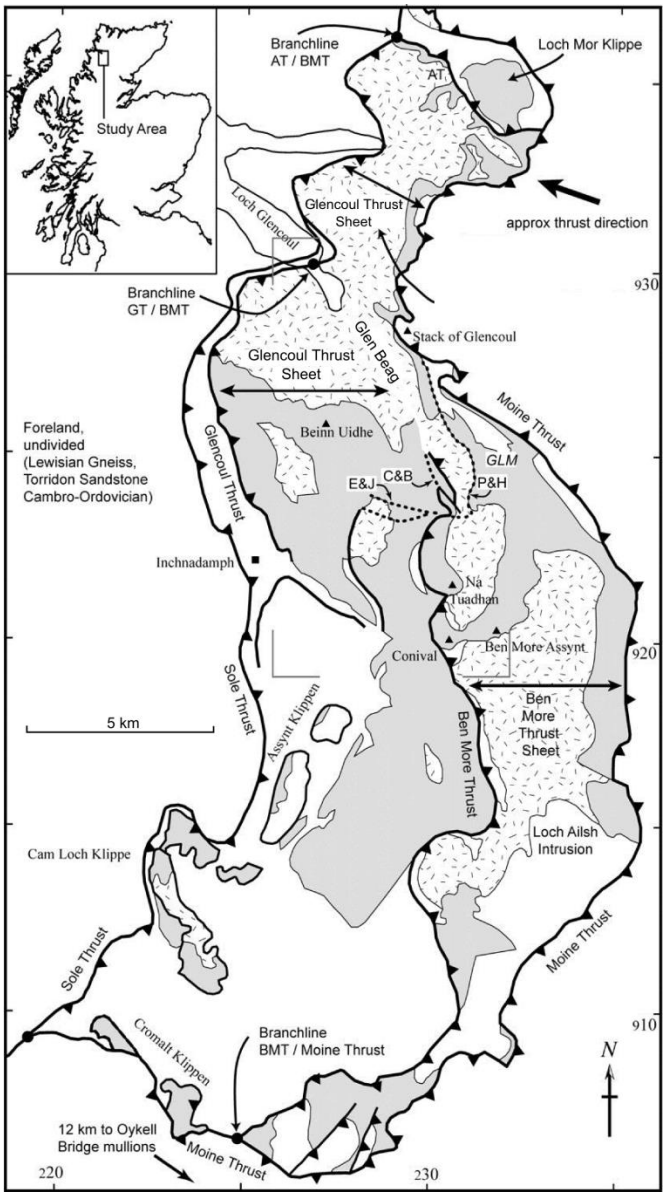

Fig. 3.4. Simplified Geologic map of the Assynt Culmination showing the relative locations of the Glencoul and Ben More thrust. The original interpretation for the location of the Glencoul thrust (Peach et al., 1907; British Geological Survey, 1923) continuing to the north across Loch Glencoul is shown. To the south of Na Tuadhan the location of the Ben More thrust is well constrained, but the location to the north is uncertain. Dashed lines for the Ben More thrust, north of Na Tuadhan are previous interpretations for its location. E & J: Elliot and Johnson (1980); C & B: Clough (in Peach et al., 1907) and Bailey (1935); P & H: Peach and Horne (1907). Figure modified from Krabbendam and Leslie (2004).

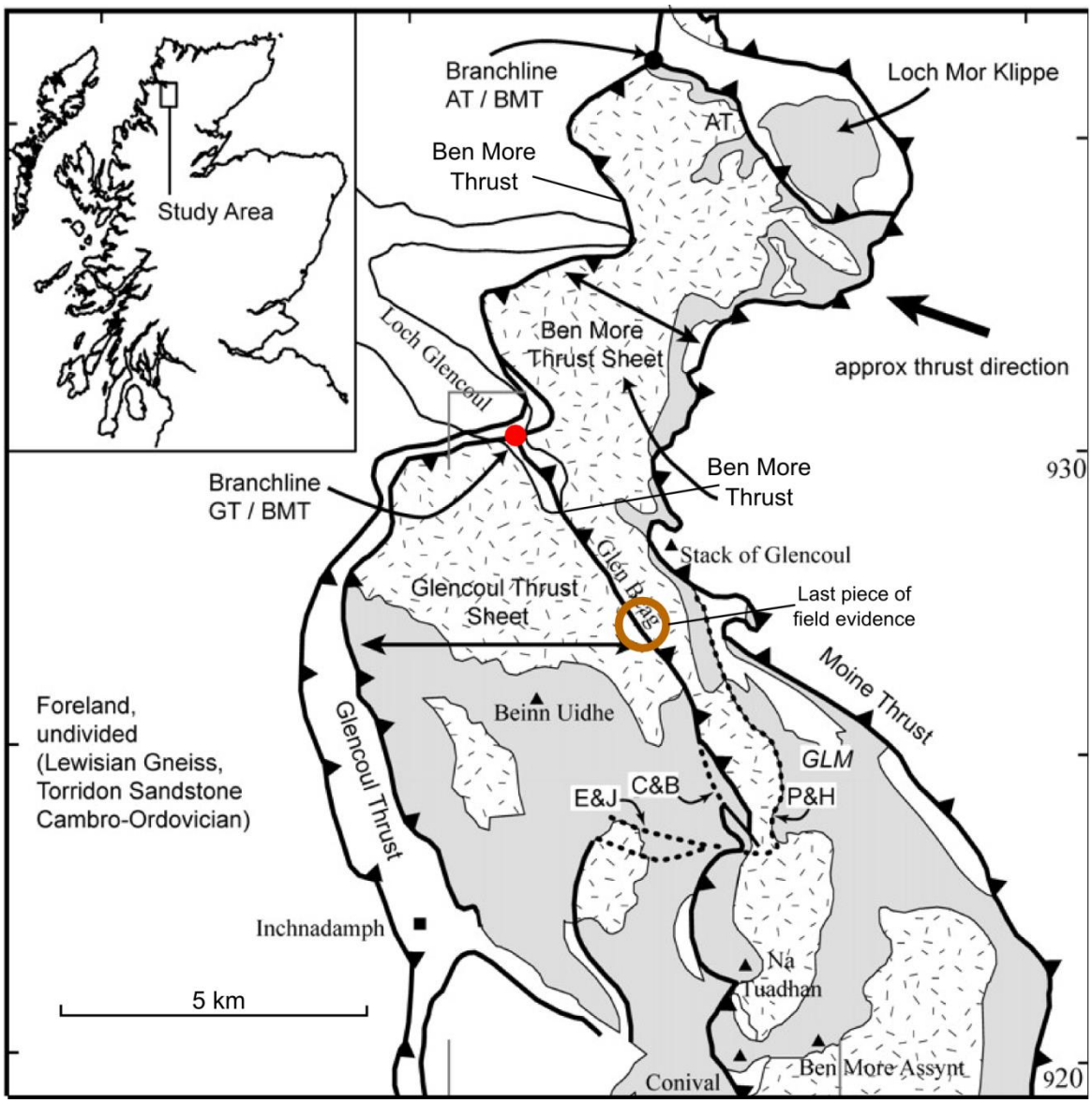

Fig 3.5. Simplified geologic map of the northern portion of the Assynt Culmination showing the Krabbendam and Leslie (2004) interpretation for termination of the Glencoul thrust south of Loch Glencoul. The red dot indicates the truncation of the Glencoul thrust at a lateral branch line, with the Ben More thrust continuing across Loch Glencoul to the north. The last piece of field evidence (interpreted to be the Ben More thrust), is indicated by the orange circle in Glen Beag. Figure modified from Krabbendam and Leslie (2004).

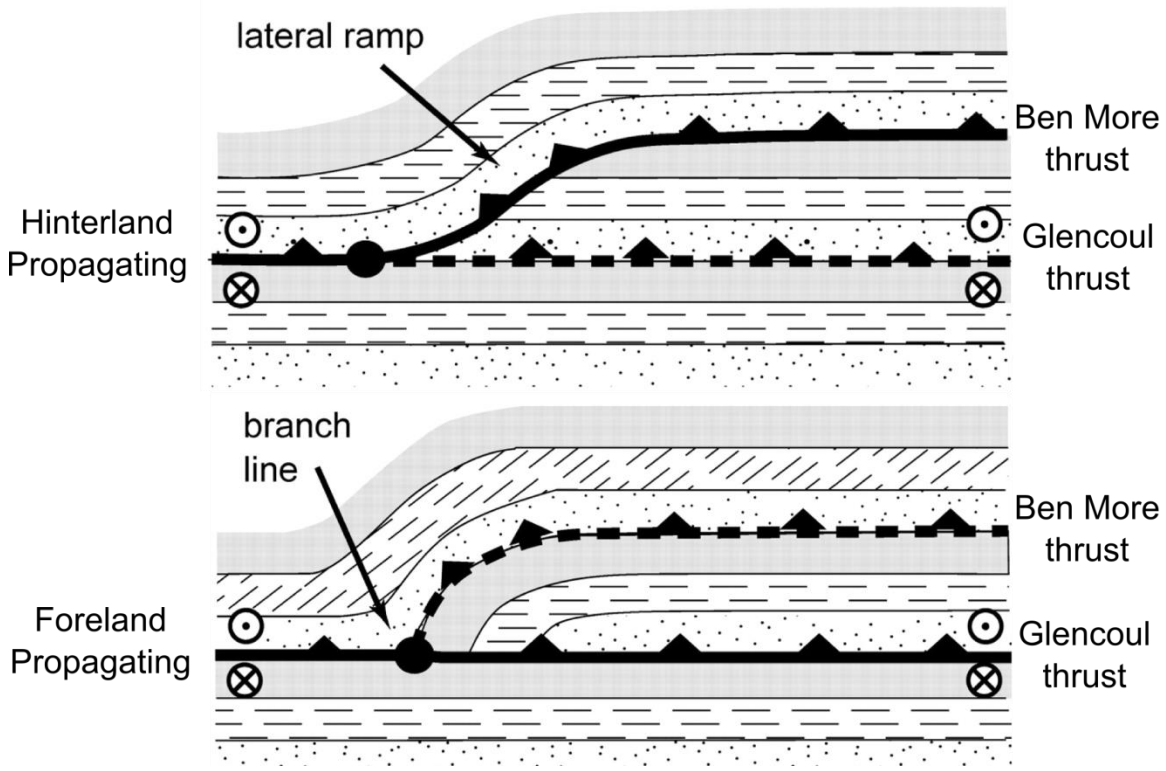

Fig. 3.6. Diagram showing the end member models for thrust propagation in the Assynt Culmination. The diagram has transport direction toward the viewer. In the top diagram, the Glencoul thrust terminates at a lateral ramp and the Ben More thrust forms out of sequence (hinterland propagating) as proposed by Krabbendam and Leslie (2004). In this interpretation the Ben More thrust is younger than the Glencoul thrust. The lower diagram is after previous interpretations (Elliot and Johnson, 1980) and displays a foreland propagating style. In this case, the younger thrust is the Glencoul thrust. Figure modified from Krabbendam and Leslie (2004).

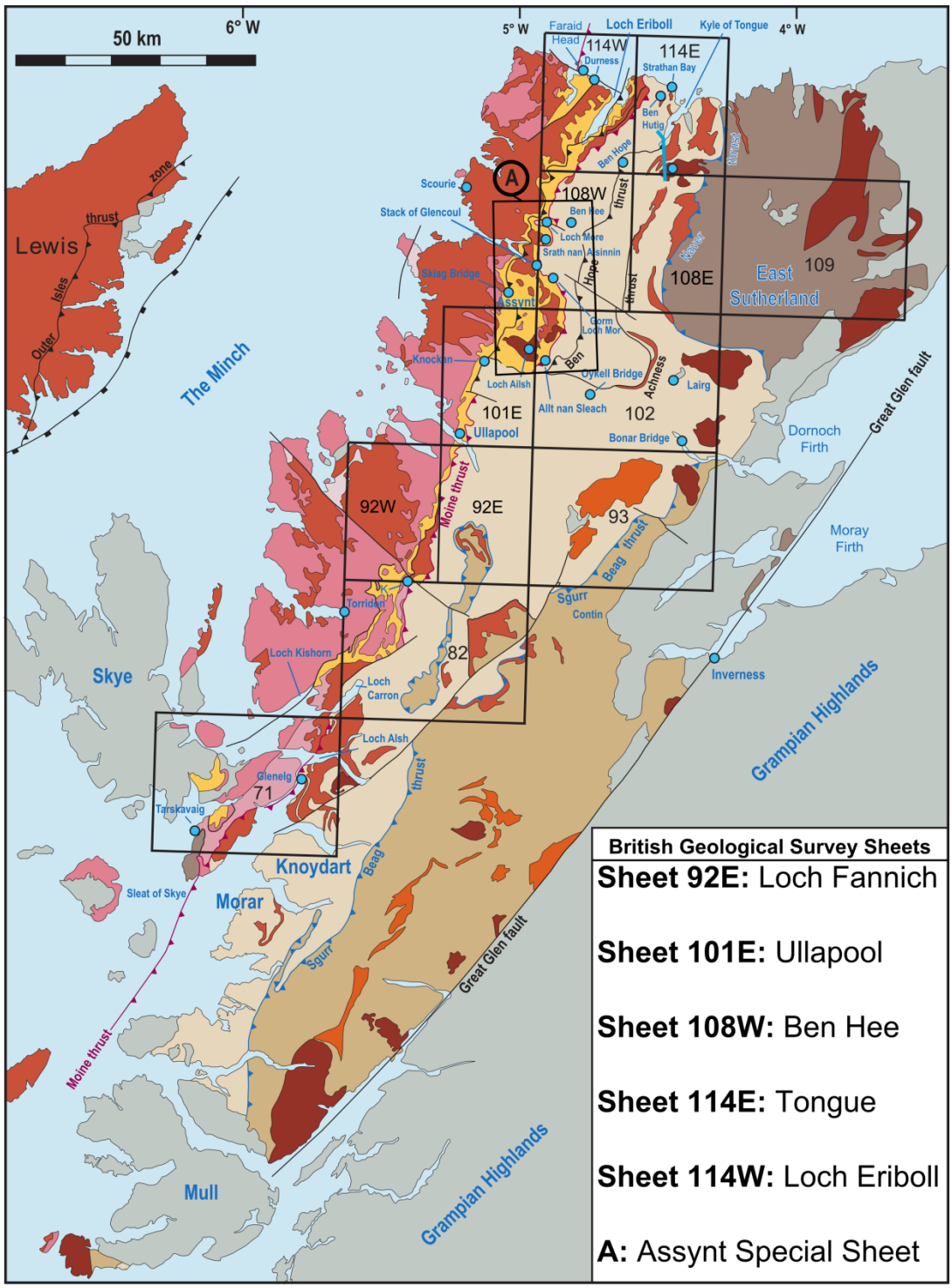

Fig. 3.7. Location map of British Geological Survey sheets (1:50 000. Inset box on the lower right includes all sheets that were used to construct our structure contour map. Figure adapted from Thigpen et al. (2010b) and Law and Johnson (2010).

Correlation between elevation control points was completed by hand contouring between equal elevation points along the trace of the fault (Figure 3.8) Contouring was completed from the North Coast (Tongue Sheet; British Geological Survey, 1997) to the Dundonnel structure located to the south of Loch Broom (Loch Fannich Sheet; British Geological Survey, 2011).

Contouring began in areas with the highest density of elevation control points and then moved laterally toward areas with sparse control. Contouring in these areas allows us to accurately characterize lateral variations in both the 3D shape of the fault surface and variations in the structural geometry of the adjacent hanging wall rocks (e.g. dip direction, folding style), and to use these well-constrained geometries to guide our interpretations in adjacent segments of the Moine thrust where structure contours cannot be drawn with such confidence. In the well-controlled areas, structure contours of differing elevation were mapped simultaneously in order to accurately determine local strike and dip values for the fault surface.

Structure contours are given as meters above sea level and presented in both 50 meter and 10 meter contour intervals. 50 meter intervals are displayed as solid lines with a specific color that reflects their elevation. Dashed 50 meter lines denote where structure contours could not be drawn with confidence and represent what is considered to be the most likely structure suggested by interpolation between well-constrained map areas. All interpretations were guided by structure contours drawn at 10 meter intervals. However, 10 meter contour intervals are only displayed if 50 meter control was not sufficient to accurately determine 3D fault geometry or dip direction. These contours are presented as thin black lines, with the elevation noted on the line.

In the hanging wall to the Moine thrust, care was taken in drawing structure contours so that individual structure contours do not intersect topographic contours that are lower in elevation, as this would imply the thrust should be exposed on the topographic surface. Similarly, individual structure contours that in map view are drawn across the footwall to the Moine thrust (west of the fault trace), are higher in elevation than the topographic contours they intersect. In these areas, the structure contours are projections of hanging wall geometry but located above the topographic surface.

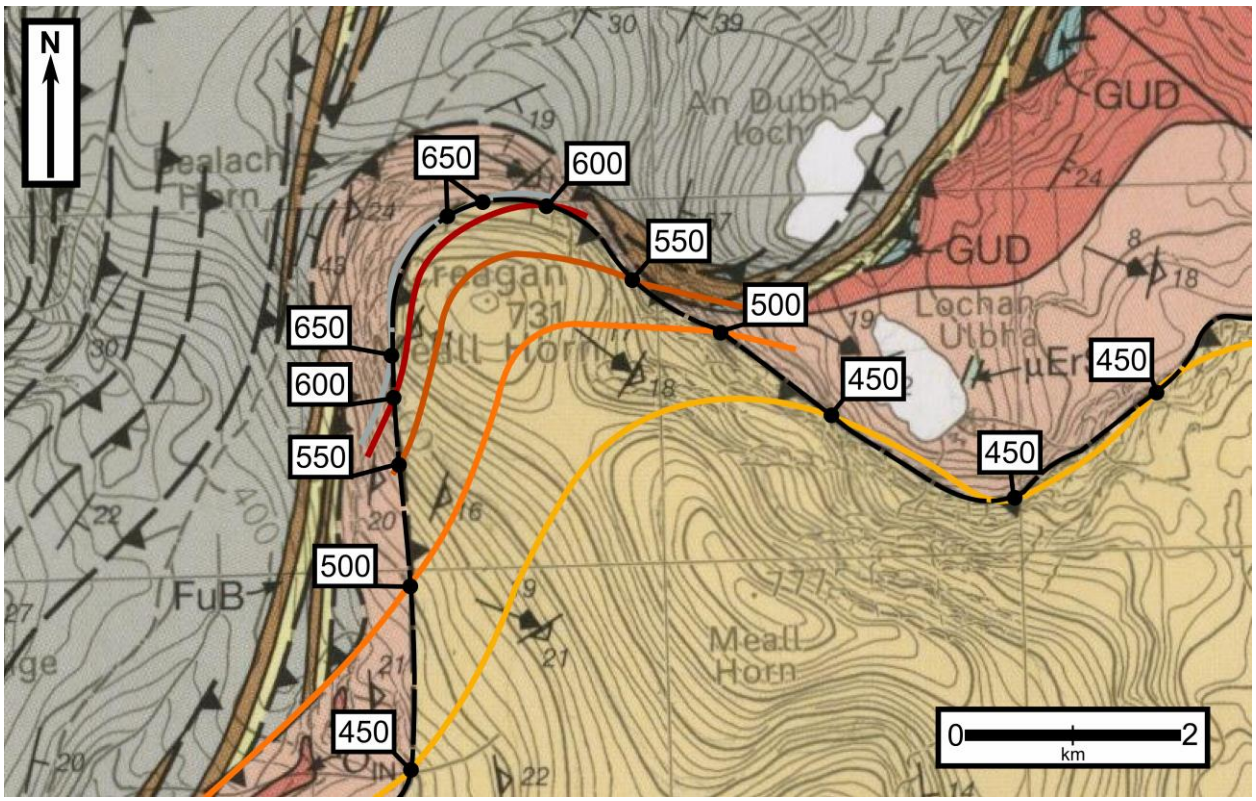

Fig. 3.8. An example of correlating between elevation control points along a salient on the Moine thrust. Elevation control points were constrained by the intersection of the Moine thrust with topographic contours. Figure adapted from BGS, Ben Hee (2009) Sheet.

Variation in spacing between structure contours on thrust faults traced perpendicular to strike may be used to infer the presence of frontal flats (wide contour spacing) and ramps (closer spacing) assuming the thrust surface has not been deformed since its initial formation. However, later flexing or folding of the original fault surface will distort this simple picture and may render the ramp-flat-ramp interpretation of structure contour spacing invalid. For example, formation of a thrust duplex in the footwall to the Glencoul thrust (Section 3.4.8) has bowed up the overlying thrust surface resulting in widely spaced structure contours on the part of the thrust surface situated over the crest of the underlying duplex, with more closely spaced contours at the trailing and leading edges of the duplex.

3.4 Geometry of Structure Contours on the Moine thrust

Structure contours constructed along the Moine thrust are shown in Figure 3.9. The structure contours indicate three distinct subsurface thrust surface geometries: synforms, antiforms, and relatively planar structures. The structure contour map indicates significant lateral variation in subsurface fault geometry traced along the length of the fault. Salients along the Moine thrust are characterized by either relatively planar geometries or broad synforms, recesses are associated with antiforms, and relatively linear segments of the fault are characterized by planar geometries. However, not all map-pattern curves on the Moine thrust are associated with subsurface geometry. For example, some curves are produced by a topographic 'cut' effect as the relatively planar Moine thrust 'Vs' up valleys. Structure contours constructed in these areas reflect this planar thrust geometry. Thrust plane dips measured from structure contour spacing are summarized in Table 3.1. Location numbers in Table 3.1 correspond to numbers between structure contour spacing on Figure 3.9.

Fig. 3.9. Next page. Structure contour map constructed from the North Coast to the Dundonnel area. Structure contours are given as meters above sea level and presented as both 50 m and 10 m contour intervals. 50 m intervals are displayed as solid lines with a specific color that reflects its elevation. Dashed meter lines denote where structure contours could not be drawn with confidence. 10 m contour intervals are displayed if 50 m control was not sufficient. These contours are shown by thin black lines. See Section 3.3 for more discussion on analytical techniques used.

Structure Contours of the Moine Thrust NW Scotland

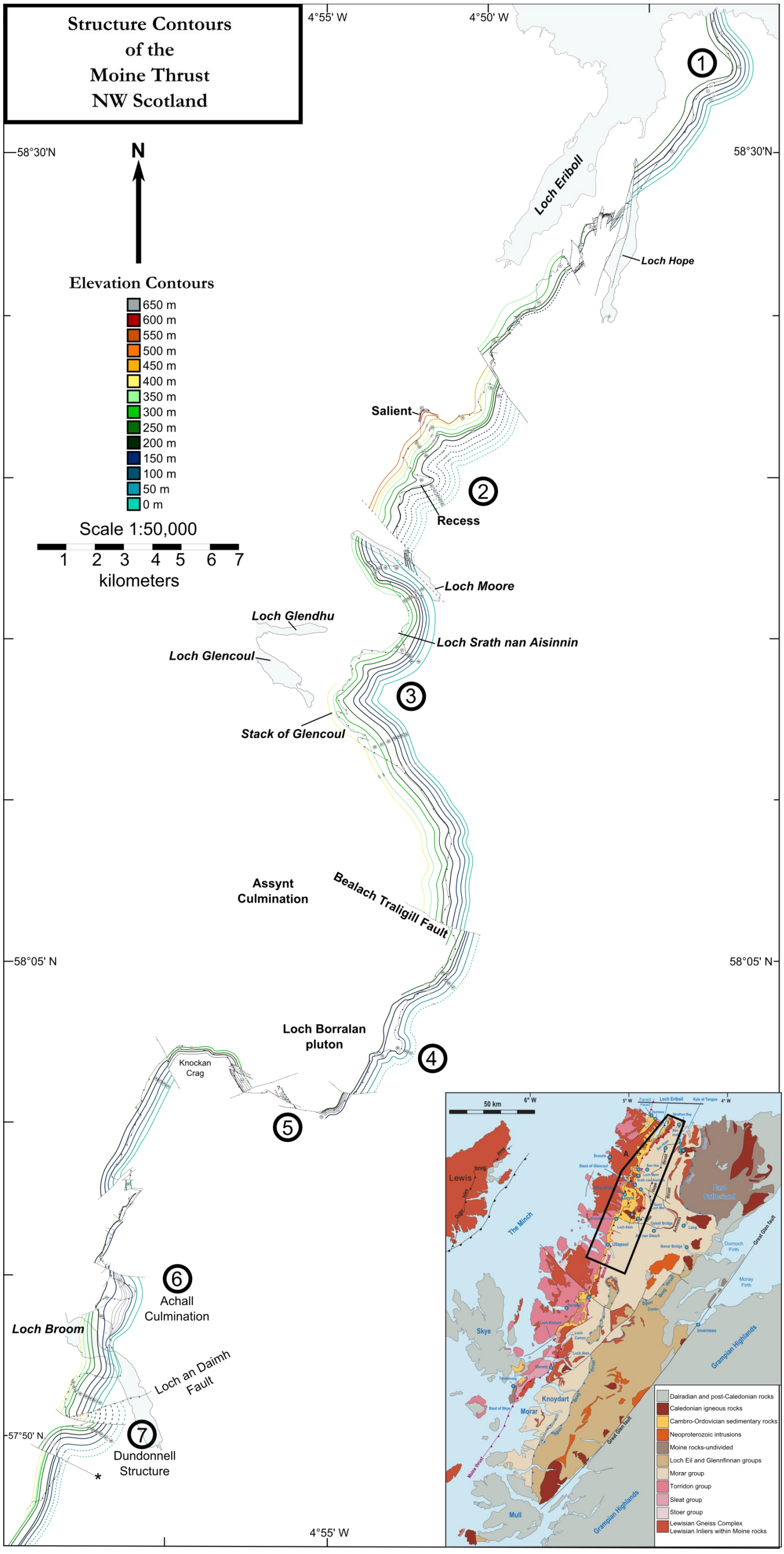

Table 3.1 **Thrust plane dips measured from structure contours of the thrust surface.**

Location	Dip °	Location	Dip°	Location	Dip°
1	3.5	41	6	81	5.5
2	4	42	7.5	82	1.8
3	2	43	4.5	83	1.8
4	4	44	3	84	2
5	3	45	4.5	85	5.5
6	2	46	6	86	5
7	4.5	47	6.5	87	5
8	6	48	5.5	88	2
9	1.5	49	3	89	3
10	2.5	50	6	90	3
11	7	51	1.5	91	3.5
12	9	52	4	92	2.5
13	12.5	53	4.5	93	6
14	6	54	4.5	94	4
15	4.5	55	2	95	4.5
16	2.5	56	1.8	96	3
17	9.5	57	2.5	97	3
18	3	58	1.8	98	2.5
19	4	59	3		
20	6.5	60	3.5		
21	15	61	4.5		
22	9	62	4		
23	4	63	4		
24	6.5	64	6		
25	3	65	4.5		
26	6	66	2.5		
27	6.5	67	2.5		
28	2.5	68	0.7		
29	1	69	3.5		
30	2.5	70	3		
31	3	71	6		
32	3	72	3		
33	3.5	73	2		
34	3	74	1.5		
35	12	75	7.5		
36	9	76	3.5		
37	5	77	3.5		
38	1.5	78	3.5		
39	3	79	3		
40	4	80	3		

Location numbers in Table 3.1 correspond to numbers between structure contour spacing of the thrust surface on Figure 3.9.

3.4.1 Tongue Sheet

To the east of Loch Eriboll (Location 1, Figure 3.9), the mapped position of the Moine thrust defines a recess that is ~0.7 km wide measured perpendicular to the west-east trending axis of the recess. Structure contours on the Moine thrust define an east plunging (085° trending) antiform that in map view is coincident with the axis of the recess. Traced southward, structure contours on the Moine thrust are essentially parallel to the map-view trace of the fault on the topographic surface; spacing between structure contours indicates that the relatively planar local fault surface dips at ~ 03˚ to the SE. Continuing further south; cross-faults cut the thrust surface near Loch Hope, and it is difficult to correlate structure contours across these faults. In this heavily cross-faulted area, 10 meter contours were used to determine dip direction of the thrust surface and to constrain overall geometry.

Structure contours constructed on the Moine thrust within the recess to the east of Loch Eriboll (Figure 3.10) are sub-parallel to foliation mapped in the overlying metasedimentary rocks of the Moine nappe (British Geological Survey, 1997; Holdsworth et al. 2001, p. 33; 2007, p. 125). Here foliation defines an east plunging antiform, with foliation in the Moine rocks on the north side of the recess dipping to the NE and foliation on the south side of the recess dipping SE. Mineral stretching lineations in the hanging wall to the Moine thrust trend sub-parallel to the east plunging antiformal hinge defined by structure contours and foliation. In contrast, foliation in the adjacent footwall rocks of the recess (composed of chlorite-muscovite schist - referred to as Oystershell Rock) has a fairly constant NNE strike and gentle dip to the ESE (Figure 3.10). Mineral stretching lineations in the footwall rocks plunge gently to the ESE, parallel to the inferred thrust transport direction. Within this part of the Moine thrust zone, the Oystershell Rocks attain their greatest outcrop width within the recess, with structural thicknesses decreasing traced both to the north and south away from the recess.

At first sight, the presence of a hanging wall antiform resting on a planar footwall suggests that the mapped recess may be the map expression of a detachment fold, forming over a weaker basal detachment horizon. Detachment folds form in hanging wall rocks where there is a significant thickness or competency contrast relative to footwall rocks (Mitra, 2003). Such

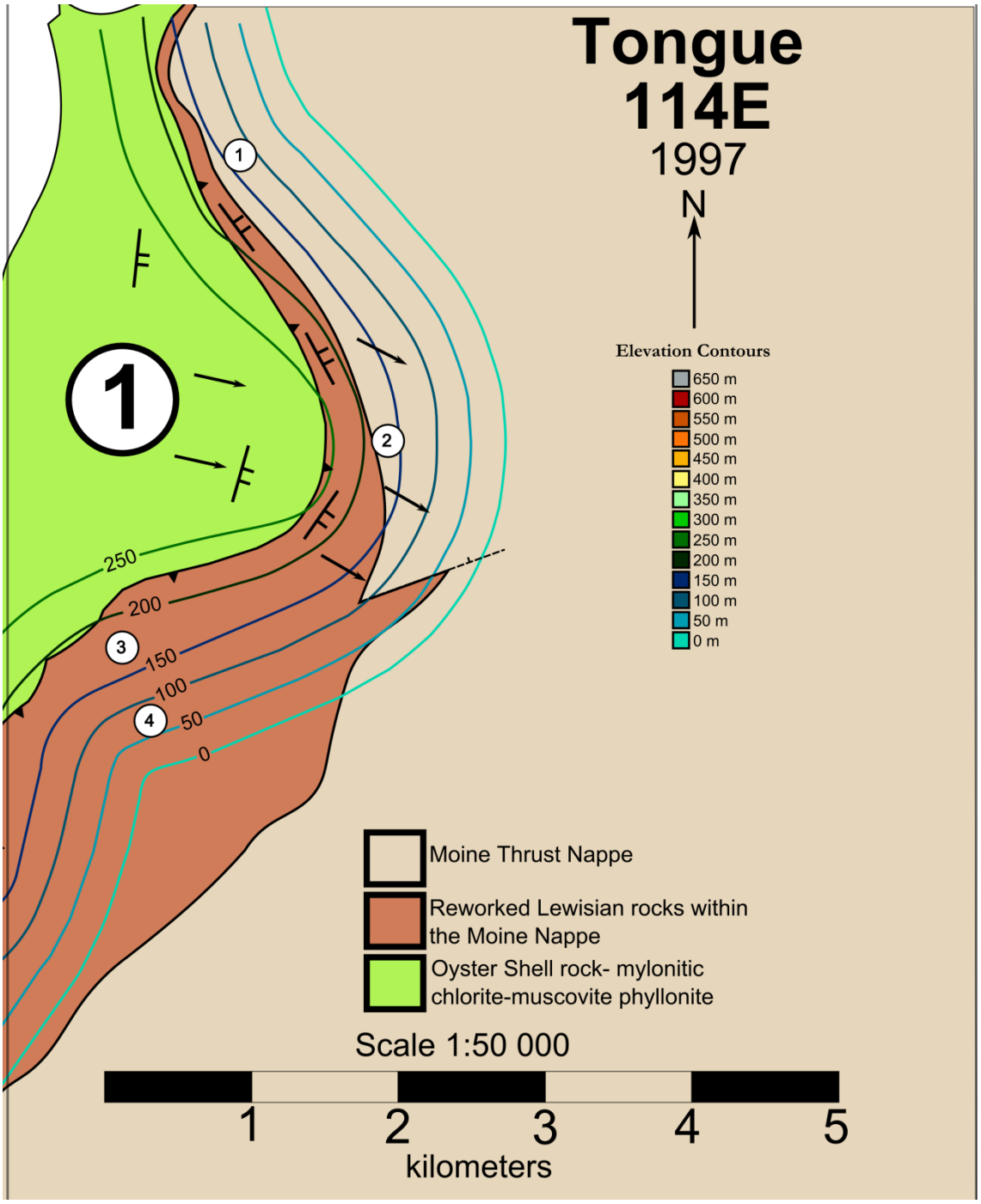

Fig.3.10. Simplified geologic map of a portion of the Moine thrust located to the east of Loch Eriboll showing lineation trend and foliation strike in the hanging wall and footwall of the Moine thrust. The antiformal structure in the hanging wall and planar geometry in the footwall implies detachment folding occurred above the weaker Oyster Shell rock. Figure adapted from BGS, Tongue (1997) Sheet. Foliation and lineation data from Holdsworth et al., 2001 p. 33, 2007, p. 125

folds have been identified in fold and thrust belts throughout the world (Jura Mountains, Central Appalachian fold belt, Brooks Range). However, a key feature of such detachment folds is that the underlying thrust/detachment surface remains relatively planar. This is clearly not the case here where structure contours indicate that the Moine thrust surface is itself sub-parallel to the overlying antiform defined by foliation in the hanging wall rocks. We interpret this antiformal structure as being an original transport-parallel corrugation in the thrust surface formed as the thrust sheet moved over a pre-existing structural high (or structural obstacle) that is flanked by lateral ramps dipping in opposite directions (i.e. to the NNE and SSW). In this interpretation, foliation in the hanging wall has been folded over this hinterland-plunging corrugation during thrusting (Figure 3.11).

3.4.2 Ben Hee Sheet

North of Loch More, a recess and salient pair on the Moine thrust is spatially associated with antiformal and synformal corrugations, respectively, defined by structure contours on the Moine thrust (Location 2, Figure 3.9).The crest of the antiform trends approximately 087˚, while the synform to the south is a broad SE-plunging fold with limb dips of ~04˚ (Figure 3.12)

Structure contours on the Moine thrust indicate that these structures are separated at depth by a relatively planar frontal ramp with structure contours indicating a dip of ~03-07˚SE. The pattern of structure contours constructed along the recess indicate that the Moine thrust in the subsurface, likely has the geometry of a hinterland plunging antiformal corrugation at depth that is flanked by lateral ramps dipping away from each other (Fig. 3.12). The pattern of structure contours associated with the salient to the north may be linked to a broad SE plunging synformal corrugation at depth that is flanked by lateral ramps that dip toward each other.

3.4.3 Assynt Special Sheet: Loch Srath nan Aisinnin Recess to Bealach Traligill Fault

North of the Assynt culmination and south of Loch More a major recess is observed in the mapped position of the Moine thrust which transitions laterally into a salient to the south, near the Stack of Glencoul (Location 3, Figure 3.9). Structure contours drawn on the Moine thrust within the recess define a broad antiformal structure with a crest that trends approximately

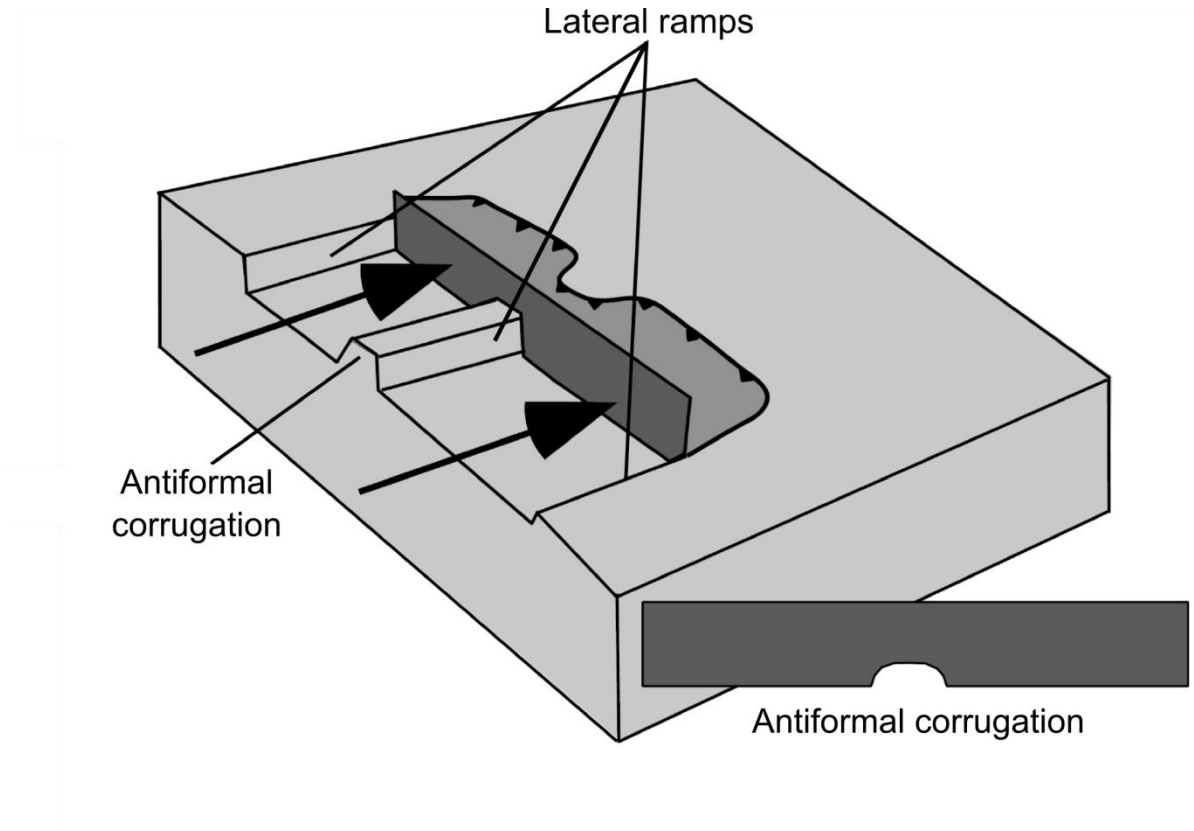

Fig. 3.11. Schematic 3D diagram of transport-parallel antiformal corrugation on the Moine thrust to the east of Loch Eriboll. Our interpretation of the structure east of Loch Eriboll is of an original transport parallel antiformal corrugation on the Moine thrust surface over which the Moine thrust sheet moved. Figure modified from Marshak (2004).

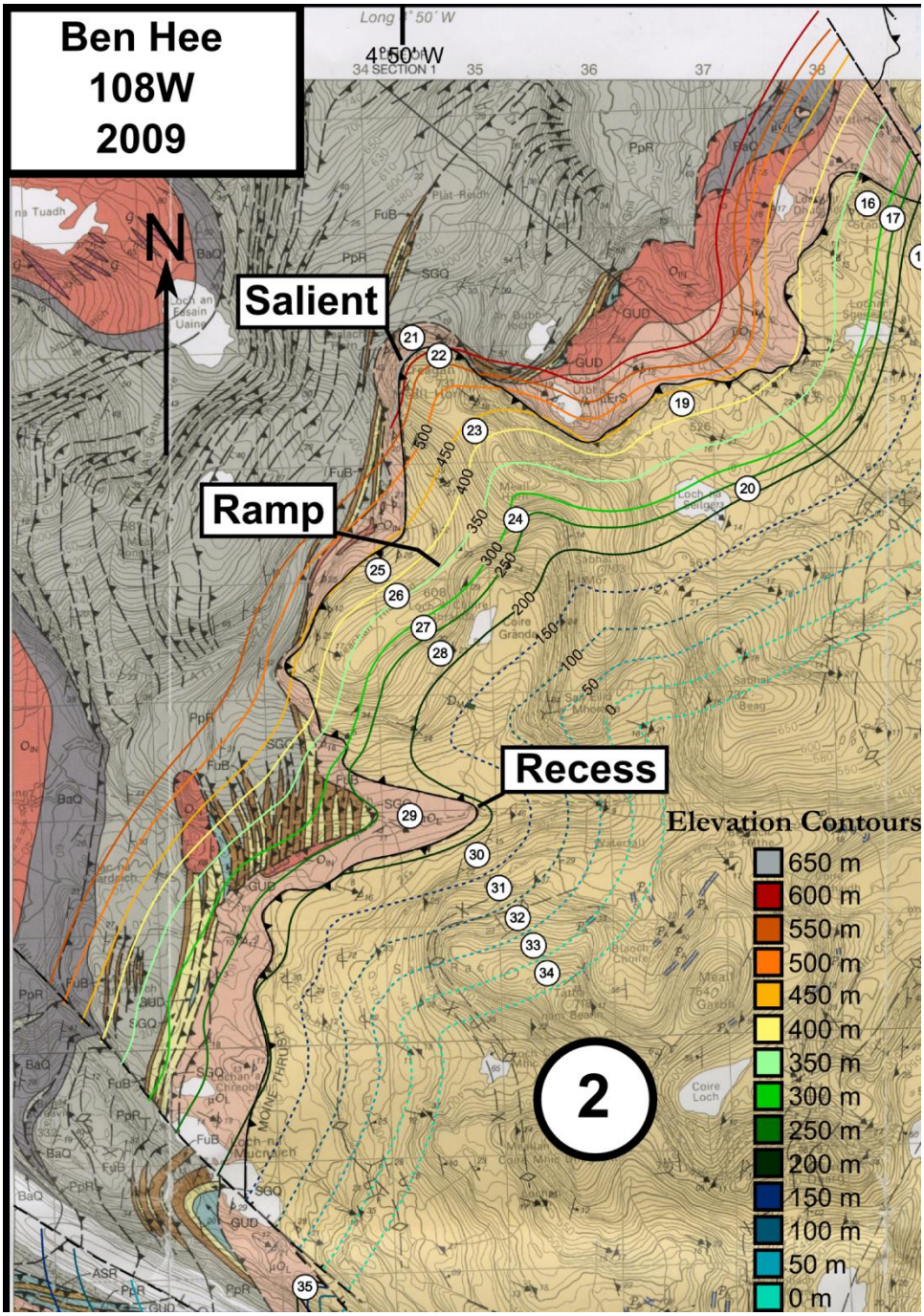

Fig. 3.12. Ben Hee BGS map with structure contours on the Moine thrust surface. The structure contours constructed in this area indicate a syncline-anticline pair associated with the salient and recess, respectively. Figure adapted from BGS, Ben Hee (2009) Sheet.

085˚. Within this major recess, a minor recess, with a crest trending approximately 130˚ at Loch Srath nan Aisinnin, is characterized by structure contours that are widely spaced over the recess and closely spaced to the east and west. At Loch Srath nan Aisinnin, Butler (1984) demonstrated that footwall imbrication led to a local bowing up of the Moine thrust in this area, thereby providing a potential explanation for the geometry indicated by the structure contours. Widely spaced structure contours represent the parts of the thrust surface that was bowed upward above the crest of the underlying footwall imbricates, while the more closely spaced contours are located at the leading and trailing edges of the footwall imbricate zone (Figure 3.13). The dip of the Moine thrust surface remains fairly constant subparallel to the limbs of the anticline (~05˚), except above the footwall imbricates where the bowing of the thrust surface is observed.

South of the Stack of Glencoul, along the northeastern margin of the Assynt culmination, structure contours parallel the relatively linear map trace of the Moine thrust, with only minor curvatures in the structure contours. Along this relatively planar section of the Moine thrust, structure contour spacing indicate that the dip of the thrust varies between ~02 - 06˚to the NE.

Along the eastern margin of the Assynt culmination, lateral continuity of the subsurface structure contours drawn on the Moine thrust is disrupted by the sinistral Bealach Traligill Fault (Krabbendam and Leslie, 2010). Structure contours are offset by between ~0.5-0.8 km and indicate that the cross-fault extends further to the east than mapped by the BGS, based on the lack of lateral continuity between contours to the east of the Moine thrust. Structure contours on the Moine thrust to the south of the Bealach Traligill Fault indicate a relatively planar geometry that parallels the map trace of the Moine thrust. Dips indicated by structure contours on the Moine thrust to the south of the cross-fault range between ~3 - 6˚ to the SE. These structure contours indicate that the thrust maintains a planar geometry traced southwards from the Bealach Traligill Fault to the southeast margin of the Assynt culmination, near the Loch Borralan Pluton.

3.4.4 Oykel Bridge Sheet: Loch Borralan Pluton

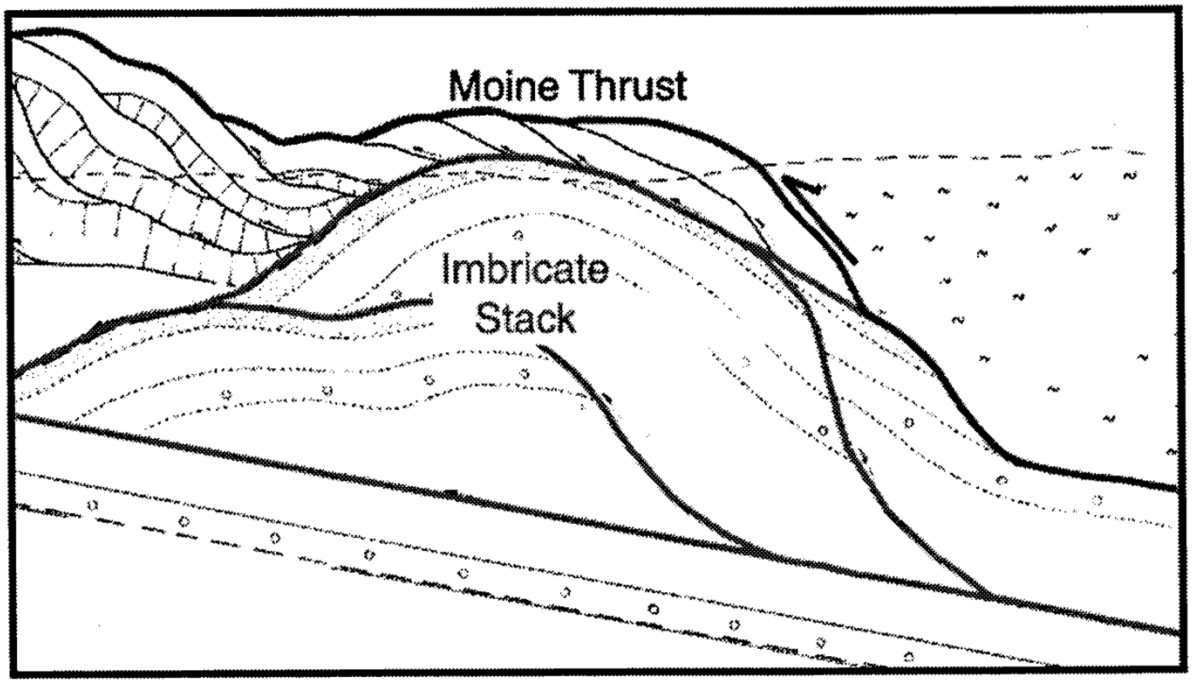

Fig. 3.13. Cross-section of the footwall imbricates observed in the footwall to the Moine thrust at the Loch Srath nan Aisinnin recess. Spacing of structure contours on the Moine thrust vary in map view due to local bowing up of the thrust surface as a result of motion on the underlying footwall imbricate zone, producing an apparent ramp-flat-ramp pattern of structure contours. Figure from Butler (1984).

Along the southeast margin of the Assynt culmination, a minor recess in the map trace of the Moine thrust appears to be associated with the Loch Borralan Pluton that is located in the footwall to the west (Location 4, Figure 3.9). Structure contours constructed across the recess indicate that the Moine thrust is warped about a broad ESE (105°) plunging antiform (Figure 3.14). This 'antiform' could either be an original corrugation on the thrust surface or due to later upwarping associated with magma intrusion or footwall imbrication. The Borralan pluton is believed to have been intruded during movement on the Moine thrust zone in southern Assynt (Halliday et al. 1987; Goodenough et al., 2011). If movement on the local segment of the Moine thrust predated or was synchronous with magma intrusion (as suggested by the data of Goodenough et al., 2011) then this antiformal warping of the Moine thrust could be due to magma intrusion in the footwall to the east of the current map position of the thrust, with more widely spaced structure contours over the crest of the intrusion (Figure 3.14).

3.4.5 Ullapool Sheet: Southern margin of Assynt Culmination

Along the southern margin of the Assynt culmination, the map trace of the Moine thrust defines a large-scale salient-recess pair (Location 5, Figure 3.9). In this area, the map trace of the Moine thrust changes from the regional ~ NNE-SSW trend (north coast to southern Assynt) to an approximately W-E trend for ~6 km, before resuming the regional NNE-SSW trend near Knockan Crag. Associated with this change in trend is a change in observed deformation microstructures / mechanisms on the Moine thrust (see review by Law and Johnson 2010, p. 474-475). Along the NNE-trending trace of the Moine thrust, located to the north of the southern margin of the Assynt Culmination, deformation is dominated by crystal plastic (ductile) processes. In contrast, along the W-E trending trace of the Moine thrust that defines the southern margin of the Assynt Culmination - and from there southwards to Skye - deformation on the Moine thrust is dominated by brittle fracturing processes.

Clearly the southern margin of the Assynt Culmination separates two fundamentally different segments of the Moine thrust, and the possibility that these two segments may be different faults (albeit with each carrying Moine Supergroup rocks in their hanging walls) needs to be tested. In the simplest possible scenario, if the two fault segments are part of a single

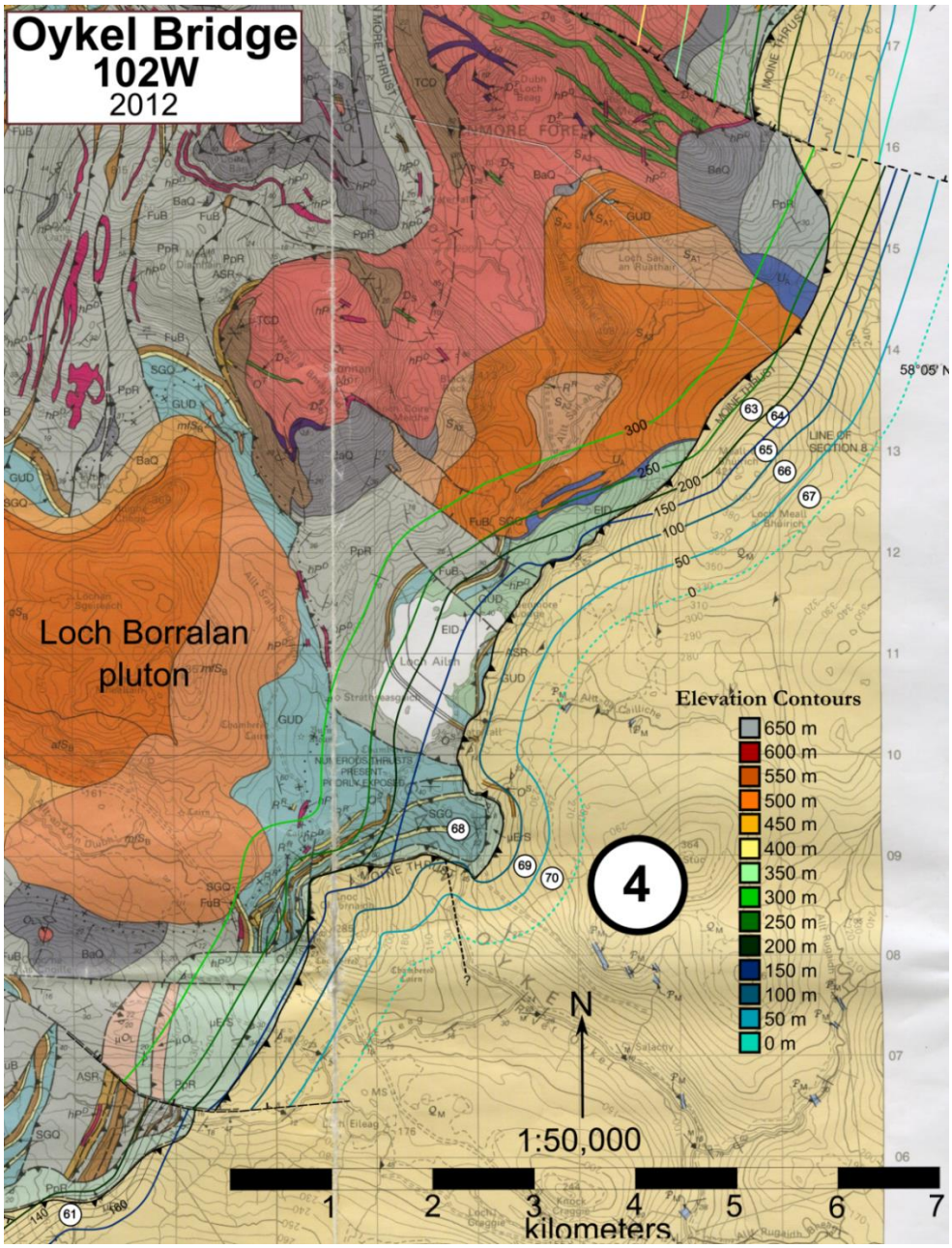

Fig. 3.14. Oykel Bridge BGS map with structure contours on the Moine thrust surface. Structure contours constructed along the recess display broad antiformal pattern with apparent ramp-flat-ramp geometry flanked by potential lateral ramps. Alternatively, either footwall imbrication or syn-orgogenic alkaline magmatism related to emplacement of the Loch Borralan pluton could have bowed up the overlying thrust surface with the flat lying thrust surface (wide structure contour spacing) located above the crest of the intrusion. Figure adapted from BGS, Oykel Bridge (2012) Sheet.

structure then it might be expected that structure contours on the fault surface(s) can be readily traced from one segment to the next. In contrast, if the fault segments are different structures then no lateral continuity would be expected between structure contours drawn on the two faults. Unfortunately, the drawing of structure contours along the southern margin of the Assynt Culmination (Figure 3.9) has proved problematic due to: 1) lack of detailed topographic control (poor exposure and low lying topography), 2) very gentle dips (local sections of the fault's map trace parallel topographic contours) and, 3) cross-faults off-setting the map trace of the thrust, making it extremely difficult to accurately construct structure contours. 10 meter contours were used to accurately constrain dip direction and overall geometry along individual km-scale sections of the thrust fault but, even so, little useful geometric information could be obtained from contouring through this area.

To the east of Knockan Crag (Figure 3.9), near the trough of the salient, an increase in map density of topographic control points allows us to construct structure contours with more confidence. The structure contours indicate that the Moine thrust in this local area is relatively planar with dips of between ~ 02˚SE and 07˚S. To the southwest of Knockan Crag, a dextral cross-fault off-sets the trace of the Moine thrust. Off-set of structure contours on the Moine thrust increases to the southeast along this cross-fault (Figure 3.9), suggesting a 'scissor' type motion on the cross-fault. In addition, lack of lateral continuity across this cross-fault indicates that the mapped trace of these faults by the BGS may extend further eastward than shown on the maps.

To the south of this cross-fault, structure contours are essentially parallel to the map trace of the Moine thrust indicating a relatively planar fault surface; contour spacing indicates that the thrust dips at ~03˚to the SE. These linear structure contours suggesting planar geometries were constructed across minor salients and recesses, with excellent topographic control, indicating that the curvature in map-pattern is caused by the intersection of a relatively planar Moine thrust with valleys in this region, rather than by corrugation on the fault in the subsurface, as described in previous sections.

3.4.6 Ullapool Sheet: Achall Culmination

The Achall Culmination (or antiform) is located ~ 3 km to the NE of Ullapool (Location 6, Figure 3.9) and exposed in the Ullapool River valley (see field guide by Leslie and Goodenough 2011). The crest of the antiform plunges towards ~ 098˚. The Moine thrust, which defines the north, south and eastern margins of this culmination, 'Vs' up valley towards the east producing a local recess in map view. Structure contours on the Moine thrust indicate that this 'V' pattern is not simply due to the intersection of topography with a planar Moine thrust (cf. area to the north described above), but that the thrust is gently curved above the culmination exposed in its footwall with limb dips of approximately 1-2˚. Structure contours on the Moine thrust traced across the salient located immediately to the south of the Achall Culmination define a broad SE-plunging synformal structure.

3.4.7 Loch Fannich Sheet: Dundonnell Structure

The Dundonnel Structure is located in a structurally complex area to the south of Loch Broom (Location 7, Figure 3.9). The Moine thrust is warped over this structure. Topographic control for drawing structure contours on the Moine thrust is severely limited in this area, with control points only present for one elevation contour. In this case, we used published field observations to guide structure contour construction. Leslie et al. (2010) have interpreted the Dundonnel Structure as a steeply inclined imbricate stack of minor thrusts, that lacks antiformal folding, and is offset by the Loch an Daimh fault. Others have interpreted the Dundonnel Structure as a classic antiformal-stack duplex (Elliot and Johnson, 1980; Boyer and Elliot, 1982; Butler and Matthews, 2009). Our structure contours were constructed using the most recent British Geological Survey (2011) mapping which reflects the interpretation of Leslie et al. (2010). The resultant structure contours on the Moine thrust therefore also reflect this interpretation, indicating a ramp structure with only slight antiformal folding (Figure 3.15).These structure contours on the Moine thrust differ greatly from those constructed by Elliot and Johnson (1980), which reflect their interpretation of the Dundonnel Structure as an antiformal stack duplex.

Structure contours drawn across the salient in the trace of the Moine thrust located immediately to the south of the Dundonnell Structure indicate a broad synformal structure

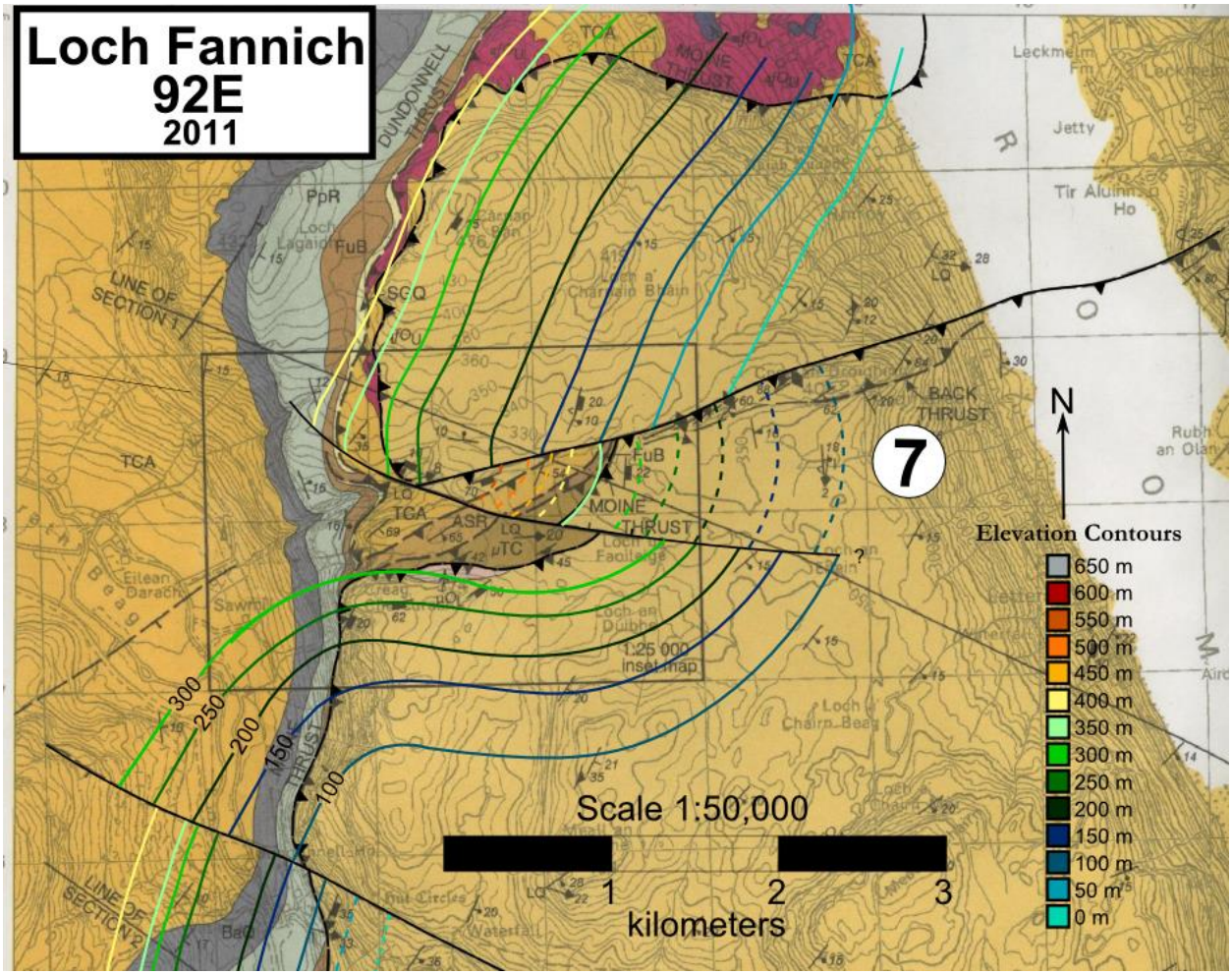

Fig. 3.15. Loch Fannich BGS map with structure contours on the Moine thrust surface. Structure contours constructed on the Dundonnel Structure reflect the stacked imbricate interpretation of Leslie et al. (2010), with relatively planar ramp geometry. Figure adapted from BGS, Loch Fannich (2011) Sheet.

plunging to the SSE. A cross-fault appears to truncate these structure contours with a sinistral off-set of approximately 250 meters. To the south of the cross-fault structure contours indicate that the Moine thrust is relatively planar and strikes parallel to the map trace of the thrust.

A salient in the trace of the Moine thrust has also been mapped to the north of the Dundonnel Structure on the south side of Loch Broom. Structure contours across this salient indicate at least here that the thrust is a relatively planar feature with dips between ~3 and 6˚to the SE. This serves to illustrate that not all salients (and probably recesses) in the map trace of the Moine thrust are of structural origin, but in some cases may simply be due to topographic 'cut' effects.

3.5 Geometry of structure contours on the Glencoul thrust*: the Glencoul thrust / Ben More thrust controversy - Assynt Sheet*

Structure contours constructed along the Glencoul thrust surface, as depicted on the original Geological Survey maps (Peach et al., 1907; British Geological Survey, 1923), were used to assess the validity of the Krabbendam and Leslie (2004) re-interpretation of structural relationships between the Glencoul and Ben More thrusts. Structure contours constructed on the Glencoul thrust to the SW of Loch Glencoul correlate with structure contours to the NE of Loch Glencoul, indicating that these segments are part of the same structure (Figure 3.16). Structure contours along the fault surface on the north side of Loch Glencoul are closely spaced to the NW and SE, with widely spaced contours in between. This geometric pattern of structure contours could be interpreted as indicating the presence of ramp-flat-ramp geometry on the Glencoul thrust. However, the domain of widely spaced contours is located over the crest of a duplex in its footwall rocks, first recognized by Callaway (1883). Along the northern shore of Loch Glencoul this duplex can be seen to have bowed up the surface of the overlying Glencoul thrust in to a broad antiform. The more closely spaced structure contours on the Glencoul thrust are located over the leading (NW) and trailing (SE) edges of the duplex (Figure 3.17).

The correlation between structure contours along the mapped trace of the Glencoul thrust to the NE and SW of Loch Glencoul strongly indicates that the recent reinterpretation of the Glencoul and Ben More thrusts by Krabbendam and Leslie (2004) cannot be correct. Our

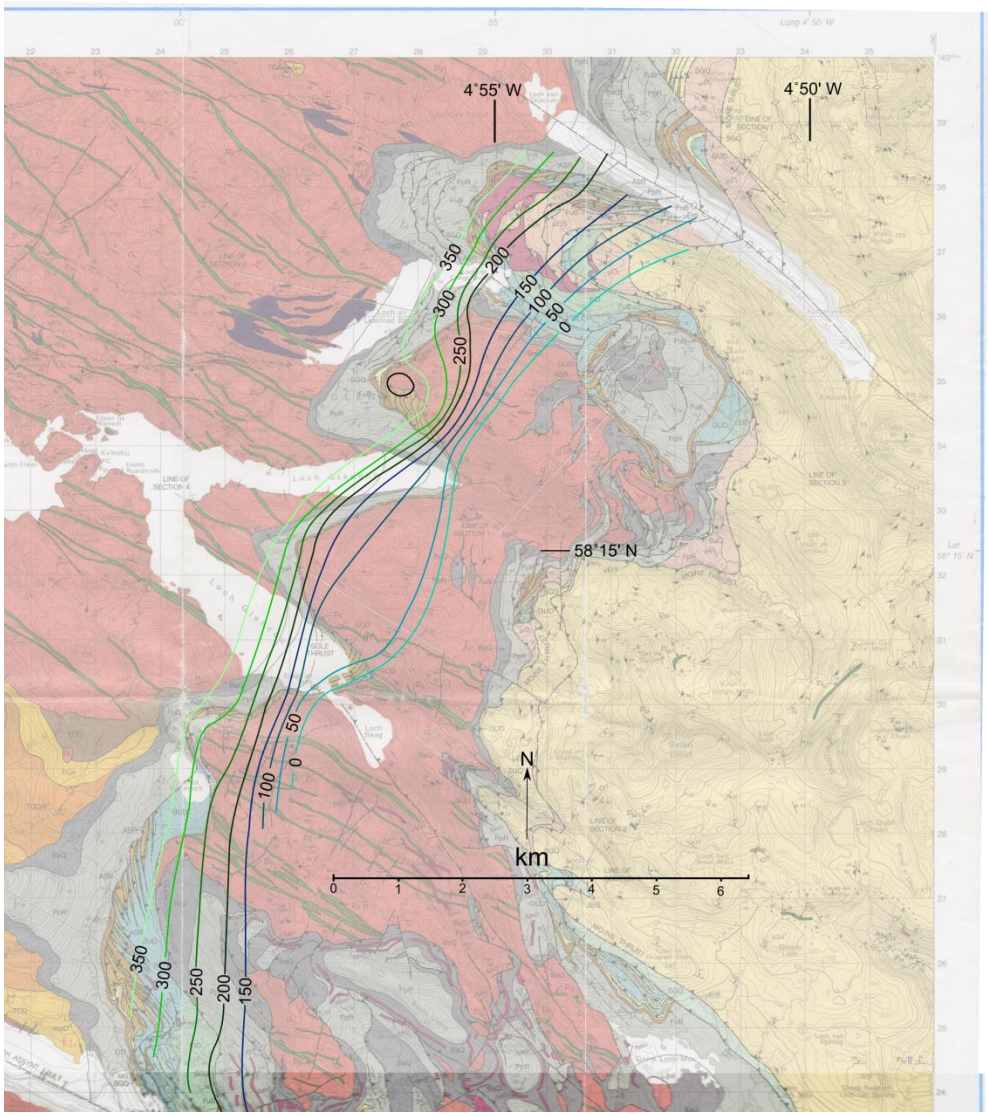

Fig. 3.16. Structure contour map constructed along the (BGS, 1923) Glencoul thrust, as depicted on the original Geological Survey maps for the Assynt region. Structure contours confirm that the thrust segments to the SW and NE of Loch Glencoul are part of the same structure. Structure contours constructed on Assynt Special Sheet (BGS, 2007).

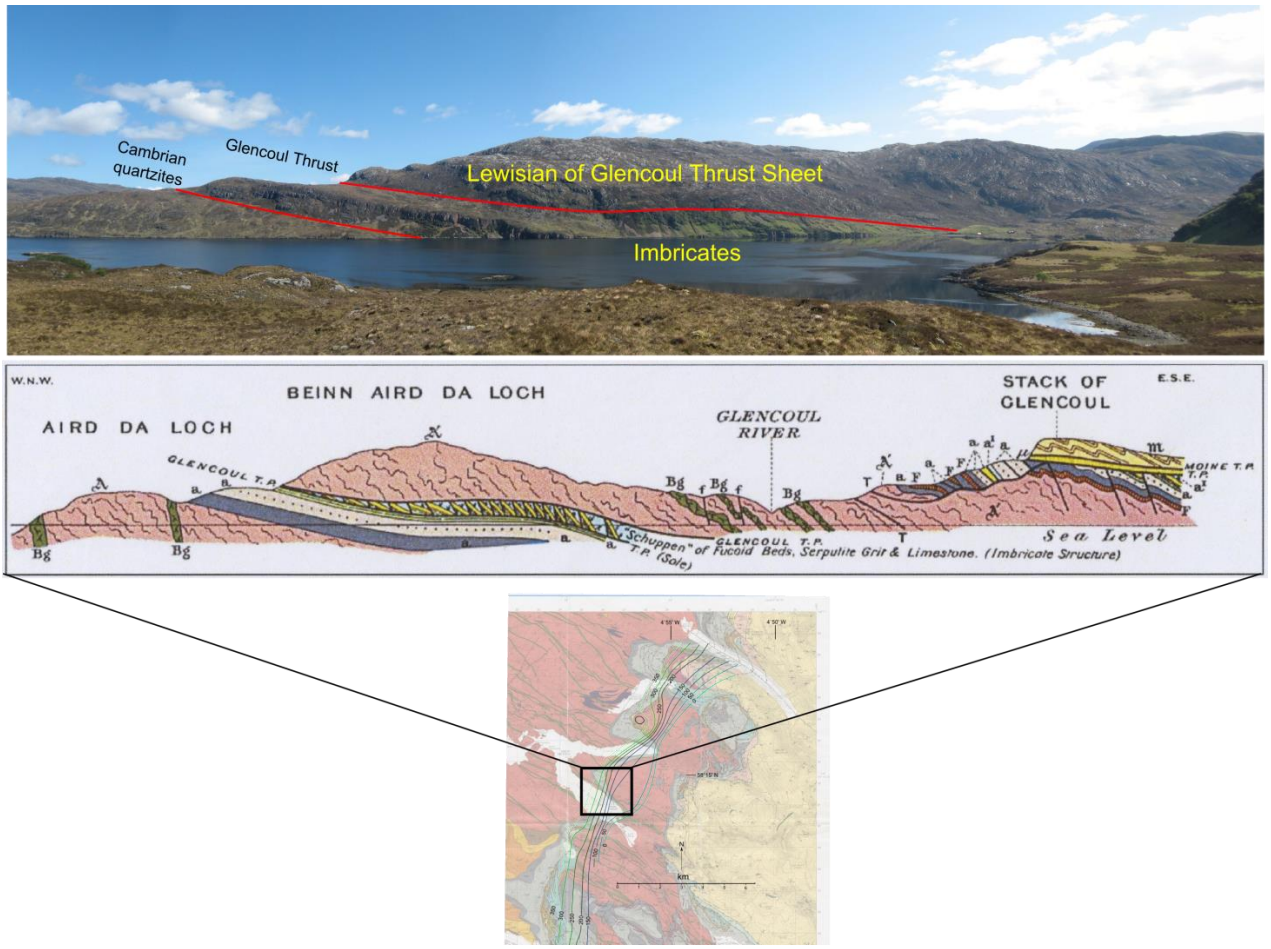

Fig. 3.17. Top image: displays the famous view of the thrust surface on the NE side of Loch Glencoul. Middle image: displays the cross-section shown on the 1923 BSG Assynt Special Sheet (see also Peach et al., 1907) for this segment of the thrust, showing a footwall duplex that has locally bowed up the overlying thrust surface. Bottom image: Structure contours drawn on the Glencould thrust as originally mapped by Survey geologists to the SW and NW of Loch Glencoul. Structure contours to the NE of Loch Glencoul are widely spaced over the footwall duplex (top and middle images) and more closely space at the leading and trailing edges of the duplex. Field photograph provided courtesy of Rob Butler.

structure contours demonstrate that the segments of the Glencoul thrust, as originally mapped by Survey geologists (Peach et al., 1907; British Geological Survey, 1923) to the NE and SW of Loch Glencoul are part of the same structure. This interpretation also supports the local foreland propagating nature of thrusts within the Assynt culmination, as suggested by Elliot and Johnson (1980). As shown in Figure 3.6, propagation of the younger Glencoul thrust from beneath the Ben More thrust results in truncation of the overlying thrust sheet along a branch line that lies at, or to the south of Loch Glencoul (Figure 3.5).

3.6 Discussion

3.6.1 Validity of structure contours

We believe that structure contours constructed using mapped intersections of the Moine thrust with topographic contours provides an excellent way to the characterize subsurface geometry of the fault in areas of tight topographic control although, by the nature of the data used, signify down (or up) dip projections of the fault surface are of limited validity. It is acknowledged that interpretation of structural contours in areas of minimal topographic control should only be regarded as 'most likely' solutions, based on adjacent structural geometries combined with the topographic control points available in the area. Following the analytical approach recommended by Groshong (2006) for areas with multiple possible ways to draw structure contours, the least complex structural interpretation was taken.

3.6.2 Interpretation of thrust surface dips based on structure contour spacing

Local estimates of dip on the Moine thrust based on structure contour spacing are summarized in Table 3.1. Comparison of these data with the orientation of local foliation shown on the BGS maps in the Moine metasedimentary rocks of the hanging wall generally indicates that although the local strike of the thrust indicated by structure contours is sub-parallel to strike of the overlying foliation, observed foliation dips are typically 5-10˚ higher than the local dip of the thrust surface indicated by structure contour spacing.

Variation in spacing between structure contours on thrust faults traced perpendicular to strike may be used to infer the presence of frontal flats (wide contour spacing) and ramps

(closer spacing) assuming the thrust surface has not been deformed since its initial formation. However later flexing or folding of the original fault surface will distort this simple picture and may render the flat-ramp-flat interpretation of structure contour spacing invalid. For example, formation of a thrust duplex in the footwall to the Glencoul thrust (Section 3.8) has bowed up the overlying thrust surface resulting in widely spaced structure contours on the part of the thrust situated over the crest of the underlying duplex, and more closely spaced contours at the trailing and leading edges of the duplex.

3.7 Conclusions

A. Structure contours on the Moine thrust indicate that the thrust surface while relatively planar at the regional scale is locally corrugated. These 'antiformal' and 'synformal' corrugations trend sub-parallel to the thrust transport direction and are probably original features of the thrust surface (possibly flanked by lateral ramps), rather than due to later folding associated with along-orogen-strike compression. To the east of Loch Eriboll foliation in the overlying Moine metasedimentary rocks is folded about an 'antiformal' corrugation on the thrust surface, while foliation in the footwall rocks remains planar. Folding of foliation in the hanging wall rocks is thought to have occurred during WNW-directed transport of the hanging wall rocks over this hinterland-plunging corrugation.
B. Lack of lateral continuity between structure contours on the Moine thrust indicates that cross-faults mapped by BGS off-setting the Moine thrust may likely extend further eastward than shown on the BGS maps. Eastward tracing of these cross-faults at ground surface in to the hanging wall Moine rocks is difficult because of the lack of lithologic marker units in the Moine needed for demonstrating fault off-sets.
C. Either footwall imbrication of syn-orogenic alkaline magmatism (Halliday et al., 1987; Goodenough et al., 2011) may have led to local (km-scale) bulging of the Moine thrust in the southeastern part of the Assynt area.
D. Lack of topographic control for drawing structure contours on the section of the Moine thrust that defines the southern margin of the Assynt Culmination has left open the

question of whether the sections of the Moine thrust mapped to the north and south of this area are: 1) the same structure (albeit either originally located at different structural depths or associated with different rates of penetrative shearing) or are different regional-scale structures that developed at different crustal levels and/or times.

E. Sections of the Moine thrust with relatively linear map traces are characterized by structure contours on the thrust that indicate fairly planar fault segments. Salients along the map trace of the Moine thrust are usually characterized by structure contours that indicate broad 'synformal' geometries for the local fault surface. In contrast, recesses on the map trace of the Moine thrust are usually characterized by structure contours that indicate tighter 'antiformal' geometries for the local fault surface. These generally transport-parallel hinterland-plunging 'synforms' and 'antiforms' are probably original corrugations on the fault surface, rather than being produced by later along-orogenic-strike compression. Structure contours indicate that only a few of the mapped salients and recesses on the map trace of the Moine thrust are entirely due to a topographic cut effect.

F. Structure contours on the Glencoul thrust confirm that the thrust segments mapped on the NE and SW sides of Loch Glencoul and extending to the eastern end of Loch Glendhu are parts of the same structure as mapped by the original Survey Geologists at the end of the nineteenth century, rather than different structures as has recently been proposed by BGS geologists (Krabbendam and Leslie, 2004). Our interpretation also supports the foreland propagating nature of the Assynt culmination proposed by Elliot and Johnson (1980), with structure contours supporting the interpretation that the Glencoul thrust is the younger thrust in the region and that the Ben More thrust is truncated to the south of Loch Glencoul.

References

Alsop, G. I., Cheer, D. A., Strachan, R. A., Krabbendam, M., Kinny, P. D., Holdsworth, R. E., and Leslie, A. G., 2010, Progressive fold and fabric evolution associated with regional strain gradients; a case study from across a Scandian ductile thrust nappe, Scottish Caledonides. In: Law, R.D., Butler, R.W.H., Holdsworth, R.E., Krabbendamn, M., Strachan, R.A., (Eds.) Continental tectonics and mountain building; the legacy of Peach and Horne: Geological Society of London Special Publications, v. 335, p. 255-274.

Bailey, E. B., 1935, The Glencoul nappe and the Assynt culmination [Scotland]: Geological Magazine, v. 850, p. 151-165.

Billings, M.P., 1954, Structural geology (second edition): Englewood Cliffs, New Jersey, Prentice-Hall, 514 p.

Bird, K. J., 1988, 16. Structure contour and isopach maps of the National Petroleum Reserve in Alaska: US Geological Survey Professional Paper 1399, p. 355.

Boyer, S. E., and Elliott, D., 1982, Thrust systems: American Association of Petroleum Geologists Bulletin, v. 66, p. 1196-1230.

British Geological Survey, 1923, Assynt Special Sheet, Geological Map of the Assynt District at 1:63,360, Geological Survey of Great Britain (Scotland): Reprinted 1965 by Ordnance Survey for the British Geological Survey, Chessington, Surrey.

British Geological Survey, 1997, Tongue. Sheet 114E. Solid Geology. 1:50,000. Keyworth, Nottingham: British Geological Survey.

British Geological Survey, 2002, Loch Eriboll. Scotland Sheet 114W. Solid Geology. 1:50,000. Provisional Series. Keyworth, Nottingham: British Geological Survey.

British Geological Survey, 2007, Assynt. Scotland Special Sheet. Bedrock. 1:50,000 Geology Series. Keyworth, Nottingham: British Geological Survey.

British Geological Survey, 2008, Ullapool. Scotland Sheet 101E. Bedrock. 1:50,000 Geology Series. Keyworth, Nottingham: British Geological Survey.

British Geological Survey, 2009, Ben Hee. Scotland Sheet 108W. Bedrock. 1:50,000 Geology Series. Keyworth, Nottingham: British Geological Survey.

British Geological Survey, 2011, Loch Fannich. Scotland Sheet 92E. Bedrock. 1:50,000 Geology Series. Keyworth, Nottingham: British Geological Survey.

British Geological Survey, 2012, Oykel Bridge. Scotland Sheet 102W. Bedrock. 1:50,000 Geology Series. Keyworth, Nottingham: British Geological Survey.

Butler, R. W. H., 1984, Structure evolution of the Moine thrust belt between Loch More and Glendhu, Sutherland: Scottish Journal of Geology, v. 20, p. 161-179.

Butler, R. W. H., 2004b, The nature of "roof thrusts" in the Moine thrust belt, NW Scotland: implications for the structural evolution of thrust belts: Journal of the Geological Society of London, v. 161, p. 849-859.

Butler, R. W. H., and Matthews, S. J., 2009, Moine thrust belt; Slioch-Heights of Kinlochewe (NG 989 707-NH 089 649): Geological Conservation Review Series, v. 34, p. 302-307.

Butler, R. W. H., 2010a, The geological structure of the north-west Highlands of Scotland; revisited; Peach et al. 100 years on. In: Law, R.D., Butler, R.W.H., Holdsworth, R.E., Krabbendamn, M., Strachan, R.A., (Eds.), Continental tectonics and mountain building; the legacy of Peach and Horne: Geological Society of London Special Publications, v. 335, p. 7-27.

Butler, R.W.H., 2010b, The role of thrust tectonic models in understanding structural evolution in NW Scotland. In: Law, R.D., Butler, R.W.H., Holdsworth, R.E., Krabbendamn, M., Strachan, R.A., (Eds.), Continental tectonics and mountain building; the legacy of Peach and Horne: Geological Society of London Special Publications, v. 335, p. 293-320.

Coward, M. P. 1985. The thrust structures of southern Assynt, Moine thrust zone: Geological Magazine, v. 122, p. 1–13.

Elliott, D., and Johnson, M. R. W., 1980, Structural evolution in the northern part of the Moine thrust belt, NW Scotland: Transactions of the Royal Society of Edinburgh, v. 71, p. 69-96.

Goodenough, K. M., Millar, I., Strachan, R. A., Krabbendam, M., and Evans, J. A., 2011, Timing of regional deformation and development of the Moine thrust zone in the Scottish Caledonides; constraints from the U-Pb geochronology of alkaline intrusions: Journal of the Geological Society of London, v. 168, p. 99-114.

Groshong, R. H., 2006, 3-D Structural Geology: A Practical Guide to Quantitative Surface and Subsurface Map Interpretation, Springer.

Halliday, A. N., Aftalion, M., Parsons, I., Dickin, A. P., and Johnson, M. R. W., 1987, Syn-orogenic alkaline magmatism and its relationship to the Moine Thrust zone and the thermal state of the lithosphere in NW Scotland: Journal of the Geological Society of London, v. 144, p. 611-617.

Holdsworth, R. E., Strachan, R. A., and Alsop, G. I., 2001, Solid geology of the Tongue District; memoir for 1:50,000 geological sheet 114E (Scotland), British Geological Survey.

Holdsworth, R. E., Alsop, G. I., and Strachan, R. A., 2007, Tectonic stratigraphy and structural continuity of the northernmost Moine thrust zone and Moine Nappe, Scottish Caledonides. In: Ries, A.C., Butler, R.W.H., Graham, R.H., (Eds.), Continental tectonics; a discussion meeting in memory of the life and work of Mike Coward: Geological Society of London Special Publications, v. 272, p. 121-142.

Kinny, P.D., Friend, C.R.L., Strachan, R.A., Watt, G.R., and Burns, I.M., 1999, U–Pb geochronology of regional migmatites in East Sutherland, Scotland: evidence for crustal melting during the Caledonian orogeny: Journal of the Geological Society, London, v. 156, p. 1143–1152.

Krabbendam, M., and Leslie, G., 2004, Lateral ramps and thrust terminations; an example from the Moine thrust zone, NW Scotland: Journal of the Geological Society of London, v. 161, p. 551-554.

Law, R.D., and Johnson, M.R.W., 2010, Microstructures and crystal fabrics of the Moine thrust zone: history of research and changing tectonic interpretations. *In:* Law, R.D., Butler, R.W.H., Holdsworth, R., Krabbendam, M. & Strachan, R.A. (Eds.), Continental Tectonics and Mountain Building - The Legacy of Peach and Horne: Geological Society of London Special Publication, v. 335, p. 443-503. doi 10.144/SP335.21

Leslie, A.G., and Goodenough, K.M., 2011, Ullapool River, Creag nam Broc and Glen Achall. In: Goodenough, K.M., Krabbendam, M., (eds.) A geological excursion guide to the North-West Highlands of Scotland: Edinburgh Geological Society, p. 85-92.

Leslie, A.G., Goodenough, K.M., and Krabbendam, M., 2010, A ruck, a ramp and imbricate stack, but no culmination – the Dundonnell sector of the Caledonian Moine Thrust Belt, Northwest Highlands of Scotland [abstract] In: *Tectonic Studies Group Birmingham 2010, Birmingham, UK, 8-10 Jan 2010*. (Unpublished)

Marshak, S., 2004, Salients, recesses, arcs, oroclines, and syntaxes; a review of ideas concerning the formation of map-view curves in fold-thrust belts: American Association of Petroleum Geologists Memoir, v. 82, p. 131-156.

Mitra, S., 2003, A unified kinematic model for the evolution of detachment folds: Journal of Structural Geology, v. 25, p. 1659-1673.

Peach, B. N., Horne, J., Gunn, W., Clough, C. T.,Hinxman, L. W., and Cadell, H. M., 1888, Report on the recent work of the Geological Survey in the Northwest Highlands of Scotland, based on the field notes and maps of Messrs B. N. Peach, J. Horne, W. Gunn, C. T. Clough, L. W. Hinxman & H. M. Cadell: Quarterly Journal of the Geological Society, London, v. 44, p. 378–441.

Peach, B.N., Horne, J., Gunn, W., Clough, C.T., Hinxman, L.W., and Teall, J.J.H., 1907, The Geological Structure of the NW Highlands of Scotland. Memoirs of the Geological Survey of Great Britain. HMSO, Glasgow.

Sebring, L. Jr., 1958, Chief tool of the petroleum exploration geologist: The subsurface structural map: American Association of Petroleum Geologists Bulletin, v. 42, p. 561-587.

Soper, N.J., and Hutton, D.H.W., 1984, Late Caledonian sinistral displacements in Britain: implications for a three-plate collision model: Tectonics, v. 3, p. 781–794.

Soper, N.J., Strachan, R.A., Holdsworth, R.E., Gayer, R.A., and Greiling, R.O., 1992, Sinistral transpression and the Silurian closure of Iapetus: Journal of the Geological Society, London, v. 149, p. 871–880.

Strachan, R. A., Smith, M., Harris, A. L., and Fettes, D. J., 2002, The Northern Highland and Grampian terranes. In: Trewin, N.H., (Ed.), The geology of Scotland: Geological Society of London.

Thomas, W. A., 1977, Evolution of Appalachian-Ouachita salients and recesses from reentrants and promontories in the continental margin: American Journal of Science, v. 277, p. 1233-1278.

Thomas, W. A., 1983, Continental margins, orogenic belts, and intracratonic structures: Geology, v. 11, p. 270-272.